COVER PAGE

Preferred CPV Integration Assessment Report

REPORT DRAFT
DATE: March 2014

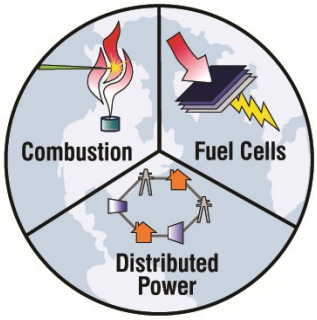

Submitted To:

Robert McConnell
Amonix Project Director
Office : 562-200-7741
Email: bob@amonix.com

Submitted By:

Professor Scott Samuelsen, Director
Professor Jack Brouwer, Associate Director
Advanced Power and Energy Program
University of California, Irvine
Tel: 949-824-7302 x11-221
Email: gss@uci.edu; jb@apep.uci.edu

March 2014

Executive Summary

Amonix, Inc., in partnership with the University of California, Irvine (UCI) and the National Renewable Energy Laboratory (NREL), is conducting a project to install two Amonix 7700 systems on the UCI campus for studies of grid integration and reliability. The project purpose is to provide technology and knowledge advancements that enable California to deploy a high percentage of ultra clean, secure and reliable solar electric generation at the lowest possible cost. The Amonix 7700 is a concentrating photovoltaic (CPV) system using inexpensive Fresnel lenses to focus the equivalent of 500 suns onto small 39% efficient solar cells. A 7700 has seven MegaModules that each produce approximately 10 kW (DC) and, with dimensions of 77' by 49', is the world's largest pedestal-mounted solar power generator. As part of this deployment the Advanced Power and Energy Program (APEP) at UCI is identifying and documenting the challenges and opportunities for installing large dual-axis CPV systems in UCI's distribution circuits. APEP is assessing the preferred dual-axis CPV integration by determining the value of peak solar generation and benefit of solar generation coordination with combined heat and power systems and demand management. In a set of additional tasks, Amonix and NREL are jointly conducting lifetime and reliability modelling by correlating failures observed in accelerated testing of dual-axis CPV components with measured weather data and with failures observed in the field deployment of the systems on the UCI campus and elsewhere.

The R&D tasks aim to address key integration barriers in installing and operating Amonix dual-axis CPV systems in a distributed grid. Additional R&D tasks address the lifetime and reliability validation of Amonix systems. The UCI tasks are as follows:

1. Subtask 2.3: Distributed dual-axis CPV electrical interconnection – to establish detailed monitoring of two Amonix 53 kW dual-axis CPV systems and the associated circuits.
2. Subtask 2.4: Preferred dual-axis CPV Integration Assessment – to assess and develop the preferred integration and operation strategies for dual-axis CPV systems integrated with complementary combined heat and power (CHP) and dispatchable air conditioning systems.
3. Subtask 2.5: Coordinate with RESCO and SCE – to coordinate with the RESCO project funded by the California Energy Commission and establish a partnership with Southern California Edison.

The integration of dual-axis CPV systems into the UCI Microgrid can impact both existing energy resources on the microgrid as well as microgrid circuit operation. The UCI subtasks evaluate both impacts. Subtask 2.3 focused on impacts associated with circuit operation. Subtask 2.4 evaluated the impacts on campus energy resources (e.g., gas turbine, thermal energy storage tank, etc.) in order to determine the preferred deployment and operation of dual-axis CPV technologies with CHP and dispatchable loads. This report focused on activities associated with Subtask 2.4.

This report summarizes (1) the dynamic modeling of UC Irvine's central plant, renewable, and future energy resources; (2) the integration of these models into a UCI community system model (Holistic Grid Resource Integration and Deployment tool); and (3) the use of this integrated campus energy system model to determine preferred deployment and operation of dual-axis CPV technologies with combined heat and power (CHP) and dispatchable loads (Subtask 2.4). Several analyses were performed using the Holistic Grid resource Integration and Deployment (HiGRID) tool to demonstrate how dual-axis CPV

systems could be integrated into the UCI Microgrid.

The first analysis investigated the effect of increasing the installed capacities of dual-axis CPV and fixed-tilt PV systems in the UCI Microgrid. Increasing the dual-axis CPV or fixed-tilt PV capacity always led to increased LCOE and reduced GT and ST capacity factors. However, there were interesting differences between the dual-axis CPV and fixed-tilt PV systems that can be leveraged by UCI as it continues to increase its on-site renewables. Fixed-tilt PV systems will not be able to deliver as much energy for a given installed capacity as dual-axis CPV systems can at lower energy penetrations, while at higher energy penetrations fixed-tilt PV systems will begin to have the ability to deliver more energy for a given installed capacity. This difference results from the more peaky nature of dual-axis CPV systems. From this comparison, if UCI were considering only solar resources, UCI should install dual-axis CPV systems on-site up to the limit dictated by space (22MW, (Samuelsen et al., 2013)) and then move to purchase dual-axis CPV from offsite locations until 27MW is reached at which point fixed-tilt PV should then be purchased.

The capability of smart cooling load dispatch to increase dual-axis CPV energy penetrations was demonstrated. The presence of the TES tank allows the campus cooling loads to be dispatched in order to increase dual-axis CPV energy penetrations significantly, which also leads to higher GT/ST capacity factors and lower levelized costs of electricity. However, at low dual-axis CPV fractions of annual energy met by renewables, the smart cooling load dispatch is not as effective as at higher fractions of annual energy met by renewables. The fraction of annual energy met by renewables at which the smart cooling dispatch became effective at increasing the renewable energy delivered to load per MW of dual-axis CPV installed was approximately 7%.

The analysis of electric energy storage using the case of a vanadium redox flow battery revealed that the implementation of energy storage achieves increased fractions of annual energy met by renewables over the case without energy storage. However, the energy storage system needs to be appropriately sized for a given fraction of annual energy met by renewables otherwise excessive curtailment could occur. At lower fractions of annual energy met by renewables, the capability of the energy storage system to reduce curtailment did not outweigh the high capital cost of this technology, but once higher fractions of annual energy met by renewables are achieved, the Vanadium-redox Flow Battery (VFB) storage system begins to be economical.

As the penetration of dual-axis CPV systems increase on the UCI Microgrid, the gas turbine and steam turbine must turn down in order to accommodate the renewable energy generated. As the penetration increases, the capacity factors decrease leaving these assets not fully utilized by the UCI Microgrid and providing an opportunity to use them in other ways to create revenue. This includes selling unused gas turbine and steam turbine capacity as spinning reserve or using the gas turbine to provide regulation. Using 4.5MW of the UCI gas turbine capacity and 5MW of the UCI steam turbine capacity for spinning reserve at CAISO market prices from 2010 and 2011 is not practical economically. Even in scenarios where the GT and/or ST bid into the market when prices were high, it was not practical economically, at least for the capacities selected for analysis. No further analysis optimizing the amount of capacity bid into the CAISO market was performed. Using the gas turbine to supply regulation to the California

Independent System Operator (CAISO) and the steam turbine to provide spinning reserves was economically beneficial to UCI at 2011 prices. Through simulation using an approximated automatic generation control signal and the dynamic gas turbine model, it was also determined that the gas turbine could physically provide reasonable regulation service.

1 Introduction

The goal of this project is to provide technology and knowledge advancements to enable California to deploy a large amount of ultra clean, regionally secure solar electric generation at the lowest possible cost. To meet this goal, four tasks were addressed. Each proposed task is complementary and specifically developed to address the most critical challenges and opportunities to increase solar deployment in California. In particular, UC Irvine was responsible for two tasks:

- Subtask 2.3 – Distributed dual-axis CPV Electrical Interconnection
- Subtask 2.4 – Preferred Integration Assessment

The objectives of UC Irvine's tasks are described below:

Subtask 2.3 – Distributed dual-axis CPV Electrical Interconnection:

The objective of this task is to establish detailed monitoring of two Amonix 53 kW dual-axis CPV systems and associated circuits at the University of California, Irvine. In the process of deploying the units, many of the challenges and opportunities to install large dual-axis CPV installations on distribution circuits will be identified and documented. Specifically, information regarding the impact of large dual-axis CPV installations on distribution electric infrastructure are to be identified. Lessons learned will provide valuable data and experience to rapidly evaluate future site deployments.

Subtask 2.4 – Preferred Integration Assessment:

The objective of this task is to evaluate the value of peak solar generation and benefit of solar generation coordination with combined heat and power systems and demand management. By coordinating with other gas turbine generators and dispatchable loads (e.g., air conditioning with thermal energy storage, and future electric vehicles), further reduction in the end users' utility bills per unit of solar installed capacity can be seen. In this way, the cost of solar energy is decreased not by reducing the direct cost of solar energy, but by the development of better grid integration and energy management strategies.

This report analyzes the integration of concentrated photovoltaic (dual-axis CPV) systems into the UCI Microgrid to determine the preferred integration of dual-axis CPV technologies (Subtask 2.4). These analyses are accomplished using models developed under this program in conjunction with the renewable-based energy secure communities (RESCO) program administered by the California Energy Commission. The various models used to study the integration of dual-axis CPV systems are:

- Gas Turbine (GT)
- Steam Turbine (ST)
- Heat Recovery Steam Generator(HRSG)
- Electric Chiller
- Thermal Energy Storage (TES) tank
- Solar Photovoltaic (fixed-tilt PV)
- Solar dual-axis CPV

- Vanadium Redox Flow Battery (VFB)

These models were integrated into a community system modeling tool. This community system modeling tool is called the "Holistic Grid Resource Integration and Deployment" (HiGRID) tool. This tool enables system analyses to be performed for communities such as university campuses, cities, neighborhoods, up to the level of the state of California. The resources listed above are specific to the UCI Microgrid with the exception of the Vanadium Flow Battery, which is a possible future resource. Many other resources needed development for the analysis of generic communities, but these will not be discussed in this report given the focus of this report is on the integration of dual-axis CPV systems into the UCI Microgrid. Each of these resource models will be discussed in detail while the integration of these models for use in the HiGRID tool (Section 5) will be discussed in a separate section once each component model is described.

The HiGRID tool will be used to investigate the effects of varying dual-axis CPV penetration levels on the UCI Microgrid and in particular how the cooling loads can be dispatched using the TES tank to enable higher fraction of annual energy met by renewabless. In addition to this analysis, the effects of installing dual-axis CPV and fixed-tilt PV systems will be studied. The addition of electric energy storage as a future resource on the UCI Microgrid will also be evaluated. It is noted that increasing fraction of annual energy met by renewables on the UCI Microgrid will require the GT and ST to turn down reducing their annual capacity factors. Given this, the use of the GT and ST for providing regulation and spinning reserve to the CAISO is also investigated. The following subsection summarizes the current resources of the UCI Microgrid.

1.1 UCI Microgrid

The UCI campus infrastructure was methodically and systematically designed from scratch with a large, circular central park encircled by a one-mile underground utility tunnel loop connected to central energy and information infrastructure. Today, the UCI campus infrastructure serves a community of more than 30,000 people and encompasses a wide array of building types (residential, office, research, classroom), transportation options (automobiles, buses, shared-cars, bicycles), and a wide array of distributed energy resources. The UCI campus infrastructure constitutes a microgrid and will be referred to as such throughout this report. A major aspect of this infrastructure is the UCI Central Plant, which will be modeled and discussed in this section.

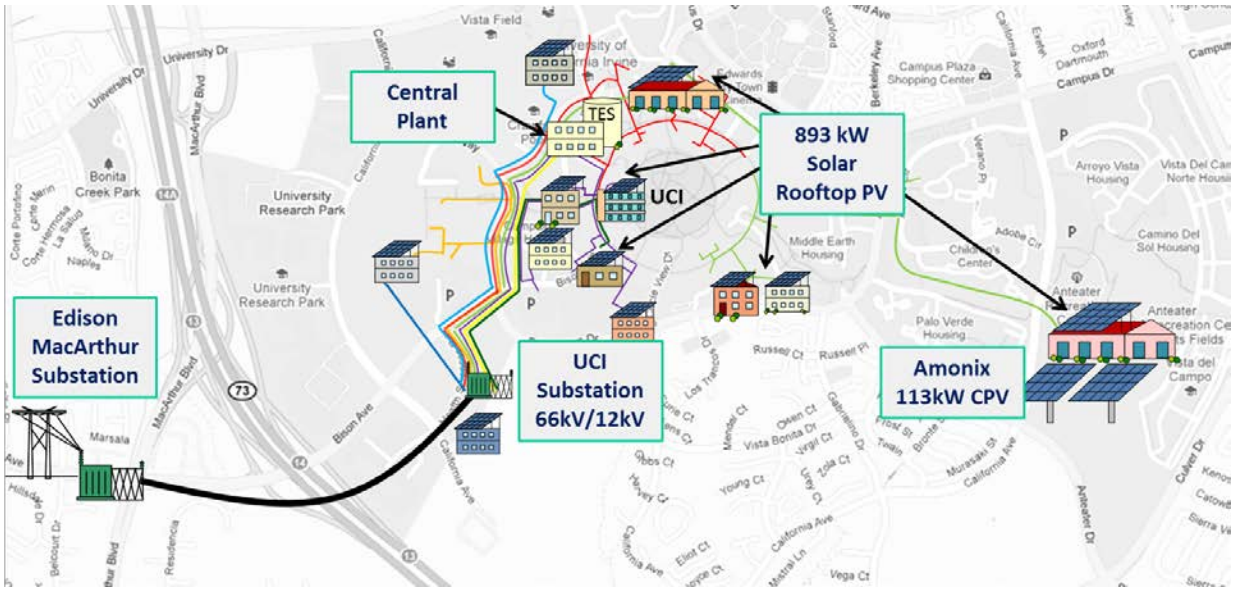

Figure 1: University of California, Irvine Microgrid

As shown in Figure 1, the UCI Microgrid is a test bed that (1) is served by Southern California Edison (SCE) through the UCI Substation which steps down voltage from 66kV to 12kV using two 15 MVA transformers, (2) encompasses ten 12kV circuits, (3) includes more than 1 MW of solar power, (4) is served by a 19MW natural gas fired combined cycle plant, (5) incorporates centralized chilling including one of the largest thermal energy storage tanks in the country (4.5 million gallons/60,000 ton-hours), and (6) serves all major buildings with district heating and cooling. The UCI Microgrid also contains a unique set of distributed energy resources that is unparalleled in the world including: (1) electric vehicle charging at multiple parking locations, (2) integrated fuel cell absorption chilling, (3) hydrogen fueling for fuel cell vehicles, (4) two-axis tracking concentrated solar photovoltaic systems, (5) advanced building energy efficiency measures, (6) advanced building monitoring and control, and (7) advanced power, power quality, and thermal metering.

2 UCI Central Plant Model

The various models discussed in this section will comprise the UCI Central Plant model that will be used in the HiGRID tool framework (Section 5) to simulate the UCI Microgrid operation under different dual-axis CPV deployment scenarios as well as different complementary technology scenarios. Specifically, the UCI Central Plant model will be utilized in the HiGRID Dispatchable Load and Balance Generation modules as described in (Section 5) and (Eichman, Mueller, Tarroja, Schell, & Samuelsen, 2013; Samuelsen, Mueller, & Eichman, 2013).

2.1 Central Plant Description and Energy Trends

The UC Irvine Central Plant consists of 8 electric chillers, a steam turbine chiller, a thermal energy storage tank, boilers (used only for backup), a 13.5 MW gas turbine, a heat recovery steam generator (HRSG), a duct burner, and a 5.5 MW steam turbine (Figure 2). The central plant serves all the campus heating and cooling loads as well as the majority of the campus electric loads. The 8 electric chillers are

capable of supplying 14,500 tons, and the steam driven chiller is capable of an additional 2,000 tons. The campus cooling load averages 3,100 tons (74,400 ton-hours per day) with a peak annual demand of 13,900 tons. The thermal energy storage tank uses a thermocline to minimize mixing. The chillers operate to facilitate this thermocline while also increasing efficiency by recirculating water exiting the chiller back to the chiller inlet until 39 °F is maintained at the chilled water exit. The thermal energy storage tank is able to shift, on average, 65% of the chilling load during the day to the night when electricity prices are lower and temperatures are cooler, which results in more efficient chiller operation via better heat rejection through the cooling towers. The campus heating load averages 44 MMBtu/hr with a peak annual demand of 100 MMBtu/hr. The heating load is served entirely through recovered heat from the gas turbine and use of the duct burner. The HRSG can supply 52,000 lbs/hr steam without duct fire and 120,000 lb/hr with duct fire. The campus electric load averages 13.4 MW with a peak annual demand of 18.6 MW (note: this is the electric load separated from the electricity used to serve the campus cooling loads). The gas turbine and steam turbine supply about 85% of the electrical energy needs on the campus with the balance being served by solar resources (1%) and utility import (14%).

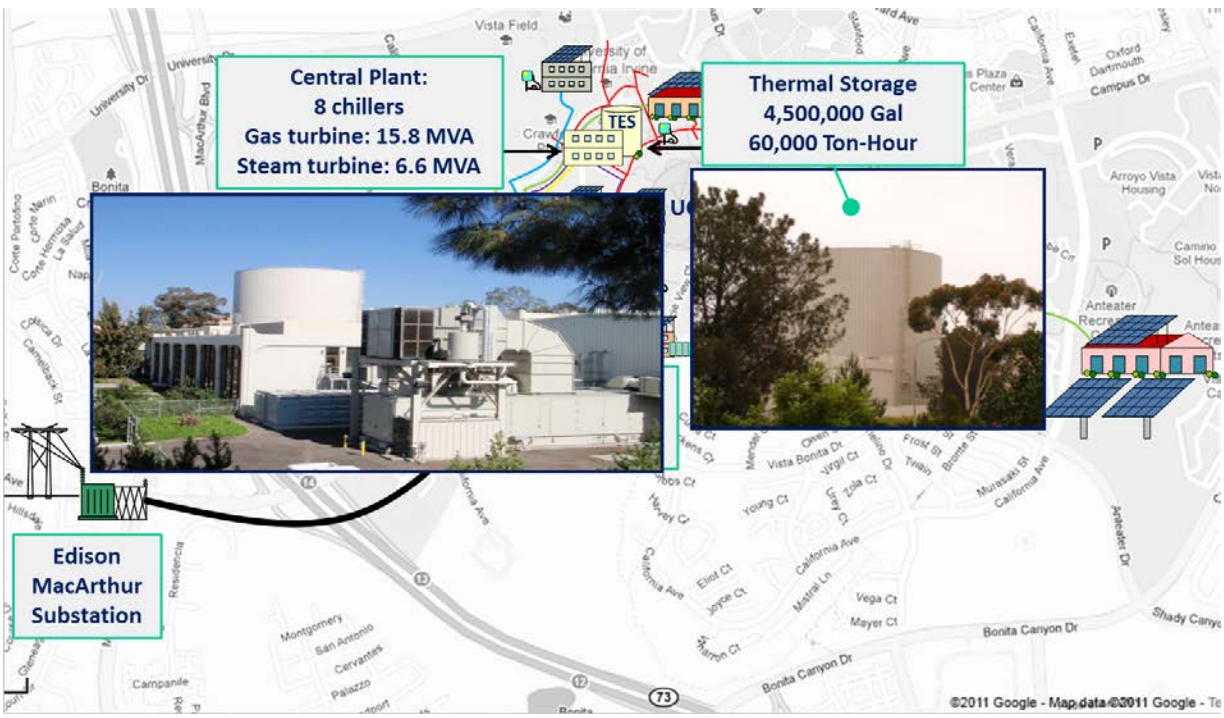

Figure 2: UC Irvine Central Plant

2.2 Gas Turbine Model

The gas turbine is used to meet a portion of the electric demand of the campus, while providing exhaust heat to be used to meet the campus heating demand. The model is based on rigorous first principles quasi-steady state dynamics, contains thermodynamics equations that describe the simplified physics for each of the major components of the gas turbine. These component parts consist of a compressor, combustor chamber, turbine, power shaft, air handling system, and enclosure housing. A schematic of the single-shaft natural-gas fired gas turbine in component modules is shown in Figure 3. Synchronous operation is preferred for single-shaft configurations because the generator needs to reliably produce

electricity at constant frequency (60 Hz). Under any operating condition other than start-up and shut-down, power produced by the turbine drives both compressor and the generator load.

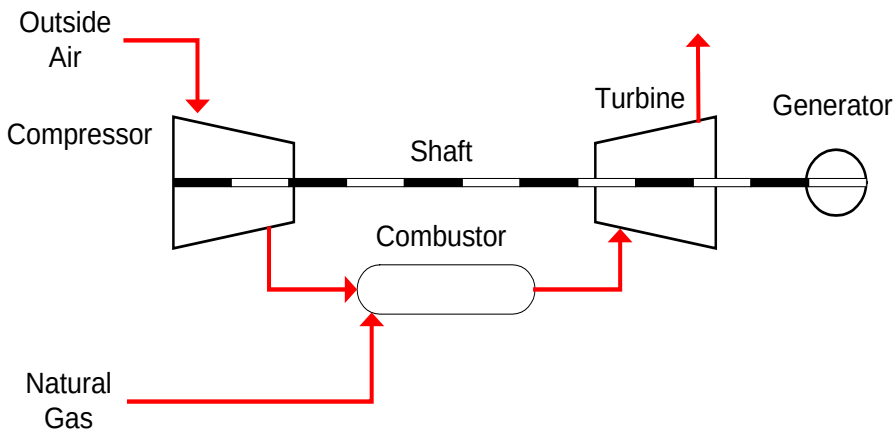

Figure 3: Block diagram of gas turbine engine components

Assumptions:

1. All gases are ideal gases
2. Heat transfer to the environment is assumed to occur primarily at the engine section
3. The generator is assumed to be well insulated.

2.2.1 Compressor and Turbine

The compressor and turbine work can be expressed as a function of their respective isentropic efficiency, rotor inlet temperature, compression ratio, and specific heat ratio, with the following expressions

$$\dot{W}_{\text{comp}} = \eta_{\text{comp}} \frac{kRT_{01}}{k-1}\left[\left(\frac{P_{02}}{P_{01}}\right)^{k-1/k} - 1\right] \tag{1}$$

$$\dot{W}_{\text{turb}} = \eta_{\text{turb}} \frac{kRT_{03}}{k-1}\left[\left(\frac{P_{04}}{P_{03}}\right)^{k-1/k} - 1\right] \tag{2}$$

where isentropic efficiency of the compressor and turbine can be determined, respectively, as

$$\eta_{\text{comp}} = \frac{T'_{02} - T_{01}}{T_{02} - T_{01}} \tag{3}$$

$$\eta_{\text{turb}} = \frac{T_{03} - T_{04}}{T_{03} - T'_{04}} \tag{4}$$

The energy balances for the compressor and turbine are given as,

$$\rho C_{mass} V_{cv} \frac{dT_{02}}{dt} = \dot{E}_{in} - \dot{E}_{out} + \dot{W}_{comp} \tag{5}$$

$$\rho C_{mass} V_{cv} \frac{dT_{04}}{dt} = \dot{E}_{in} - \dot{E}_{out} + \dot{W}_{turb} \tag{6}$$

where $\dot{E}_{in}$ and $\dot{E}_{out}$ are enthalpy terms representing the internal energy of flow at the inlet and outlet of the compressor and turbine. The flow enthalpy can be captured based on the sensible enthalpy of the fluid species and their respective heat of formation as follows:

$$\dot{E}_i = \sum^{i} m_i \left[\overline{h}^{o}_{f,i} + \left(\int_{T_{ref}}^{T} \overline{c}_p dT \right) \right] \tag{7}$$

2.2.2 Combustor

Most state-of-the-art combustors utilize dry lean-premixed combustion technology to achieve low levels of both nitrous oxides (NOx) and carbon monoxide (CO) emissions. The combustion chamber is characterized as a constant volume and perfectly mixed reactor where complete and instantaneous combustion reaction occurs. The key assumption here is chemical kinetic rates are 2 to 6 orders of magnitude greater than transport phenomena in a gas turbine engine (Gou, 2010). On the other hand, complete reaction is a reasonable assumption due to the inherent characteristics of dry lean-premixed technology to combust fuel with a large excess of air above the required stoichiometric level. In the model, the combustion is simulated as a complete combustion reaction of methane with the overall reaction,

$$CH_4 + 2O_2 \rightarrow CO_2 + 2H_2O \tag{8}$$

The conservation of mass in the combustion chamber is described by

$$\frac{dP}{dt} = \frac{RT}{V}\left(\dot{N}_{in} - \dot{N}_{out} + \sum R_i \right) \tag{9}$$

The energy conservation is

$$\rho C_p V_{cv} \frac{dT_3}{dt} = \dot{E}_2 - \dot{E}_3 - \dot{Q}_L \tag{10}$$

The pressure losses in the combustor is expressed as

$$P_2 = P_3 \left(1 - \frac{\Delta p}{100} \right) \tag{11}$$

2.2.3 Power Shaft

The coupling of the shaft speed and torque of the compressor, turbine, and generator can be described by a torque balance performed on the rotating shaft. As shown in Figure 4, the torque produced by the turbine on the shaft is opposed by the torque of the compressor and the generator. The torque by the compressor and turbine, respectively τ_{comp} and τ_{turb}, are sometimes referred to as "developed torques." The opposing torque produced by the steady operation of the generator generally referred to as load torque, τ_{load}, is a resistive torque caused by the rotating motion of reduction-drive gearbox, generator shaft, and synchronous generator with permanent magnet exciter. The aggregated inefficiencies of these components inside the generator compartment amount to minimal efficiency loss.

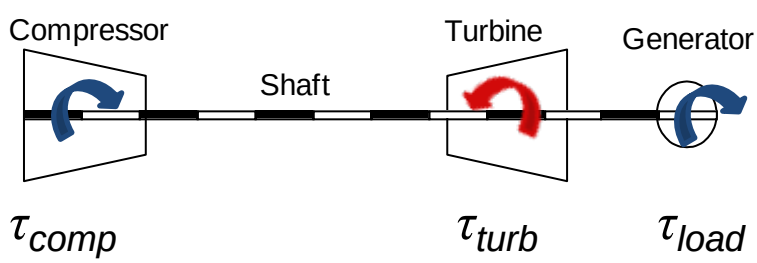

Figure 4: Schematic of the torque diagram around the rotating shaft of single-spool

The torque analysis based on the rotating shaft relates the change in shaft speed, ω, and the rotating inertia to the torque balance

$$\tau_{turb} - \tau_{comp} - \tau_{load} = J \frac{d\omega}{dt} \tag{12}$$

Since the work being done, P, on a rotating body is a product of the exerting torque and the angular velocity,

$$P = \tau\omega \tag{13}$$

Power balance on the rotating shaft then becomes

$$P_{turb} - P_{comp} - P_{load} = J\omega \frac{d\omega}{dt} \tag{14}$$

where the power of the generator, P_{load}, is a controlled variable for the feedback control of the fuel inlet. The power of the compressor, P_{comp}, and turbine, P_{turb}, are output variables determined from thermodynamic relationships and part-load characteristic maps. Figure 5 shows the model representation of Equation (14) in Simulink.

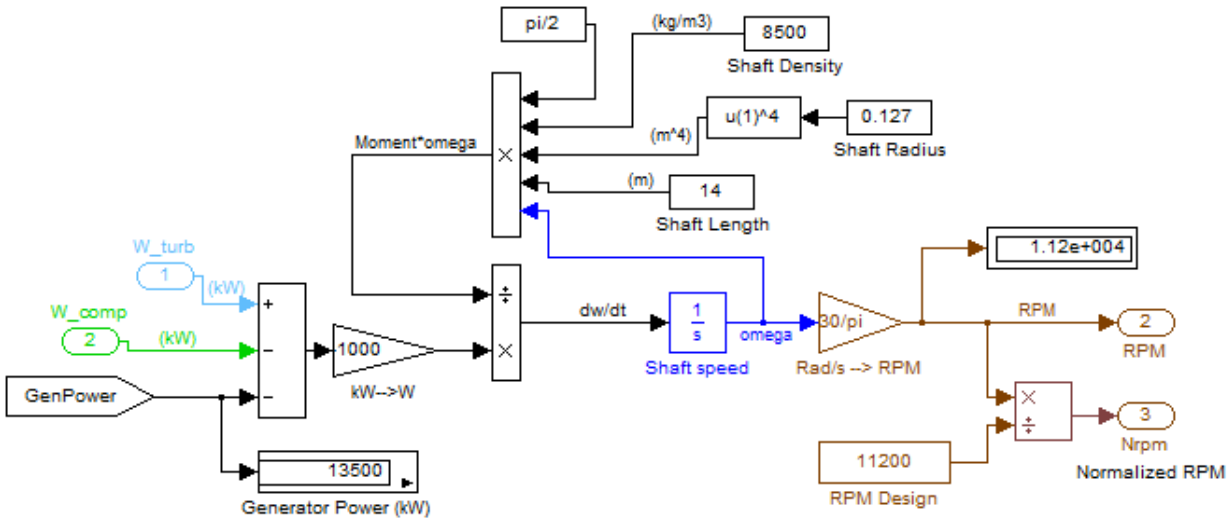

Figure 5: Simulink representation of the shaft dynamics

2.2.4 Air Handling Unit

As ambient temperatures rise, gas turbine efficiency and power output decrease due to a lower density of air. In conventional combined cycle plants, this effect is alleviated by installing air cooling systems to lower the compressor inlet temperature and effectively increase gas turbine performance. Standard air cooling systems can be quite complex but for simplicity, the model assumes a pressure loss across an air filter and cooling coil. The cooling coil module is simulated as a discretized counter-flow shell-and-tube configuration as shown schematically in Figure 6. Quasi-two-dimensional conductive and convective heat transfer using Fourier's law and Newton's law of cooling are considered and resolved at each node with control volumes for the shell side, tube side, and the heat exchanging wall.

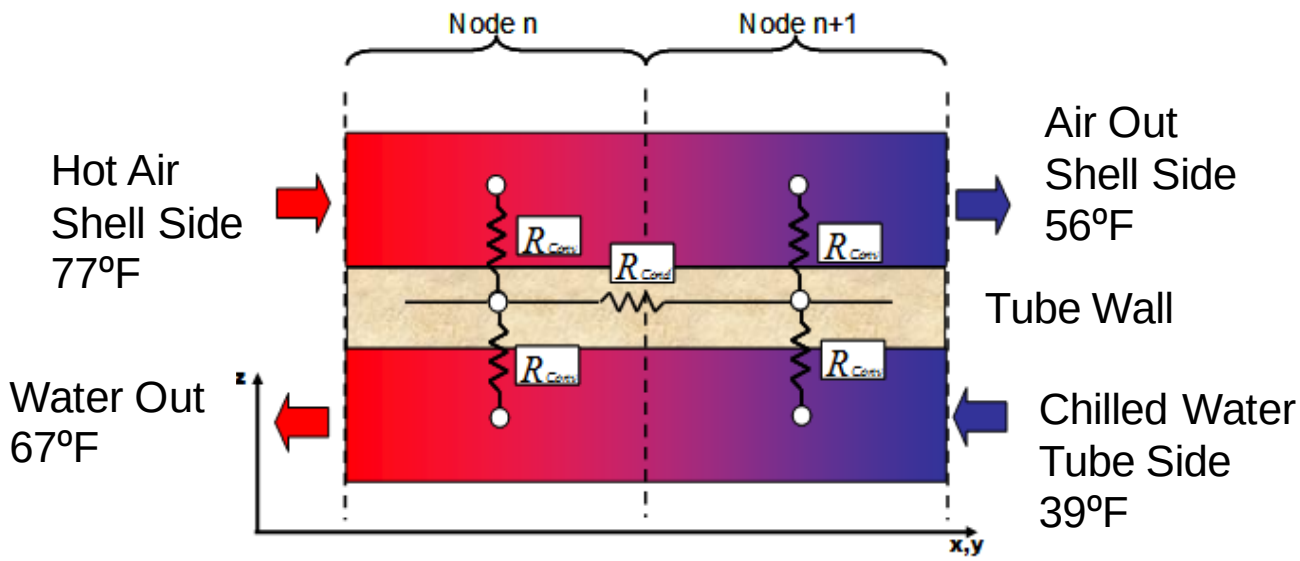

Figure 6: Discretized counter-flow shell-and-tube cooling coil

2.2.5 Control logic

The control strategy of the gas turbine is modeled as having two active principal controllers: temperature control by variable inlet guide vane (VIGV) manipulation and power control by fuel flow manipulation. The temperature controller of gas turbine model has been tailored after recorded field data of a Solar Titan 130 at various part loads under steady state operation. As shown in Figure 7, the turbine exhaust temperature is controlled by manipulating the air flow rate with a proportional and integral action with a feed forward. The feed forward block contains recorded field data of the Titan 130 engine relating the turbine exhaust temperature to various part loads. In synchronous engines typically used in CCHP systems, the air flow rate is physically controlled by the closing action of the variable inlet guide vanes (VIGV). The VIGVs are connected together by a rod to an actuator. Thus, the closing action of the VIGVs can be simulated as a transfer function with a time delay constant. In the physical system, the closing of the VIGVs not only reduces the air flow but also changes the angle of incidence of the air flow into the compressor rotor blades. Since the compressor module contains a VIGV performance map, the deviation of the angle of incidence or VIGV angle (from off-design position) corresponds to a specific compressor air flow and pressure ratio.

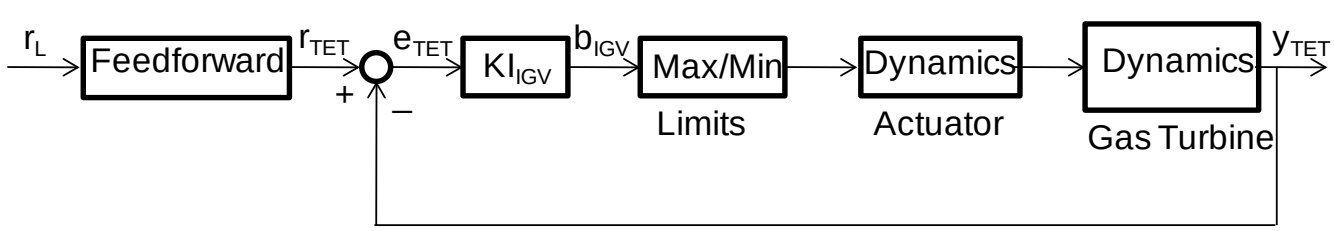

Figure 7: Modeled Solar Titan 130 temperature controller

The gas turbine power is controlled by manipulating the fuel flow into the combustor with a proportional and integral action without a feed forward. This power controller is displayed in the block diagram in Figure 8. The dynamics of the fuel delivery system is represented by a first order transfer function with time delay constant. For synchronous gas turbines, while the load control is active during all operating conditions, speed control is only active during transient operation. The proportional and integral speed control loop serves as a curtailment or increase of fuel delivered to ensure constant shaft speed. This is especially important for the generator to maintain its frequency to that of the 60 Hz regulation. Also during transient operation, acceleration control by fuel manipulation becomes active when the acceleration of the generator exceeds the acceleration limit. This is an integral control feedback loop without feed forward. The output of the three control loops for the fuel delivery system are fed into a minimum value select gate where the loop with the lowest output will be the active controller of the fuel flow.

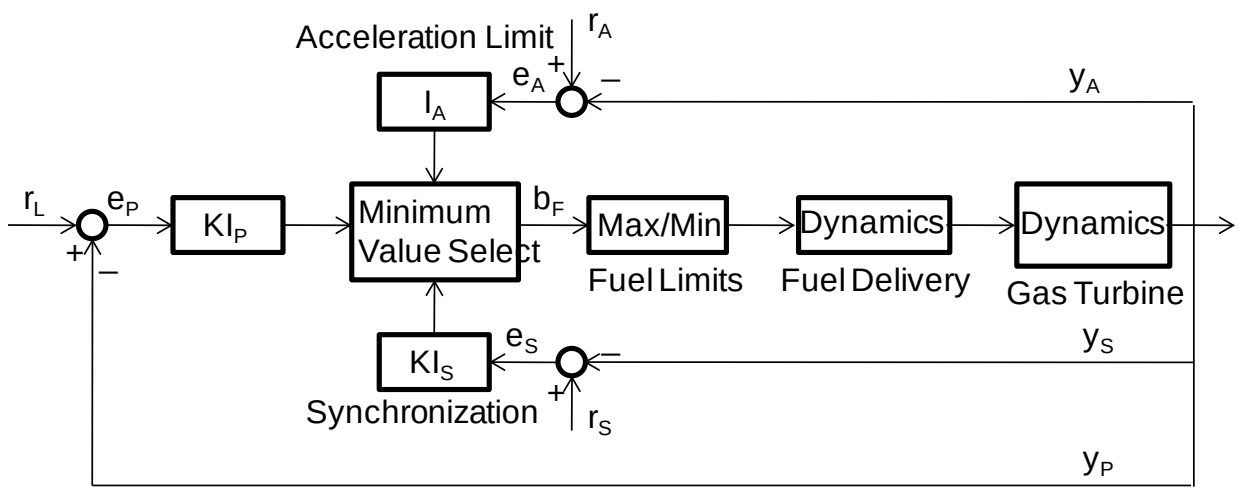

Figure 8: Modeled Solar Titan 130 power controller

2.2.6 Model Validation: Design and Off-Design Characteristics

The off-design simulation of the engine performance requires the performance maps of the compressor and turbine for part-load characteristics. These performance maps of the compressor and turbine are generally not available for proprietary reasons. Performance maps of representative gas turbines are used in their places. The maps are then tailored to match the design-point performance specifications (Table 1) of the Titan 130. Part-load performance is simulated by employing a controlling scheme to manipulate the fuel flow and the air flow according to observed field data and suggested turbine exit temperature (TET) control from the literature.

In part-load operation of the Titan 130, the inlet airflow is controlled by modulating the variable inlet guide vanes (VIGV). This is to ensure that the turbine exit temperature (TET) is at the highest level as possible. Maintaining the highest possible TET is critical for the efficiency of the heat recovery steam

generation system in cogeneration plants. The first six compressor stages are equipped with VIGVs for the Titan 130. The setting angles of the variable vanes are actively controlled during part-load operation to change the airflow characteristics. Changing the angle of these vanes or VIGV modulation provides the closing effect on the air flow and changes the direction of the air flow being introduced into the rotor inlet. Both of these physical effects provide surge protection for the compressor by lowering pressure ratio and moving the operating point away from the surge line in part-load operation. In the model, the operating characteristics of the compressor are derived from empirical performance of a representative compressor at different IGV angles. The minimum operating power of the gas turbine is about 8 MW. If the gas turbine power is required to drop below 8 MW for any reason, the entire system must shut down or 'trip' offline.

Table 1: System parameters of Solar Titan 130 engine for design performance

Parameters	Design Specs	Field Data	Simulation
Electrical Power [MW]	13.5	13.5	13.5
Shaft speed [rpm]	11,200	--	11,200
Pressure Ratio	16	16	16
Fuel Flow (Natural Gas) [pph]	--	6600	6600
Air Flow Rate [pph]	396,390	--	418,260
Engine Efficiency [%]	33.3	32.6	32.6
Compressor Efficiency [%]	83	--	83
Turbine Efficiency [%]	--	--	85.6
Compressor Inlet Temperature [^{o}F]	59	55	55
Firing Temperature [^{o}F]	2050	--	1903.7
T5 Temperature [^{o}F]	--	1400	1400
Exhaust Temp [^{o}F]	913	926	926

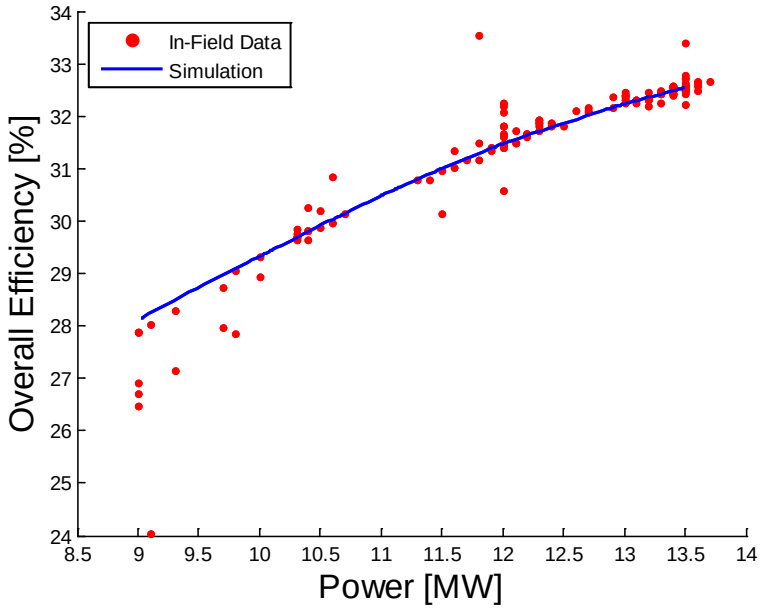

Figure 9: Simulated results of the overall efficiency of the gas turbine model as compared to in-field operation (Jan 17-23, 2010) of the Titan 130

Steady-state performance of the gas turbine is first verified by comparing simulated results against two full weeks of field operation data. Field operation data have been obtained for one full week in January 2010 and another week in August 2010.

The overall efficiency of the gas turbine, displayed in Figure 9, shows the model capability in capturing the part load performance of the engine. The maximum efficiency attainable for this engine reaches 32% at peak load. According to the data, the engine can attain higher power than the design value at some points during the operational time frame. This suggests that under some favorable inlet conditions, the airflow intake could exceed the design value by the opening of the VIGV (negative value).

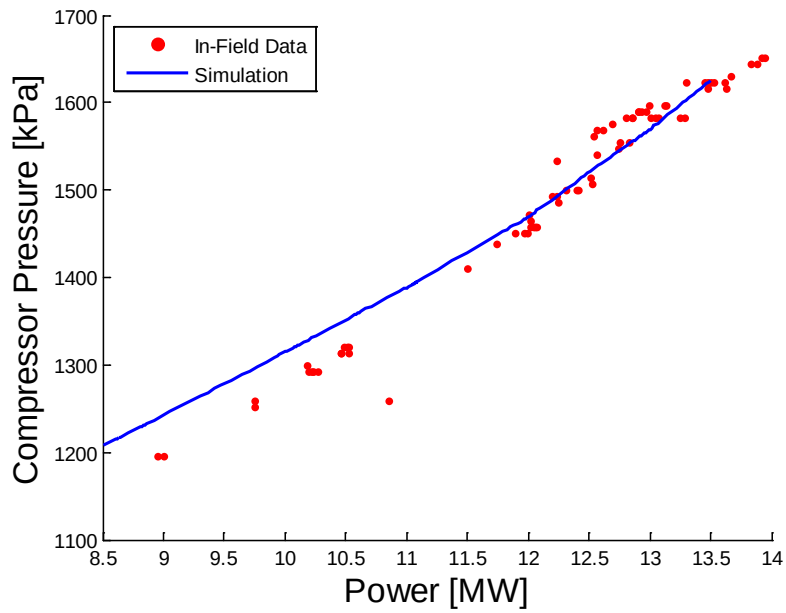

Figure 10: Compressor discharge pressure versus engine load

Figure 10 shows the compressor exit or discharged pressure variation with part-load. The compressor discharged pressure increases as part load increases. Very small discrepancies between simulated results and the actual data occurred at low part load of 9 MW. Dynamic verification against operational data was also performed as shown in Figure 11. The model well predicts the dynamic performance of the system. For more verification of the gas turbine model see (Do, 2013).

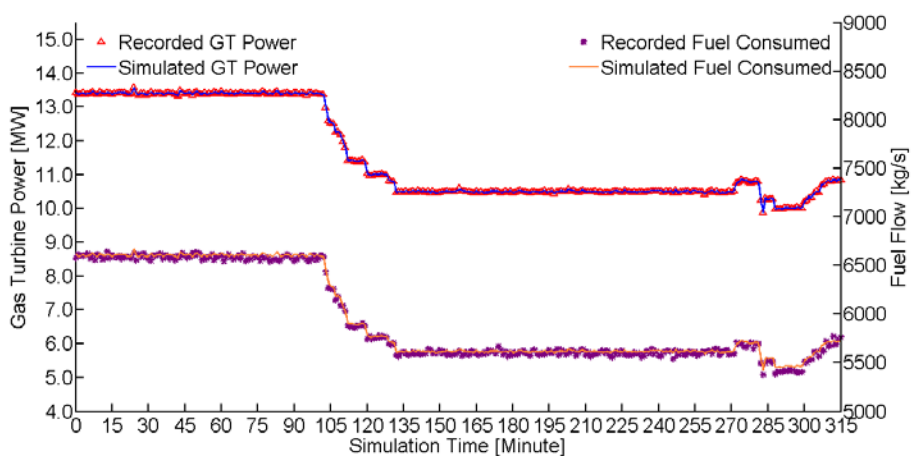

Figure 11: Simulated fuel consumption transient during the unscheduled power ramp-down event on March 5, 2011. Top curve features simulated gas turbine power versus experimental data. Bottom curve features simulated fuel consumption versus experimental data

2.3 Heat Recovery Steam Generator Model

The heat recovery steam generator (HRSG), which uses exhaust from the gas turbine to produce steam that is used to meet the heating demand of the campus and potentially produce additional electricity through the use of the steam turbine, is modeled using the Number of Transfer Units (NTU) method. The expressions for the heat exchanger effectiveness are presented as follows:

$$\varepsilon = \frac{1}{C_r}\left[1-\exp\left\{-C_r\left[1-\exp(-NTU)\right]\right\}\right] \qquad C_{\min} \text{ unmixed } C_{\max} \text{ mixed} \tag{15}$$

$$\varepsilon = 1-\exp\left\{-\frac{1}{C_r}\left[1-\exp(-C_r\cdot NTU)\right]\right\} \qquad C_{\min} \text{ mixed } C_{\max} \text{ unmixed} \tag{16}$$

Where

$$NTU = \frac{UA}{C_{\min}} \tag{17}$$

C_r refers to the ratio of the heat capacity coefficients of the two fluids (C_{min}/C_{max}), U is the overall heat transfer coefficient, and A is the area of heat transfer.

The heat recovery steam generator (HRSG) model is an integrated dynamic model consisting of individual cross-flow dynamic models simulating the physical and transient performance of the major HRSG components. The simulated components are the economizer, two subsequent boilers, and the superheater. Under all operating cases, cross-flow configuration using the effectiveness-NTU method is modeled with the assumption that the air side is the mixed fluid and the water or steam side is the unmixed fluid. Thus, equations (15) and (16) are used to determine the effectiveness factor of each heat transfer component. Boiler #1 is simulated as a single-phase cross-flow heat exchanger with the key assumption that the colder fluid, in this case water, is heated up to the onset of evaporation. This is reasonable based on the observation that water still retains its liquid phase while moving through this section of the HRSG. Boiler #2 is simulated as a cross-flow heat exchanger with a phase change occurring on the colder and unmixed fluid side. Preliminary analysis indicated that the air side is generally the limiting factor in the heat transfer but the model has the intelligence to switch between equations (15) and (16).

2.4 Steam Turbine Model

If steam in excess of the amount required to meet the campus heating demand is present, this additional steam is routed through the steam turbine to produce additional electricity to meet the campus electric load. The on-campus steam turbine is a 5.5 MW unit that does not include any steam extraction, and is oversized for this application in anticipation of an expansion of the gas turbine capacity.

The steam turbine is modeled with a physical dynamic model of the steam turbine based on first-principle thermodynamics is developed and validated against in-field operation data. The mass balance for the steam turbine is given as,

$$V_{cv}\frac{d\rho}{dt} = \dot{m}_{in} - \dot{m}_{out} \tag{18}$$

The transient energy balance takes into account the enthalpy difference between the inlet and outlet steams, the work done on the turbine blades by the steam, and a constant heat loss to the surrounding. The governing equation for the energy balance is thus,

$$\rho C_p V_{cv}\frac{dT}{dt} = \dot{m}h\big|_{in} - \dot{m}h\big|_{out} - \dot{W}_{st} - \dot{Q}_L \tag{19}$$

where $\dot{W}_{st}$, the actual mechanic work, deviates from the ideal mechanic work according to its isentropic efficiency and is given by the expression,

$$\dot{W}_{st} = \eta_{isen}\left(\dot{m}h\big|_{in} - \dot{m}h\big|_{out}\right) \tag{20}$$

During the expansion stages, the steam loses some of its quality. The outlet enthalpy therefore is a function of quality and is expressed as

$$h_{out} = h_f + xh_{fg} \tag{21}$$

All thermodynamic properties for steam are obtained from steam tables derived from the International Association for the Properties of Water and Steam (IAPWS IF-97). Peak isentropic efficiency of 0.9 was used for the model, representing the typical value for steam turbines. Important design characteristics for the central plant turbine are synchronous generator, inlet-pressure valve control, and operating pressure range of 230 psig inlet and 15 psig outlet.

The off-design performance of the steam turbine was simulated using a steam turbine performance curve derived from part-load study as reported by Fallah (Fallah, 1978) . The resulting performance curve relates the isentropic efficiency to the steam flow.

2.5 Electric Chiller Models

The campus cooling system consists of eight centrifugal chillers in parallel, a multiple-cell cooling tower with a common pump, and a stratified water thermal energy storage (TES) tank (4.5 million gallon; 60,000 ton-hour). Figure 12 shows the cooling system's primary-secondary loop schematic.

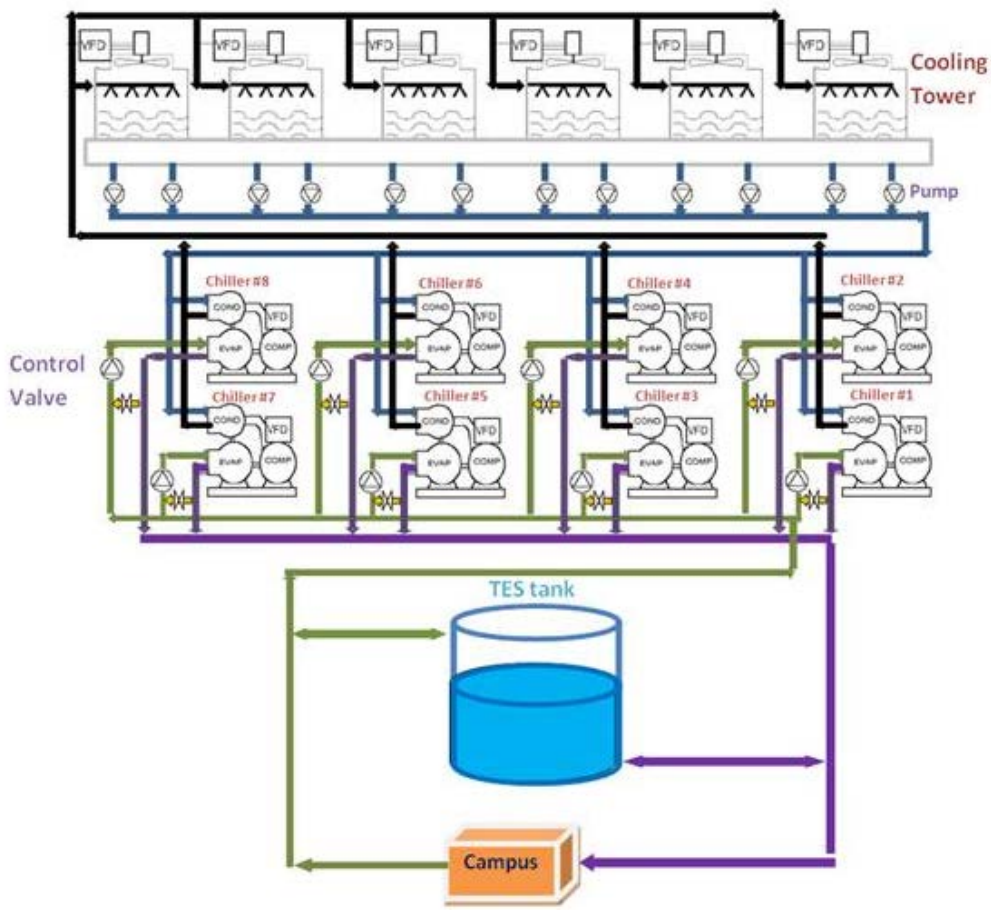

Figure 12: University of California at Irvine's central plant primary-secondary loop schematic

A quasi-steady thermodynamic model of the campus cooling system has been developed by modeling each of the plant components based on models in the literature. Each of the component models are developed based on conservation of mass, momentum and energy and resolving the key transport phenomena (e.g., heat transfer).

2.5.1 Compressor

Figure 13 gives the vapor compression cycle of the centrifugal chillers studied.

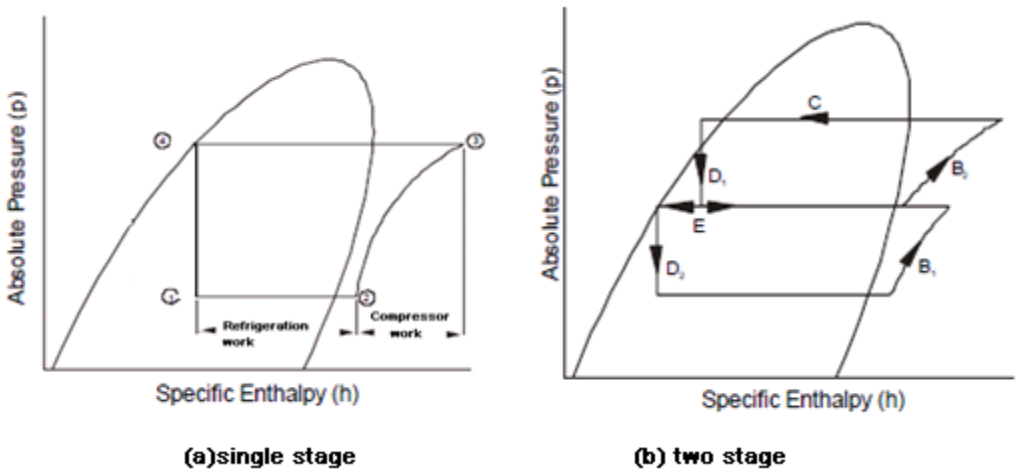

Figure 13: Vapor compression cycle pressure-enthalpy diagram

The isentropic approach is used for compressor analysis. The isentropic work for the single stage compressor is given as:

$$w = c_1 m_r (h_3 - h_2) + c_2 \tag{22}$$

The two-stage compressor uses an economizer which flashes a portion of the refrigerant. It is assumed that the inter-stage saturated temperature in the economizer T_{int} is:

$$T_{\text{int}} = \frac{T_{ev} + T_{cd}}{2} \tag{23}$$

And the isentropic work is given by:

$$W = c_1 m_r [(1-x)\Delta h_{B1} + \Delta h_{B2}] + c_2 \tag{24}$$

2.5.2 Evaporator and Condenser

The chilled water flows through the evaporator and condenser of the chiller. The evaporator is a heat exchanger where the chilled water gives up its sensible heat (the water temperature drops) and transfers the heat to the refrigerant as latent energy (the refrigerant evaporates or boils). The condenser is also a heat exchanger, where the heat leaves the refrigerant (condensing the refrigerant) and enters the condenser water (raising its temperature).

As in the previous study (Liu, 1997), the method of log mean temperature difference (LMTD) is adopted to model the heat transfer performance of the shell-and-tube flooded type evaporator and condenser. The mathematical expressions to determine the cooling load, heat exchanger conductance (AU), and LMTD are summarized in following equations:

$$\dot{Q}_{evap} = \dot{m}_{chw} C_w (T_{chwr} - T_{chws}) \tag{25}$$

$$\dot{Q}_{evap} = UA_{evap} LMTD_{evap} \tag{26}$$

$$LMTD_{evap} = \frac{T_{chwr} - T_{chws}}{\ln(\frac{T_{chwr} - T_{evap}}{T_{chws} - T_{evap}})} \tag{27}$$

It is assumed that the overall UA is a function of chilled water flow rate and cooling load. And the following equation is used to determine the overall AU.

$$AU_{evap} = \frac{1}{c_1 m_w^{-0.8} + c_2 Q_{cl}^{-0.745} + c_3} \tag{28}$$

2.5.3 Cooling Tower

The NTU-effectiveness analysis is engaged to model the cooling tower. The number of transfer units (NTU) can reflect the cooling tower performance, which is given by the equation developed by Lowe and Christie (Lowe & Christie, 1961):

$$Ntu = c(\frac{m_{cdw}}{m_a})^{1+n} \tag{29}$$

The fictitious specific heat C_{paf} is defined as the enthalpy difference over the temperature difference of the leaving and entering condition of the saturation air as:

$$C_{paf} = \frac{h_{awbe} - h_{awbl}}{T_{awbe} - T_{awbl}} \tag{30}$$

The LMTD method is adopted to describe the effective heat transfer coefficient (AU_{ct}) of the cooling tower:

$$AU_{ct} = \frac{Q_{cd} C_{pa}}{C_{paf} LMTD_{ct}} \tag{31}$$

$$LMTD_{ct} = \frac{(T_{ctwe} - T_{ctwl}) - Approach}{\ln((T_{ctwe} - T_{ctwl}) / Approach)} \tag{32}$$

The mass flow rate of air m_a is computed by the given relationship between Ntu and AU_{ct}:

$$Ntu = \frac{AU_{ct}}{m_a C_{pa}} \tag{33}$$

The cooling fan power is determined by mass flow rate of air:

$$w_{fan} = \exp(A + B \cdot \ln(m_{air})) \tag{34}$$

2.5.4 Water Pump

The following equations are used to model constant speed pumps. The efficiency and shaft power are a function of flow rate.

$$W_{shaft} = A_1 + B_1 \cdot GPM \tag{35}$$

$$\eta_{pump} = A_2 + B_2 \cdot GPM + C_2 \cdot GPM^2 \tag{36}$$

$$W_{pump} = \frac{W_{shaft}}{\eta_{pump}} \tag{37}$$

When variable speed pumps are used, the pump power is computed by use of the 'affinity laws'.

2.6 Thermal Energy Storage Tank Model

The TES is modeled as presented in (Hermanns, 2003). Several assumptions are made in the development of the equations solved in each of the TES control volumes:

1. Mass flow occurs only in one direction either from top to bottom or bottom to top.
2. Working fluid: liquid water.
3. No heat transfer to the environment is allowed. The tank is assumed to be well insulated from the environment.
4. Between control volumes, only mass transport and conductive heat transfer is considered.

Based on these assumptions, the molar flow rate and temperature of each control volume of the TES are determined from the appropriate transient energy and mass conservation equations of the same general form. Figure 14 shows the schematic of the modeled stratified thermal energy storage tank. The flow rates throughout the tank are calculated by the mass conservation equation in each control volume as follows.

$$\dot{N}_{\mathrm{HX}} = \dot{N}_{\mathrm{TES}} + \dot{N}_{\mathrm{Load}} \tag{38}$$

where $\dot{N}_{\mathrm{HX}}$, $\dot{N}_{\mathrm{TES}}$, and $\dot{N}_{\mathrm{Load}}$ show flow rate of the heat exchanger, internal flow rate of the TES tank, and flow rate of the hot water-exhaust gas recuperator respectively.

Temperature at each control volume is evaluated from transient energy conservation equation. Flow direction from top to bottom is assumed to be positive.

$$\dot{N}C_V \frac{dT}{dt} = \dot{N}_{\text{in}} h_{\text{in}} - \dot{N}_{\text{out}} h_{\text{out}} + \sum \dot{Q}_{\text{in}} - \sum \dot{W}_{\text{out}} \tag{39}$$

i = 1

$$\dot{N}_1 C_V \frac{dT}{dt} = \dot{N}_{\text{HX}} h(T_{\text{HX}}) - \dot{N}_{\text{Load}} h(T_1) - \dot{N}_{\text{TES}} h(T_1) + Q_{\text{in}} \tag{40}$$

1< i < n

$$\dot{N}_i C_V \frac{dT}{dt} = \dot{N}_{\text{TES}} h(T_{i-1}) - \dot{N}_{\text{TES}} h(T_i) + Q_{\text{in}} \tag{41}$$

i = n

$$\dot{N}_n C_V \frac{dT}{dt} = \dot{N}_{\text{TES}} h(T_{n-1}) - \dot{N}_{\text{Load}} h(T_{\text{Load}}) + \dot{N}_{\text{HX}} h(T_n) + Q_{\text{in}} \tag{42}$$

where i is the number of control volumes.

Conductive heat transfer between nodes is solved using Fourier's law throughout the model. The properties of water for conductive heat transfer are used.

$$Q_{\text{in}} = \frac{kA}{L}(T_{i-1} - T_i) \tag{43}$$

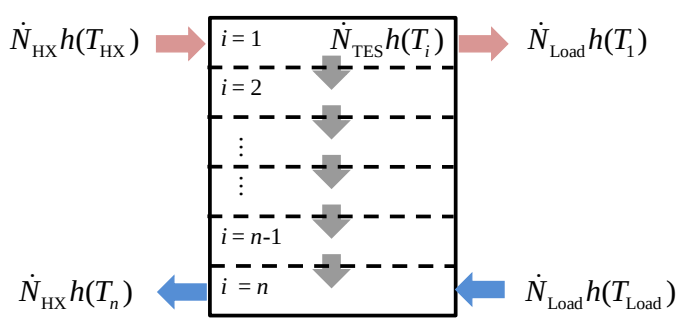

Figure 14: Schematic of modeled thermal energy storage tank, showing model nodes and internal flow configuration.

2.6.1 TES Model Verification

Important model parameters and simulation conditions are provided in Table 2. All values correspond to the published experimental data (Wildin & Truman, 1985) except for the geometric data of the tank. Since the literature did not mention the geometry of the tank, a column tank with height to diameter ratio of 3 is assumed in the current model.

Table 2 Simulation conditions for validation of the TES model

Number of nodes, *n*	50	-
Tank volume, V_{TES}	16,000	Gallon
Tank diameter, D_{TES}	2.95	m
Tank height, H_{TES}	8.85	m
Cross sectional area of the Tank, *A*	6.83	m^2
Distance between control volumes, *L*	0.177	m
Height to diameter ratio of the tank, H/D	3	-
Density of the liquid water, ρ	999.7	kg m^{-2}
Heat conductivity of water, *k*	0.00058	kW $m^{-1}K^{-1}$
Inlet/Outlet flow	0.1	kmol s^{-1}
Inlet temperature	60	°F
Initial temperature	42	°F
Ambient temperature, T_{amb}	77	°F

Time ordinary differential equations for each control volume are solved using the Simulink® stiff differential equation solver ODE 15s. Dynamic simulation of a full discharge cycle has been conducted and compared to available experimental data as shown in Figure 15 (b). Note that this simulation is conducted for a TES that provides cooling water in order to compare with published experimental data (Wildin & Truman, 1985).

Figure 15 shows the comparison of current TES simulation result to the literature experimental result. The plot in the simulation result shows the temperature distribution in the tank at 15, 100, 200 300, 400, and 520 minutes after the start of discharging, respectively. In the experimental result, the lines (called thermoclines) show the temperature distribution at each time. The simulation result shows the dynamic change of the thermoclines in the tank at the same times showing that the current TES model results correspond well with the experimental data.

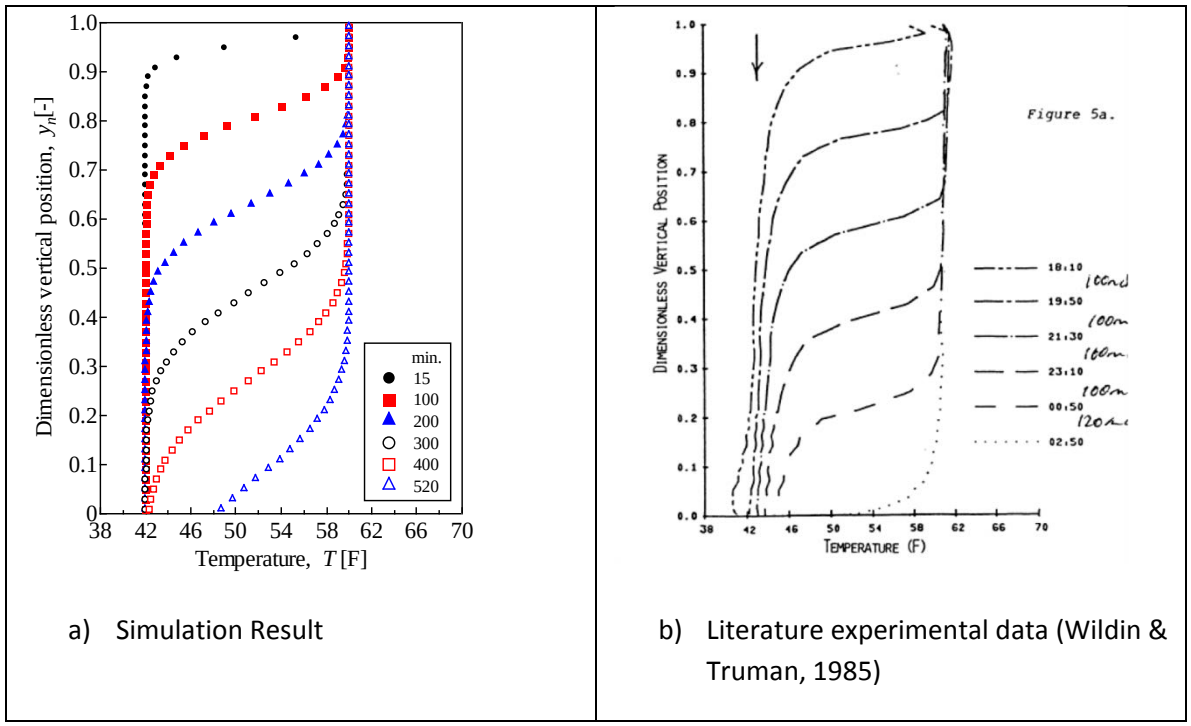

a) Simulation Result

b) Literature experimental data (Wildin & Truman, 1985)

Figure 15: Comparison of temperature distribution to experimental testing data, showing in full scale distributed nozzle tank during discharging for final cycle of complete charge-complete discharge test

3 UCI Renewable Resource Models

The UCI Microgrid's renewable resources will be modeled using the HiGRID tool's renewable module (see (Samuelsen et al., 2013)). Only the two-axis tracking concentrated photovoltaic (dual-axis CPV) and fixed-plate photovoltaic (fixed-tilt PV) models in the HiGRID tool's renewable module will be discussed in detail in this section. This is because local wind is not a viable option (see (Samuelsen et al., 2013)). The location and capacity installed of the dual-axis CPV and/or fixed-tilt PV is input into the HiGRID tool's renewable module.

3.1 Solar Resources

The University of California Irvine campus has installed nearly 1MW of fixed-plate fixed-tilt PV systems and 113 kW of concentrated fixed-tilt PV Amonix systems (two Amonix 7700 dual-axis CPV systems). This section will describe how these two systems have been modeled and what solar data have been used as inputs to the models.

3.1.1 Amonix dual-axis CPV 7700 Installation

The Amonix installation is located at the eastern side of the University of California, Irvine campus at 33° 38' 23.29" N, 117° 49' 30.33" W. The site contains two Amonix 7700 dual-axis CPV systems with a combined peak output rating of approximately 112kW. The record maximum AC power output was measured at 126.19kW at 999.94W/m^2 direct normal insolation (534m^2 lens area), yielding an overall system efficiency of 23.63%. Each system contains a 21 x 12 module array mounted on a two-axis

tracker and a Solectria 7700 PVI inverter. The UC-9 branch circuit that connects the installation to the UCI microgrid also services the student recreation center, which represents an average load of approximately 300 kW. Data have been collected over the course of 443 days (June 5th, 2012 to Sept 5th, 2013) at a 1-minute granularity from each dual-axis CPV panel and at the points of common coupling of the inverters and the recreation center. An onsite weather station gathers insolation and meteorological data at the same sampling rate.

Figure 16: Two Amonix dual-axis CPV-7700 Systems at the University of California, Irvine.

3.1.2 Fixed-Plate Solar fixed-tilt PV Installations

In addition to the 120kW Amonix installation, the campus hosts an additional 900kW of flat plate fixed-tilt PV generation located at 11 locations throughout the campus. The unique combination of a high fixed-tilt PV penetration and on campus generation allows for detailed comparative studies on fixed-tilt PV connected to microgrid circuits. Figure 17 and Table 3 summarize additional campus solar resources.

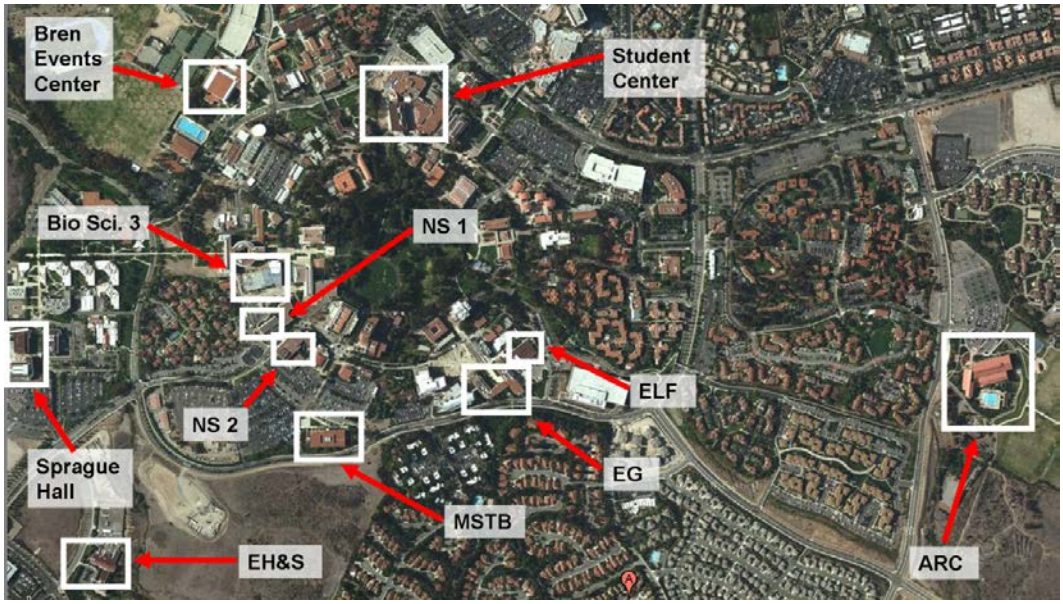

Figure 17: UCI fixed-tilt PV Resources

Table 3: Capacity of Additional UCI fixed-tilt PV Resources.

Location	fixed-tilt PV Capacity (kW)	Circuit
Engineering Gateway	48	UC-9
Sprague Hall	55	UC-2 / UC-6
Biological Sciences	63	UC-1 / UC-6
McGaugh Hall	65	UC-8
Student Center 1	29	UC-6
Student Center 2	56	UC-6
Multipurpose Sci. & Tech.	92	UC-1
Natural Sciences 1 (NS 1)	37	UC-8
Natural Sciences 2 (NS 2)	56	UC-8
Env. Health & Safety Sciences	118	UC-10
Bren Events Center	118	UC-3
ARC	150	UC-9
Engineering Lab Facility	5	UC-9

Solar power includes both photovoltaic and solar thermal technologies. For solar photovoltaic technologies radiation data from the National Solar Radiation Database (NSRDB) were selected for different sites in California including: 1) coastal sites like Santa Ana, Santa Maria and Miramar, 2) desert sites like Daggett-Barstow, Palm Springs, Twenty-nine Palms and Edwards Air Force Base, and 3) inland sites like Bakersfield Meadows and China Lake. Transmission and resource restrictions are considered in a similar manner as that for wind generation. Technologies include fixed plate, 1-axis tracking and two-axis tracking photovoltaic panels.

3.1.3 Solar Data Acquisition

For the purposes of the HiGRID code, solar power production is modeled by utilizing irradiation data obtained from the NSRDB developed by NREL as inputs to first-principles-based models of solar photovoltaic panels and solar thermal power cycles. The dataset includes the different components of irradiation (direct, diffuse) and is converted into an effective total (in-plane) irradiation via a model constructed in house. Data from the NSRDB is available for most sites from 1991 through 2005. The database contains hourly-resolved irradiation measurements from a variety of sites spread throughout the U.S, as shown in Figure 18:

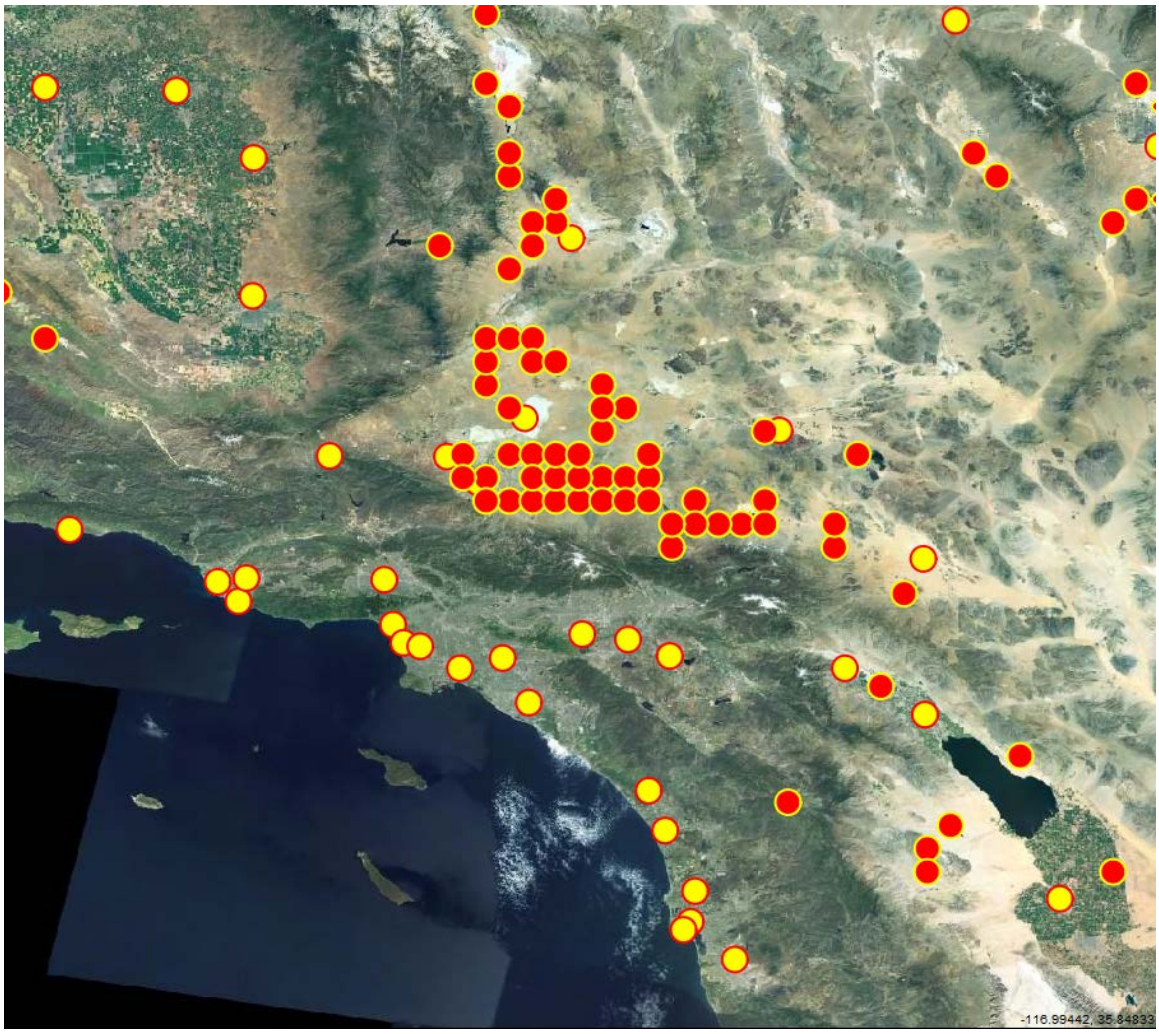

Figure 18: Location of NSRDB Solar Irradiation Measurements (Yellow)

A separate, in-house analysis showed that for solar power profiles composed of a large amount of solar farms that are spaced apart by a sufficient amount such that their cloud-pass sequences are decoupled, the fast-timescale fluctuations in irradiation become a smaller and smaller fraction of the total solar power output and the total profile converges towards its longer-timescale average. This effect is presented in Figure 19 utilizing irradiation data with a 5-minute resolution for the case of a) 1 site, b) 3 sites, c) 5 sites, and d) 8 sites spread across the state of Oregon, respectively.

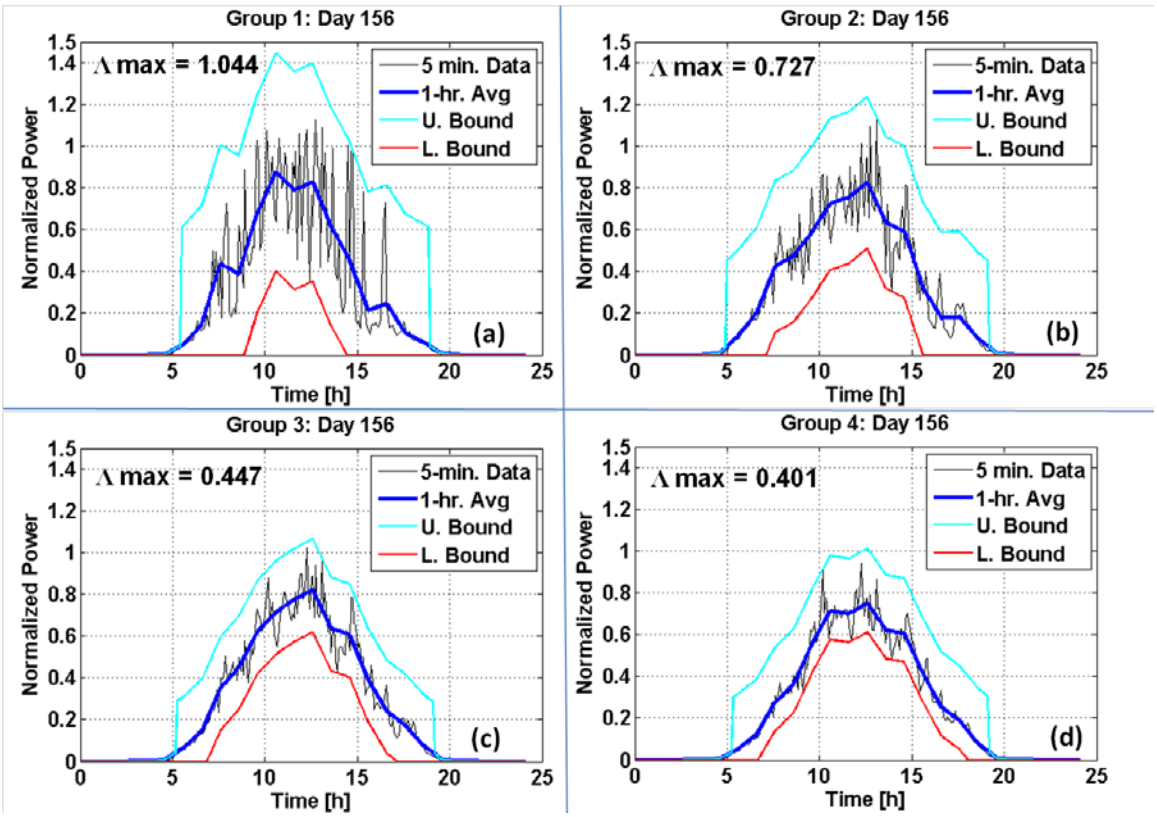

Figure 19: Decrease in Magnitude of Fast-Timescale Fluctuations in Irradiation Profiles based on a) 1 site, b) 3 sites, c) 5 sites, d) 8 sites

Therefore, for a large-scale system such as the transmission grid that utilizes multiple solar farms that are spread across large distances, it is reasonable to utilize hourly resolved irradiation data as the input to model solar power production.

The use of this dataset allows for the construction of total solar power profiles from solar farm installations that may be present at a variety of sites ranging from large desert installations to distributed coastal installations such as the rooftops of buildings. In the HiGRID code, the nameplate capacity of solar farms at different sites is specified as an input, and appropriately scaled profiles from the different regions are combined to create the aggregate solar power profile. Different technologies such as fixed-plate, 1-axis tracking, and 2-axis tracking can be specified for each individual solar farm, and the different technologies utilize slightly different power profiles produced by in-house models.

3.1.4 Solar Irradiation Module

Solar power-producing devices such as photovoltaics are capable of producing electrical power from both direct and indirect light inputs. Therefore, the total irradiation that is incident on the photovoltaic cell must be calculated from the different irradiation components.

Calculation of the in-plane irradiation on the solar array is done using the exact model constructed in Heling (Heling, 2008). The model reads files containing hourly data for different types of solar insolation for a given location:

Direct "beam" insolation (B) is the component of the sun's radiation which arrives on a horizontal surface at ground level without interruption, in a straight line from the sun.

Indirect "diffuse" insolation (D) is the component of the sun's radiation which arrives at a horizontal surface at ground level after being reflected from atmospheric objects such as clouds and airborne particles.

An additional given parameter is the global horizontal irradiation (H), which is the amount of total (beam and diffuse) irradiation striking a horizontal surface at ground elevation.

The model uses the different types of insolation to calculate in-plane beam irradiation (I_b), the in-plane diffuse irradiation (I_d), and the in-plane irradiation that is reflected from the ground. (I_r). The total in-plane irradiation on the solar panel is then:

$$I = I_b + I_d + I_r \tag{44}$$

3.1.4.1 Calculation of in-plane beam irradiation and in-plane reflected irradiation

The in-plane beam irradiation is calculated according to the following method using the solar declination and the true solar time:

The solar declination, which is the angle between the earth's equatorial plane and a straight line drawn between the center of the earth and the center of the sun, is calculated for locations north of the equator as:

$$\delta = 23.45^\circ \sin\left[\frac{360(d_n + 284)}{365}\right] \tag{45}$$

where d_n is the serial number of the day of the year.

The true solar time, which is the difference between noon and the considered hour of the day in terms of a complete revolution of the earth, is calculated as:

$$\omega = 15 \times (TO - AO - 12) - (LL - LH) \tag{46}$$

where TO is the local time, AO is the time by which the clocks are advanced ahead of local time zones, LL is the longitude of the site in consideration, and LH is the reference longitude of the local time zone encompassing the site in consideration. Note that TO and AO are in hours, and LL, LH are in degrees.

The solar declination and true solar time are used to calculate the angle of solar incidence θ_s, which is the angle between the sun and the line that perpendicular to the face of the photovoltaic array:

$$\begin{aligned}\cos\theta_s = {} & \sin\delta\sin\phi\cos\beta - \sin\delta\cos\phi\sin\beta\cos\alpha + \cos\delta\cos\phi\cos\beta\cos\omega + \ldots \\ & \cos\delta\sin\varphi\sin\beta\cos\alpha\cos\omega + \cos\delta\sin\alpha\sin\omega\sin\beta.\end{aligned} \tag{447}$$

where Φ corresponds to the latitude of the site under consideration.

The total in-plane beam irradiation is then calculated by:

$$I_b = B\max(0, \cos\phi_s) \tag{48}$$

The total in-plane reflected irradiation can also be calculated by:

$$I_r = \rho_g H \frac{1-\cos\beta}{2} \tag{49}$$

where ρ_g is the reflectivity of the ground.

3.1.4.2 Calculation of the in-plane diffuse irradiation

The in-plane diffuse irradiation is calculated according to the model presented by Perez (Perez, 1990), represented by:

$$\theta_Z = \cos\phi\cos\delta\cos\omega + \sin\phi\sin\delta \tag{50}$$

$$I_d = D\left[\frac{(1-F_1)(1+\cos\beta)}{2} + F_1\frac{a}{b} + F_2\sin\beta\right] \tag{51}$$

Where F1 and F2 are functions of the sky condition, found from tables presented in Perez, 1990, and θ_z is the solar zenith angle as calculated by Duffie, 1991. The values for a and b are calculated according to:

$$a = \max(0, \cos\theta_s) \tag{52}$$

$$b = \max(0.087, \cos\theta_Z) \tag{53}$$

3.1.5 Fixed-Plate Solar Photovoltaic Model

The fixed-tilt PV model captures the effect of solar irradiance, cloud cover, and ambient temperature on the array outlet power, dynamically capturing the intermittent nature of solar fixed-tilt PV power. The model integrates (1) a power equivalent circuit model and (2) an energy balance based fixed-tilt PV cell temperature model. The developed model is tuned to represent experimentally measured data of a Solarex MSX-60 panel installed on top of the Engineering Laboratory Facility at the University of California, Irvine. The developed model output is scaled to simulate any sized solar installation parametrically.

3.1.5.1 fixed-tilt PV Power module

The model was developed based on an equivalent circuit representation of a solar cell as presented in Walker (Walker, 2001) with temperature dependence of the diode saturation current (I_o) and photo-current (I_L), and the inclusion of a series resistor. The circuit diagram is presented in Figure 20.

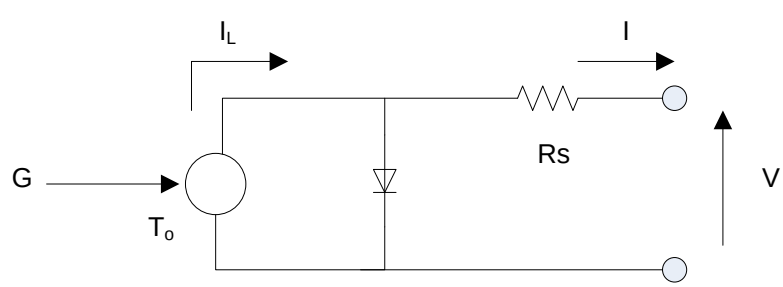

Figure 20: Equivalent Circuit Representation of a Solar Cell

The operating current throughout the panel circuit is determined from the Shockley diode Equation and Kirchoff's current Law:

$$I = I_L - I_o(e^{q(V+IR_S)/nkT} - 1) \tag{54}$$

The limiting current of the panel is assumed to have a linear temperature dependence, where the slope is determined from the short circuit current at different temperatures:

$$I_L = I_{L(T1)}(1 + K_o(T - T_1)) \tag{55}$$

$$K_o = (I_{SC(T_2)} - I_{SC(T_1)})/(T_2 - T_1) \tag{56}$$

The reference limiting current is assumed to have a linear dependence on the magnitude of the incident solar irradiation:

$$I_{L(T1)} = G \cdot I_{SC(T_1,nom)} / G_{(nom)} \tag{57}$$

The diode saturation current is dependent on temperature and is given by:

$$I_o = I_{o(T_1)} \cdot (T/T_1)^{3/n} \cdot e^{-qVg/nk\cdot(1/T - 1/T_1)} \tag{58}$$

$$I_{o(T_1)} = I_{SC(T_1)} / (e^{qV_{OC}(T_1)/nkT_1} - 1) \tag{59}$$

Where the variables are as follows:

Table 4: Power Module Variables

Variable	Quantity	Value	Units
I	Operating Current	--	A
I_o	Diode Saturation Current	--	A
I_L	Photo-current	--	A
T	Temperature	--	K
T_1	Reference Temperature	298	K
G	Irradiation	--	$W\ m^{-2}$
R_s	Series Resistor	0.003	Ohm
I_{SC}	Short Circuit Current	3.8	A
K_o	Slope of Current vs. Temperature curve	--	A/K
V_{OC}	Open Circuit Voltage	0.585	V
q	Charge	--	C
n	Diode Quality Factor ($1 < n < 2$)	1.2	--
V_g	Band Gap Voltage	1.12	V
k	Boltzmann's Constant	1.38×10^{-23}	$J\ K^{-1}$
V	Operating Voltage	--	V

3.1.5.2 fixed-tilt PV Cell Temperature Module

The temperature of the solar cell was determined by applying conservation of energy to a control volume encompassing the entire 5 kW solar array. Heat transfer due to convection and radiation was resolved, however conduction was assumed to be negligible since the contact area of the panel interconnects with the roof is very small.

$$\rho \forall C_v \frac{dT_s}{dt} = Q_{rad} - Q_{conv} - Q_{rad,loss} - W \tag{60}$$

Convective heat transfer was determined using a turbulent-flow Nusselt number approach for a flat plate:

$$\overline{Nu} = \frac{\overline{h}L}{k_f} = 0.664\, Re_L^{0.5}\, Pr^{0.33} \tag{61}$$

Where Re_L is the Reynolds number of the ambient flow, Pr is the Prandtl number, k_f is the thermal conductivity of the ambient air, L is the length of the plate, and A_s is the surface area of the array.

The density, dynamic viscosity, thermal conductivity and Prandtl number are all temperature dependent. The velocity of the ambient air is taken from measured wind speed data in the Santa Ana region for the appropriate time period.

Radiative heat transfer was modeled using the grey body assumption, where the temperature of the grey surface is set to the ambient temperature:

$$Q_{rad} = \left(G_{measured} - \varepsilon\sigma\left(T_s^4 - T_\infty^4\right)\right)A_s \tag{62}$$

where $G_{measured}$ is the in-plane solar irradiation on the panel, calculated from the irradiation module. In addition, a radiative heat loss was included to account for the absorptivity of the ambient atmosphere and any cloud cover that might be present. This loss is also modeled with a grey body, where the temperature of the grey body is set to the ambient temperature minus 2 degrees Kelvin, and the emissivity of the grey body is dependent on the ambient relative humidity and cloud condition:

$$Q_{rad,loss} = \varepsilon(\%RH, \text{Cloud})\sigma A_s\left(T_s^4 - (T_\infty - 2)^4\right) \tag{63}$$

Where:

$$\varepsilon(\%RH, \text{Cloud}) = 1 - \left(\frac{\varepsilon_{RH} + \varepsilon_{Cloud}}{2}\right) \tag{64}$$

Where ε_{RH} and ε_{Cloud} are the emissivity indices of the grey surface due to relative humidity and cloud cover, respectively:

Table 5: Relative Humidity Emissivity Indices

Relative Humidity (%)	Relative Humidity Index
RH < 65%	0
65%< RH < 70%	0.1
70% < RH < 75%	0.25
75% < RH < 80%	0.4
80% < RH < 85%	0.5
85% < RH	0.8

Table 6: Cloud Condition Emissivity Indices

Cloud Condition	Cloud Condition Index
Clear	0
Few	0
Scattered	0.05
Broken	0.25
Overcast	0.65
Haze	0.8

This approach greatly simplifies the calculations needed to determine the temperature of the solar cell. Notice that as the cloud cover or relative humidity increases, the radiation loss decreases, representing the effects of atmospheric radiation absorption and re-radiation. This assumption was made since it was deemed unnecessary to develop a physics of weather simulation for the purpose of determining the temperature of the solar cell, since the variation in the performance of the cell over the temperature range considered is relatively small, however it is significant enough to be included.

3.1.5.3 Fixed Plate Photovoltaic Model Verification

The model was constructed to simulate the performance of a Solarex MSX60 60W solar panel array. Model validation of the power module was carried out by comparing simulation results to power data obtained from a 3.85 kW solar array on the rooftop of the Engineering Laboratory Facility at the University of California, Irvine. The simulated irradiation and cell temperature were used as inputs to the power module, and the results were compared to the measured power data. The individual 60W panel was scaled up to 3.85 kW for comparison.

The combined model was validated against measured power, cell temperature, and irradiation data from a 3.85 kW solar panel array on the roof of the Engineering Laboratory Facility at the University of California, Irvine.

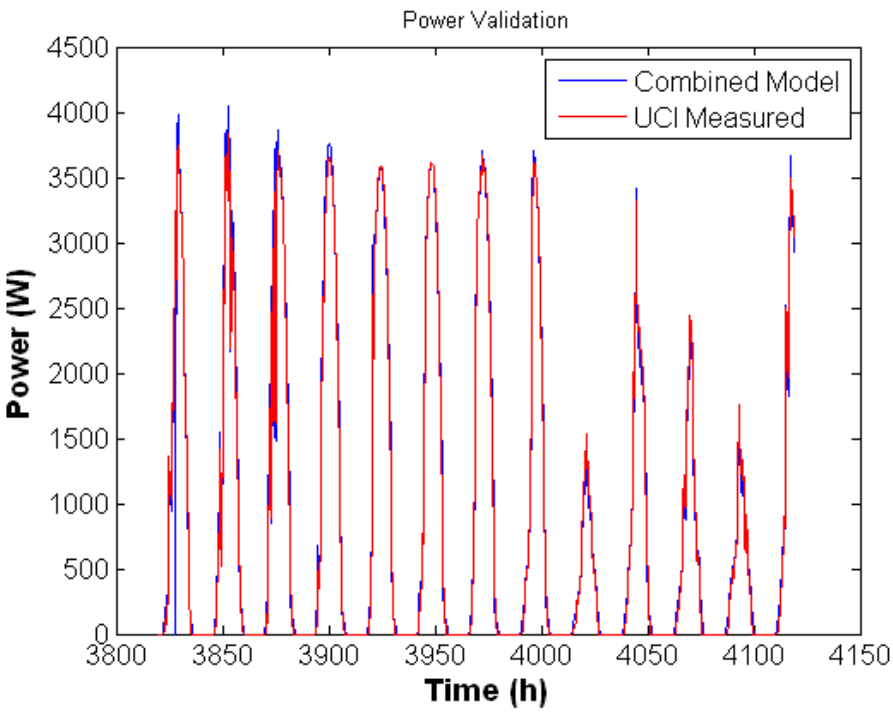

Figure 21: Solar Model Validation: Power Module

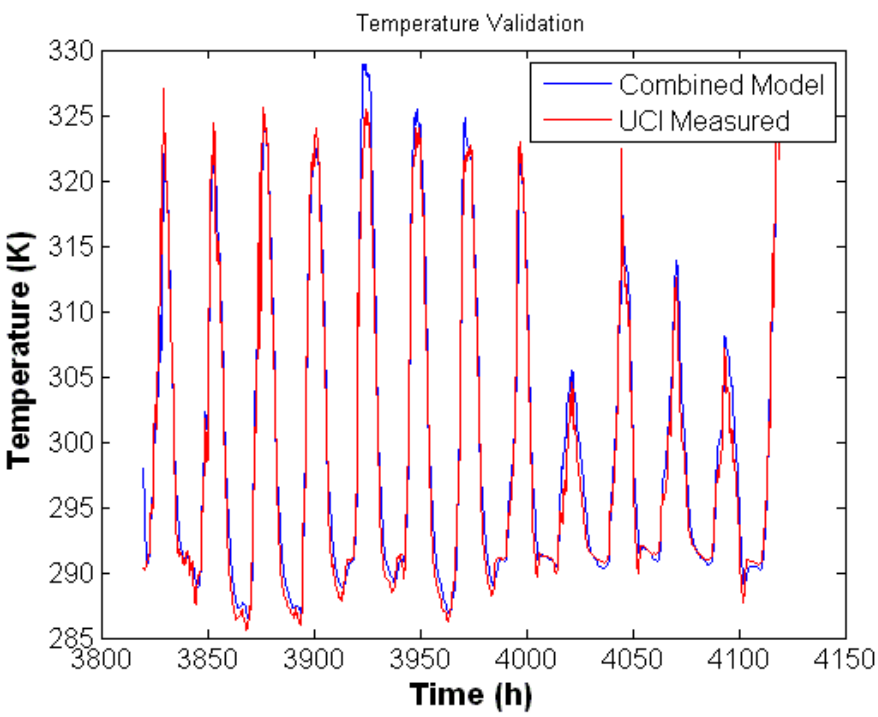

Figure 22: Solar Model Validation: Temperature Module

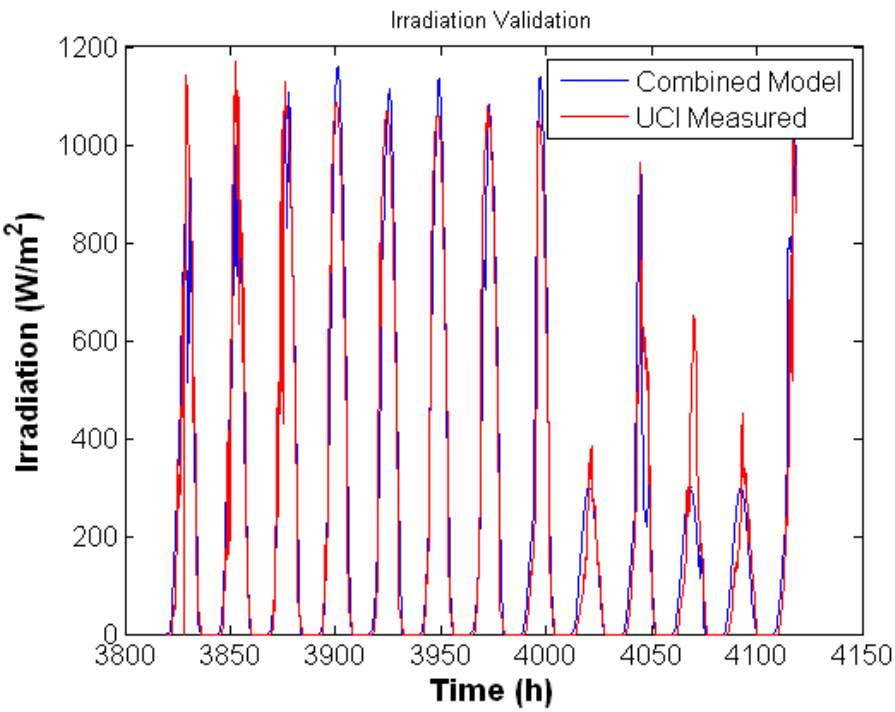

Figure 23: Solar Model Validation: Irradiation Model

From Figure 21, Figure 22, and Figure 23 the combined model results match with the measured data with an average error of 1.36%. Therefore, it is safe to assume that a more detailed model for determining the effective irradiation, power output, or cell temperature is not necessary for this level of analysis.

3.1.6 Amonix 7700 dual-axis CPV Model

3.1.6.1 dual-axis CPV Power Module

The dual-axis CPV power module uses multi-junction cell experimental data from Spectrolab. Spectrolab manufactures the Concentrator 3rd generation MultiJunction cell (C3MJ), which is used in Amonix panels. Figure 24 shows the data used to calculate the power output of each cell. Using Figure 24, the lens concentration (240), and the cell temperature, the cell efficiency can be calculated. The cell efficiency multiplied by the incident radiation on the cell will provide the power output of the cell.

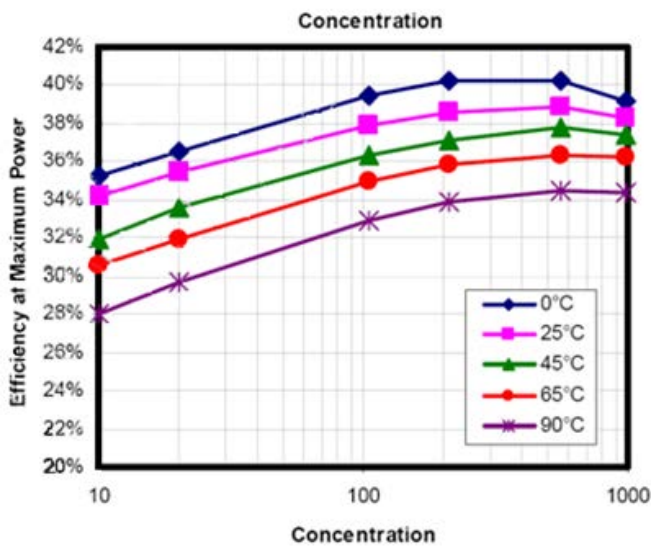

Figure 24: Performance data from Spectrolab's Concentrator 3rd generation MultiJunction cell (CDO-030-C3MJ) (Spectrolab, 2010)

The incident radiation is calculated using a model of a maximum power point tracking (MPPT) controller as shown in Figure 25. This MPPT controller model is applied to the azimuth and tilt angles in order to simulate the two axis tracking of the Amonix 7700 panels. To get the total dual-axis CPV system power, the output of each cell is multiplied by the number of panels as specified in Table 7.

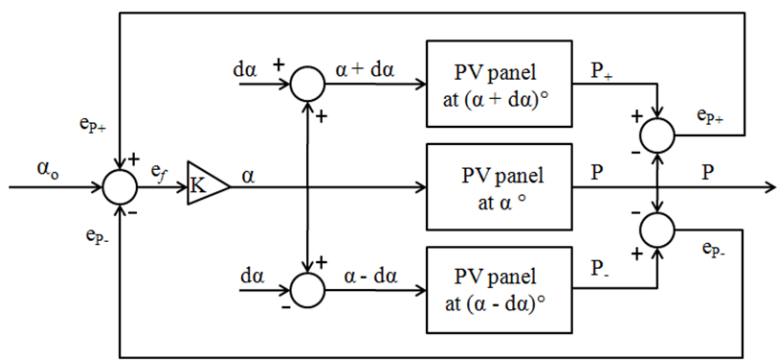

Figure 25: Maximum power point tracking controller model

The losses associated with the other balance of plant in the Amonix 7700 system is accounted for by a second order polynomial loss equation that was fitted to data sheet specifications shown in Equation 65. In this equation A,B, and C are constants and P is the the power produced. These values are shown in Table 7.

$$\mathrm{BOP_{Loss}} = \mathrm{A} + \mathrm{BP} + \mathrm{CP}^2 \tag{65}$$

Table 7: Dual-axis CPV Model Specifications

No.	Parameter		Value	Units
1	Solar Cell (CDO-030-C3MJ)	Aperture length	0.555	cm
2		Aperture width	0.554	cm
3		Aperture thickness	0.019	cm
4		Aperture Area	3.0747×10^{-5}	m^2
5		Cell Density	2330	Kg m^{-3}
6		Specific heat capacity	710	J/ (kg.K)
7		Cell Volume	5.84193×10^{-9}	m^3
8		Overall heat transfer coefficient	2.3256	W/K
9		Reference intensity for defining concentration	900	W m^{-2}
10		Concentration	240	--
11	Solar Panel (Amonix 7700)	Panel Height	49	ft
12		Panel Width	72	ft
13		Panel Area	327.762	m^2
14		Number of Mega-modules	7	--
15		Solar cells in series per Mega-module	576	--
16		Series in parallel per Mega-module	2	--
17		Total number of solar cells	8064	--
18	BOP constant	A	0	W
19		B	0.40	--
20		C	1.5×10^{-6}	W^{-1}

3.1.6.2 Dual-axis CPV Temperature Module

The dual-axis CPV temperature module is the same as the fixed-plate temperature module.

3.1.6.3 Dual-axis CPV Model Verification

The dual-axis CPV model was compared to experimental data from several locations (Dagget, CA; Las Vegas, NV; Phoenix, AZ; Alamosa, CO) (Kinsey, Nayak, Liu, & Garboushian, 2011). Both the energy yield and energy yield error are shown in Figure 26. The model is represented by the line and the field data are represented by symbols. The percent error of the model does not exceed 6% for all the locations and is affected by the error in the DNI data input into the model versus the data collected at the locations as shown in Kinsey (Kinsey et al., 2011).

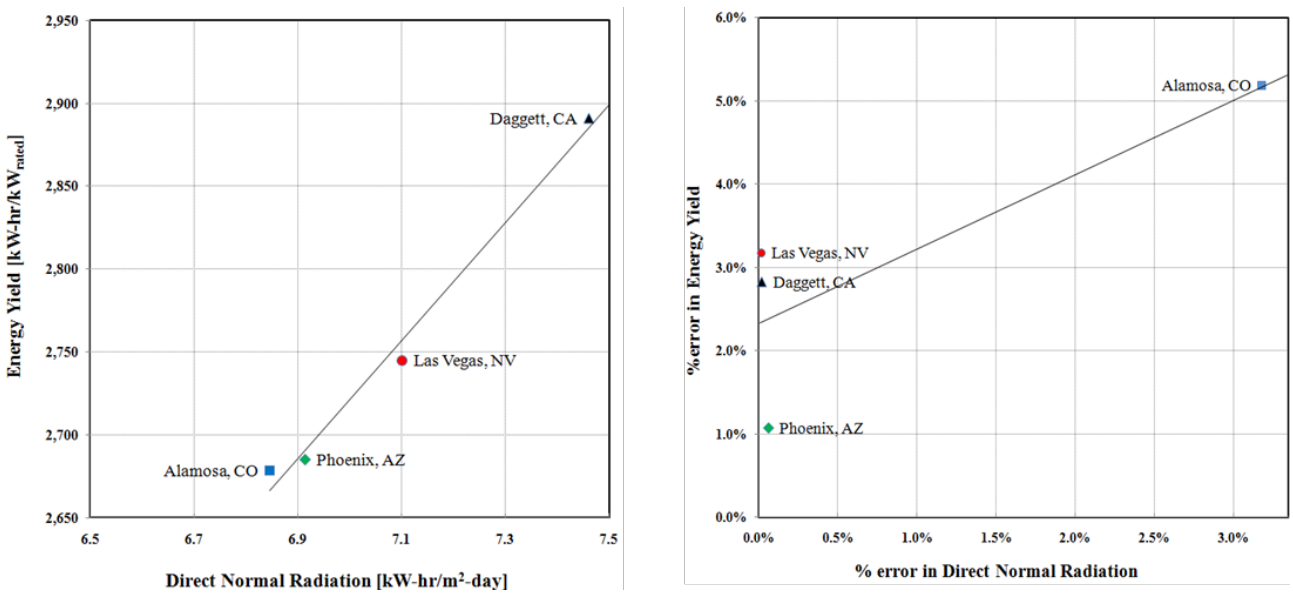

Figure 26: Dual-axis CPV model (line) verification using field data (symbols)

3.2 Wind

Local wind is not investigated here as it was found in the RESCO project (Samuelsen et al., 2013) to not be a viable resource given the local wind potential.

4 Future Resource Models

4.1 Renewable

The future renewable resource models considered in this report are only fixed-plate fixed-tilt PV and Amonix dual-axis CPV. Therefore, the models described in the previous sections will serve as those used for future resource projections.

4.2 Battery Energy Storage Model

Battery energy storage is another possible future resource. The campus currently has an arrangement for the future demonstration of a 2MW/0.5MWh battery for several months at the campus. However, the battery modeled in this work is a Vanadium-Redox Flow battery with a larger power capacity and energy storage capacity such that the energy storage system would have a larger impact on the campus operations. The electric energy storage model is a physically-driven, rule-based model. It uses the system's physical behavior and operation to advise the rule-based constraints imposed. Following the logic in Figure 27, any signal can be inputted into the model including demand, renewable signal, etc. Next, the maximum load value in the demand signal is reduced by a small increment while the nearest earlier minimum is increased and assessed an energy penalty due to inefficiencies of charging the system. The ramp rate, power capacity, energy capacity and other operational constraints are checked to ensure they are not violated for the resulting signal. If these conditions are violated then the current iteration resets to the initial values and reruns. This process continues until the available power and energy capacity for every available time step is exhausted.

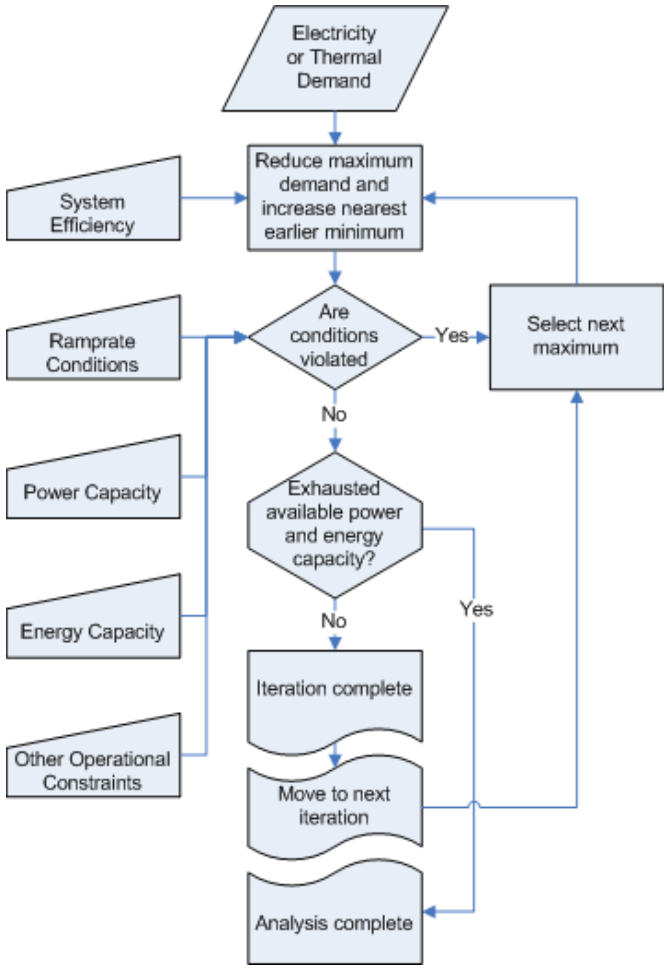

Figure 27: Flowchart of Energy Storage Model

This control strategy shifts the maximum amount of load without violating any of the system constraints. The figures below show one example of the energy storage process that is modeled. Figure 28 depicts the peak to trough shifting described. Figure 29 and Figure 30 show the cumulative energy capacity and power demand, respectively. Notice the associated energy penalty for charging the system. This penalty is the energy that is lost in conversion or storage and does not contribute to the amount of generation.

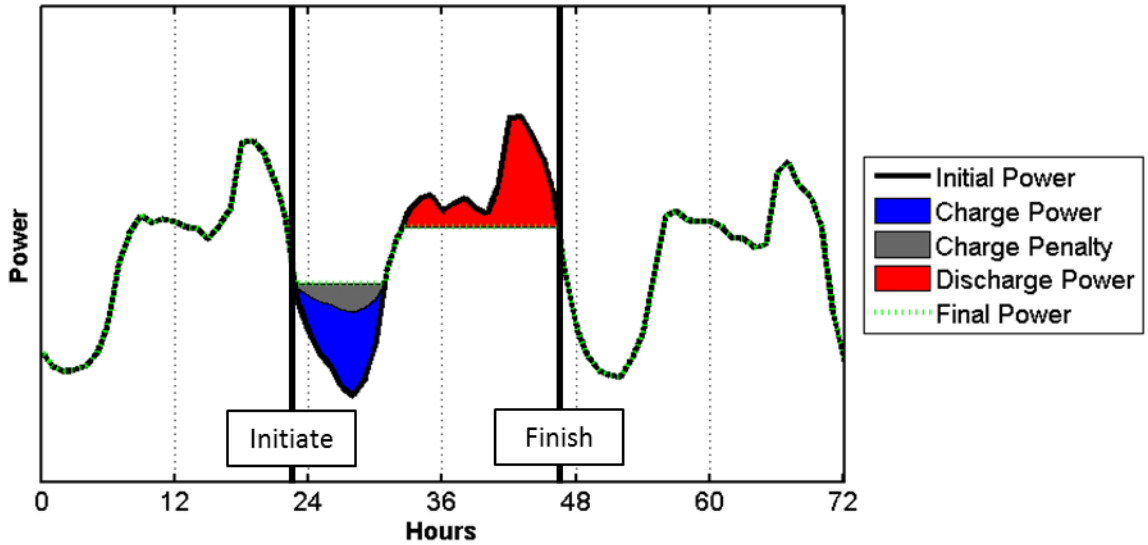

Figure 28: Energy Storage Model Effect on Example Demand Signal

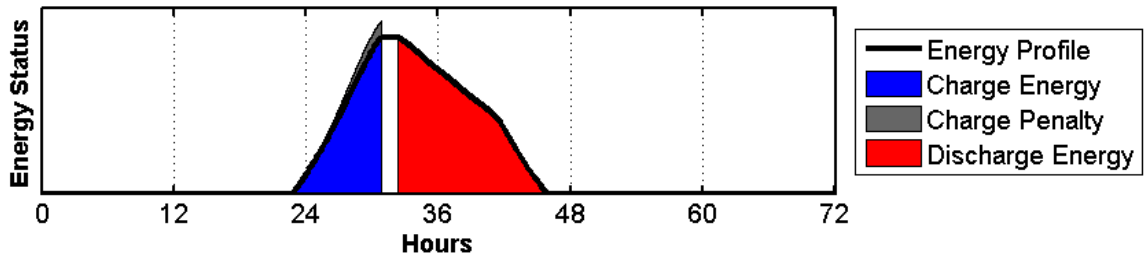

Figure 29: Cumulative Energy Capacity of Energy Storage System

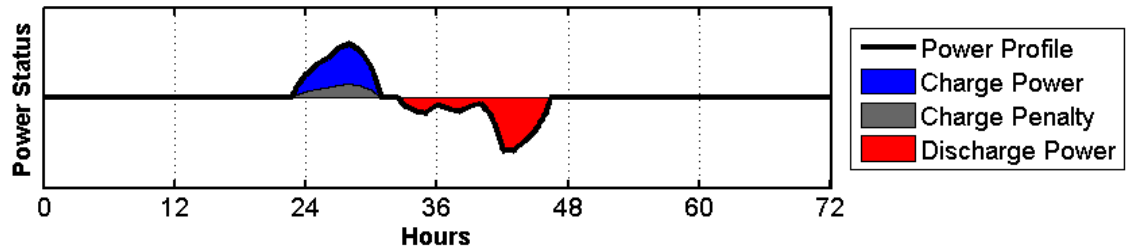

Figure 30: Power Demand of Energy Storage System

Information from the three figures above provides a complete picture of the operation of the model. While Figure 28 shows the resulting effect on the initial demand signal, Figure 29provides information about the current and total energy capacity of the device. Lastly, the information used to generate

Figure 30constrains the charging and discharging power capacity as well as the ramp rate of the system, since the derivative of the power status signal is the ramp rate.

In addition to the efficiency, power capacity, energy capacity and ramp rate of the system, the model considers variable charging and discharging power and has the ability to include additional operation characteristics dependent on the technology type. However, for these analyses, the Vanadium-Redox flow battery was considered.

In this particular example, the energy storage system is assumed to be a Vanadium Flow Battery with the following parameters:

Table 8: Vanadium Flow Battery System Parameters

Power Capacity [MW]	Rated Discharge Time [h]	Energy Capacity [MWh]	Round Trip Efficiency
5	4	20	0.85

4.3 Optimized Chiller Plant Dispatch

To examine the effects of dispatching cooling loads optimally at the community scale, a cost function was developed to simulate an optimal chiller/TES dispatch and compare it to the existing chiller/TES dispatch procedures.

4.3.1 Cost Function Components

The dispatch behavior of the central plant chillers with TES capability was simulated by allowing the system to respond to a cost function, which weighted certain metrics that pertain to the utility-grid behavior or campus demand behavior with more or less priority.

The cost function used in these analyses has two components.

1. A **utility component** which represents a real-time electricity rate that is designed to promote chiller dispatch to benefit the transmission grid by penalizing peak campus power use and increasing power demand during periods of high electric load on the bulk transmission grid. More specifically:

$$Cost_u = k_u \left(\frac{P_{grid}}{P_{grid\,,max}} + \; max\left(\frac{P_{chil}}{P_{chil,max}} \right) \right) \tag{45}$$

Where P_{grid} is the load demand on the bulk transmission grid, P_{chil} is the power demand of the aggregated chiller plant, and k_u is a constant which weights the priority of this behavior and can translate this component into a dollar per kilowatt hour amount. The first fraction represents the normalized load demand on the bulk transmission grid. Therefore, during periods of high grid load, the associated cost penalty is higher. The second fraction represents the normalized power demand of the aggregated chiller plant on the UCI campus and penalizes excessively high power use. Setting this

component to a high priority (high k_u value) will promote the dispatch of the chiller plant to operate during periods of low grid load and minimize absolute power demand requirements.

2. An **energy component** which evaluates the energy required to provide the cooling necessary to prevent the TES tank from becoming empty:

$$Cost_e = k_e(P_{chil}) \tag{46}$$

Where k_e is a constant which weights the priority of this behavior and can translate this component into a dollar per kilowatt hour amount. While the amount of cooling required is set by the cooling load, the magnitude of the actual power used to provide that cooling is dependent on the coefficient of performance (COP) of the chillers in the chiller plant. The COP is unit specific and generally depends on the mass flow rate of water and the wet-bulb or ambient temperatures. When this component is given a high priority (high k_e), the chiller plant will be dispatched to minimize the total amount of energy consumed to provide the required cooling demand, operating in the most efficient manner possible.

The cost function is a combination of these two components:

$$Cost = k_u\left(\frac{P_{grid}}{P_{grid\ ,max}} + \ max\left(\frac{P_{chil}}{P_{chil,max}}\right)\right) + k_e(P_{chil}) \tag{47}$$

Using this cost function, isolated and combined dispatch behaviors can be simulated. Setting either of the k constants to zero eliminates the corresponding component from influencing the cost, therefore the chiller plant will not respond to the behavior prioritized by that component. In these analyses, three cases are examined in particular.

1. **Utility-Biased:** In this case, the priority of the chiller dispatch is to benefit the electric grid, and cooling loads at the community level are dispatched in response to transmission grid load characteristics. The local considerations of chiller efficiency are not addressed, and the primary controlling entity is the electric utility. This case represents a limiting scenario where community cooling loads can be used as distributed, dispatchable energy resources by the utility or balancing authority to mitigate issues on the bulk transmission grid.

2. **Chiller-Biased**: In this case, the priority of the chiller dispatch is to minimize the energy used to provide the necessary cooling. The behavior of the bulk transmission grid is not considered, and the campus operates independently of the properties of the electric grid load. To achieve this, the chiller plant will operate in the most efficient manner possible, regardless of the effect that it has on influencing the characteristics of the electric grid load. This represents a limiting scenario where community resources are not controlled by any extent by the electric utility or balancing authority, and communities act independently of each other.

3. **Combined Case:** In this case, the chiller dispatch responds to electric grid load characteristics and energy use considerations with equal priority. This is a compromise between the chiller-biased and utility-biased cases where both considerations are addressed.

A summary of the three cases as implemented in the optimization code is presented in Table 9:

Table 9: Chiller Dispatch Behavior Parameters

Case	k_u	k_e
Utility-Biased	1	0
Chiller-Biased	0	1
Combined	1	1

4.3.2 Chiller Optimization Code

The cost functions and associated dispatch behaviors described previously are simulated by the use of a chiller dispatch optimization code which determines the temporal operation of the aggregated chiller plant such that the case-specific cost function is minimized.

To utilize the following chiller optimization code, a number of data sets and model tables are required as inputs:

1. Temporally resolved cooling demand for the UCI campus for an entire year (Tons).
2. Temporally resolved building electric loads for the UCI campus for an entire year (MW).
3. Temporally resolved wet-bulb temperature at the UCI campus for an entire year (F/C).
4. Model table that determines the combined coefficient of performance of the aggregated chiller plant as a function of wet-bulb temperature and water flow rate (Unit-less).
5. Model table that determines the aggregated chiller plant power as a function of COP and water flow rate (MW).

The temporally resolved data sets were obtained from UCI campus facilities and associated measurements. The model tables were obtained from results produced by the UCI campus cooling system model described previously.

Once the code is executed, it will provide the following outputs:

1. Temporally resolved chiller plant power for the entire year (MW).
2. Temporally resolved total campus load demand for the entire year (MW).
3. Temporally resolved TES level profile for the entire year (%).
4. Total chilling energy consumption for the entire year (MWh).

4.3.2.1 Optimization Strategy

The basic operation of the code that determines the chiller power profile associated with different dispatch behaviors is described herein.

1. At the first time-step in the beginning of the year, the TES tank is assumed to be full. As time moves forward, the corresponding raw cooling demand at each time-step is subtracted from the TES capacity until a point is reached where the TES tank becomes empty. The chiller power

profile is initialized as being zero at all times.

2. The time step before the TES tank is expected to be empty and the last time step when the TES level was full is recorded. Between these two points in time, the chiller plant must be activated to prevent the TES tank from becoming empty and unable to meet the cooling demand. Therefore, this creates a window where the cost of providing a certain increment of chilling can be evaluated.
3. In this window, the cost (according to the specified cost function) of using the chiller plant to provide a fixed increment of cooling is evaluated at each time step. The increment of cooling is specified by the user as a fraction of the cooling capacity of the chiller plant. The time step at which the increment of cooling can be provided at lowest cost is selected, and the chiller power is increased at that particular time step. The TES level is constrained such that the capacity of the TES tank cannot be exceeded, that is, time steps where adding one increment of cooling would cause an overflow of the TES tank are automatically assigned an extremely high cost function value and are therefore disregarded.
4. The chiller power profile is updated, and the process described in steps 1-3 are repeated, with the new initial time step starting immediately after the last time step when the TES tank was full as evaluated in the previous process iteration.
5. Steps 1-4 are repeated until the end of the year is reached, producing an updated chiller power profile for the entire year. The updated chiller power profile for the campus is added to the decoupled electric load for the campus to produce a new campus load profile.

5 HiGRID

The HiGRID tool was developed to resolve interaction between different types of generation (e.g., gas turbines, combined cycle plants, renewable generators) and supporting equipment in an effort to evaluate the cost and benefit of installing renewable generation capacity. The time resolution is hourly and the analysis area can range in size from a campus to the entire state of California depending on the input data. Applied to the state of California, it has the capability to integrate conventional generators including coal, nuclear, natural gas and hydroelectric with an array of both local and regional renewable generation. However, for the purposes of this report it has been used only for application to the UCI Microgrid. Given this, only those resources associated with the UCI Microgrid (as well as those future resources investigated) will have their integration into the HiGRID framework described here. For further description, see (Eichman et al., 2013; Samuelsen et al., 2013).

A very important aspect of the HiGRID tool is that each resource data signal is temporally coincident, because many of the phenomena that contribute to intermittencies of renewable generation like wind speed, temperature, cloud cover, and humidity also affect the operation of other generators as well. Another important aspect is how the various resources are categorized and called upon as shown in the flow diagram of the HiGRID tool inFigure 31.

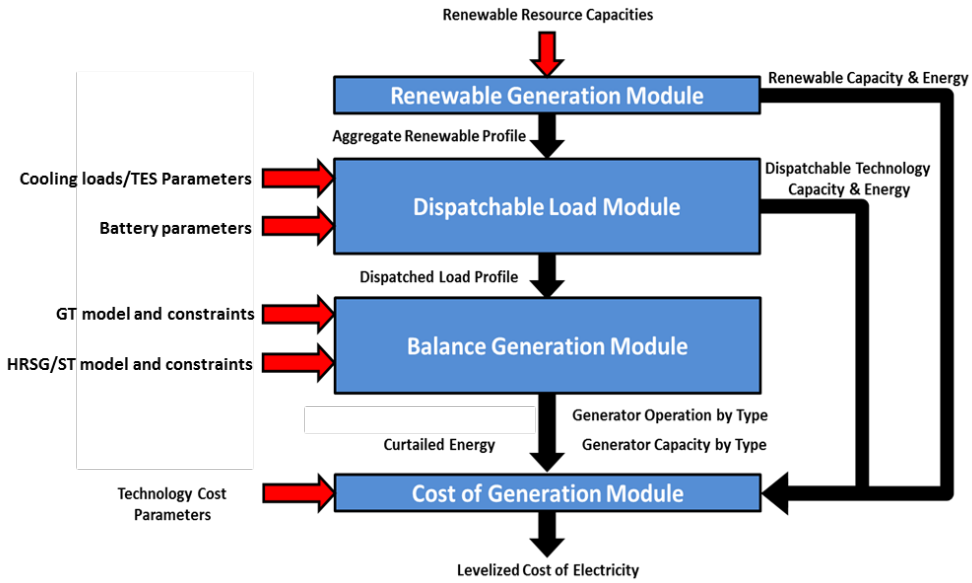

Figure 31: HiGRID tool flowchart

Specifically, the HiGRID tool makes use of 4 distinct modules. These modules are described in brief as follows, with more detailed descriptions in (Eichman et al., 2013; Samuelsen et al., 2013).

5.1 Renewable Generation Module

This module takes the capacity of different renewable resources as an input, and uses models of each type to determine the time-resolved profile of power generation and power delivered to load for each resource type. In the case of this study, only solar resources located on the UCI Microgrid are considered (fixed-tilt PV and dual-axis CPV). The costs associated with utilization of these resource types is also calculated and factored into the cost of generation module. The generation profile of the combined renewable resource mix is composed and fed into the dispatchable load module.

5.2 Dispatchable Load Module

The dispatchable load module takes the time resolved electric demand profile and aggregate renewable generation profile as inputs to compose the net load profile. This module dispatches complementary technologies and loads in response to the behavior of the net load profile or the behavior of balance generators through an iterative process, within the operating constraints of each technology. This is where the VFB energy storage model is used for this study. After all selected technologies are dispatched, the adjusted net load profile which balancing generators must meet is produced and fed into the balance generation module.

5.3 Balance Generation Module

The balance generation module determines the dispatch of GT, ST, and electric utility import that is required to meet the adjusted net load profile. The performance capabilities of the GT and ST as well as their interaction through the HRSG are taken into account through the use of the dynamic models discussed in the previous sections. The operation of the ST and GT determined in this module can also be re-fed back into the dispatchable load module to allow technologies to respond specifically to certain

aspects of the ST and GT in an iterative process. However, this capability was not used in this study.

5.4 Cost of Generation Module

Once all of the installed capacities, operational characteristics and resource consumption of all of the different types of technologies considered have been computed, these measures are fed as inputs into the cost of generation module. This module is based in part on the California Energy Commission (CEC) model for determining the Levelized Cost of Electricity (LCOE) and has been developed further to include a wide range of technologies and unique operation methods. The cost of each technology considered in this study is shown in Table 10.

Table 10: Cost parameters for UCI technologies considered in this study (VFB instant cost in $/kWh = 775)

	Rooftop fixed-tilt PV	2-Axis Tracking CPV	Flow Battery (Va Redox)	Small GT (13.5MW)	Small ST (6.0MW)	Electric Chiller	Thermal Energy Storage (TES)	Electricity Imports
Gross Capacity	0.01	25	10	13.5	6	200	10	100
Annual Capacity Factor	0.2	0.32	0.1	0.8	0.45	0.25	0.75	0.65
Instant Cost ($/kW)	6600	4650	3100	1200	1000	400	600	0
FOM ($/kW-yr)	25	55	32	25	30	10	1.75	0
VOM ($/MWh)	0	0	0	5	7.5	48	1	0
HR (MMBtu/MWh)	0	0	0	12	0	0	0	0
HR Degradation	0	0	0	1e-3	1e-3	0	0	0
Capacity Degradation	5e-3	0.005	0	1e-3	1e-3	5e-3	5e-3	0
Debt Term (Yrs)	20	15	5	12	12	20	20	0
Economic Life (Yrs)	25	20	10	20	20	20	30	20
Federal Tax Life (Yrs)	5	5	10	15	15	20	20	0
State Tax Life (Yrs)	20	20	10	15	15	20	30	0
Ad Valorem Tax Rate	0	0	0.011	0.011	0.011	0.011	0.011	0
Annual Starts	0	0	0	150	100	0	0	0
Start-Up Fuel (MMBtu/MW)	0	0	0	2.8	0	0	0	0
Plant Losses	0	0.09	0	0.034	0.034	0	0	0
TX Losses	0	0.05	0.05	0	0	0	0	0
Transformer Losses	0	5e-3	5e-3	0	0	0	0	5e-3

6 UCI Community Modeling Results

This section describes the results of various scenario investigations using the HiGRID tool. In particular, deployment of dual-axis CPV systems at the UCI campus is investigated. The deployments range from the current installation (893 kW fixed-tilt PV and 113kW dual-axis CPV) up to 70MW installations of dual-axis CPV. This rollout of dual-axis CPV systems will be compared to a similar rollout of fixed-tilt PV. The HiGRID tool is also used to evaluate how cooling loads can be dispatched when thermal energy storage is available in order to enhance dual-axis CPV integration to the UCI campus Microgrid. Battery energy storage and its effect on dual-axis CPV integration will also be investigated. This section also includes some investigation into the utilization of the gas turbine and steam turbine as ancillary services operating in the CAISO market.

6.1 dual-axis CPV and fixed-tilt PV Comparison

Simulations with the HiGRID tool were performed for deployments of dual-axis CPV and fixed-tilt PV systems up to 70 MW. Installations of this capacity are not possible at the UCI campus for either dual-axis CPV or fixed-tilt PV systems. The estimated maximum installation capacity for dual-axis CPV and fixed-tilt PV systems at the UCI campus is 22 and 15 MW, respectively (See (Samuelsen et al., 2013)). However, 70 MW was chosen in order to take the analysis to an extreme case to allow further comparison. In both deployments (i.e., dual-axis CPV and fixed-tilt PV), the TES and cooling load dispatch methodology was the same (utility biased optimization as described in Section 4.3.1). The gas turbine in both deployments is dispatched to operate at maximum power while also maintaining the minimum import requirement specified in the utility interconnect agreement. The minimum turn down of the gas turbine is 8MW. The minimum import requirement is 1 MW but is typically kept at 2MW to ensure the gas turbine does not trip off as a result of going below the minimum import of 1MW. The steam turbine is dispatched if there is additional heat available from the HRSG once the heating load is satisfied. The duct burner could also be fired to provide additional heat for the steam turbine if needed, however, this rarely occurs and is not modeled here. Figure 32 shows the time series plots for one year of operation under different fixed-tilt PV deployment scenarios. The important aspects are that for low deployments of fixed-tilt PV there is no curtailment; the gas turbine operates at higher capacity factor; the steam turbine operates at higher capacity factor; more utility import is needed; and much lower levels of renewable power are produced. The basic message is that without the ability to export to the utility much of the renewable power generated by on-site renewable resources must be curtailed. However, at the current campus renewable deployment, there is still opportunity to reduce the utility import with renewable power. Therefore, it is important that the campus continue to deploy renewable resources to reduce carbon and criteria pollutant emissions by reducing utility imports.

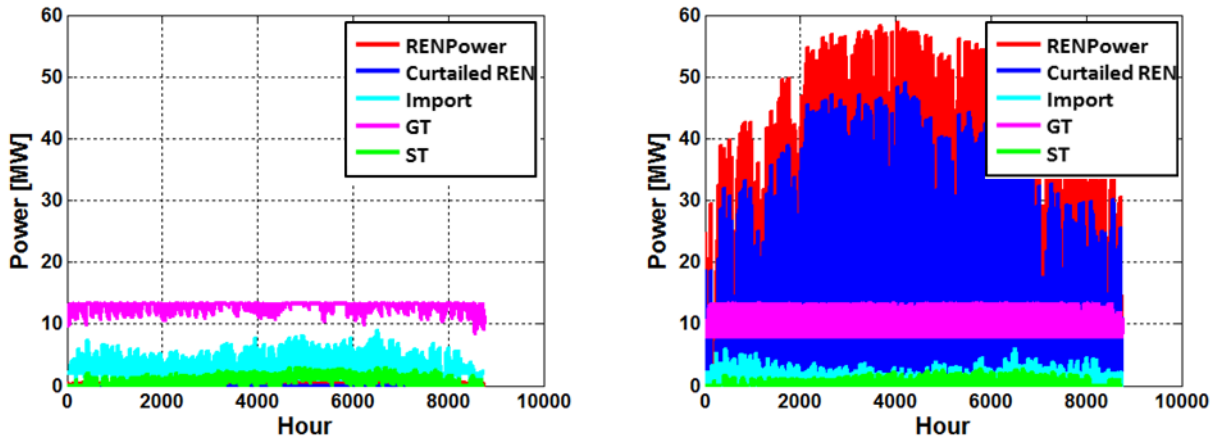

a) b)

Figure 32: Time series plots of various campus resources for a) current renewable deployment (893kW fixed-tilt PV and 113kW dual-axis CPV) and b) 70MW fixed-tilt PV deployment with 113kW dual-axis CPV

The point at which the renewable energy contribution to the overall campus energy needs begins to decrease exponentially as new renewable capacity is installed is shown in Figure 33. For the deployment of both dual-axis CPV and fixed-tilt PV systems, there is a limit at which each additional installed MW of capacity results in diminished energy production due to curtailment required by the need to balance load and generation given the utility import restriction. The solution might be lifting the utility import restriction and allowing export. However, this would introduce large dynamics onto the utility system, and if many other communities also did this or as the fraction of annual energy met by renewables on the utility grid increased, curtailment would still be required in order to balance load and generation on the entire grid (See (Eichman et al., 2013; Samuelsen et al., 2013)for more information). Therefore, other solutions must be implemented in order to achieve higher fractions of annual energy met by renewables with the least installed capacity (i.e., least cost). These will be investigated in subsequent sections, but include cooling load dispatch with thermal energy storage and electric energy storage.

Figure 33 also allows for comparison between the dual-axis CPV and fixed-tilt PV systems, which is this section's focus. The dual-axis CPV system allows for slightly higher fractions of annual energy met by renewables for the same installed capacity of fixed-tilt PV systems up until an installed capacity of 27 MW. Given that on-campus space constrained maximum installation capacity for fixed-tilt PV is 15 MW (22 MW for dual-axis CPV), dual-axis CPV systems are slightly superior to fixed-tilt PV systems in their capability to achieve higher fractions of annual energy met by renewables for similar installed capacities over the practical range of interest for the UC Irvine campus. However, if UCI acquired more land or purchased more fixed-tilt PV/dual-axis CPV power, then beyond installed capacities of 22 MW, fixed-tilt PV systems begin to become superior in the ability to increase fractions of annual energy met by renewables for additional installed capacity. dual-axis CPV systems are slightly superior in the lower fractions of annual energy met by renewables ranges because their tracking capability enables them to have higher capacity factors than fixed-tilt PV systems. However, at the higher fractions of annual energy met by renewabless, the dual-axis CPV systems capability for higher capacity factors begins to have less effect because the dual-axis CPV generation is more peak dominated than the fixed-tilt PV systems. For example, Figure 34 shows the time series plot of fixed-tilt PV and dual-axis CPV at the same

30 MW installation capacity. The dual-axis CPV system is capable of higher peaks in generation, but is incapable of generating during times of diffuse radiation (e.g., cloud cover) whereas the fixed-tilt PV systems are. Although the fixed-tilt PV systems cannot typically generate as much in direct sunlight, their ability to generate during times of diffuse radiation allow a more distributed overall generation profile that is more effective at avoiding curtailment than generation with high peaks for small periods of time. This can also be seen when comparing wind and solar as in (Eichman et al., 2013; Samuelsen et al., 2013).

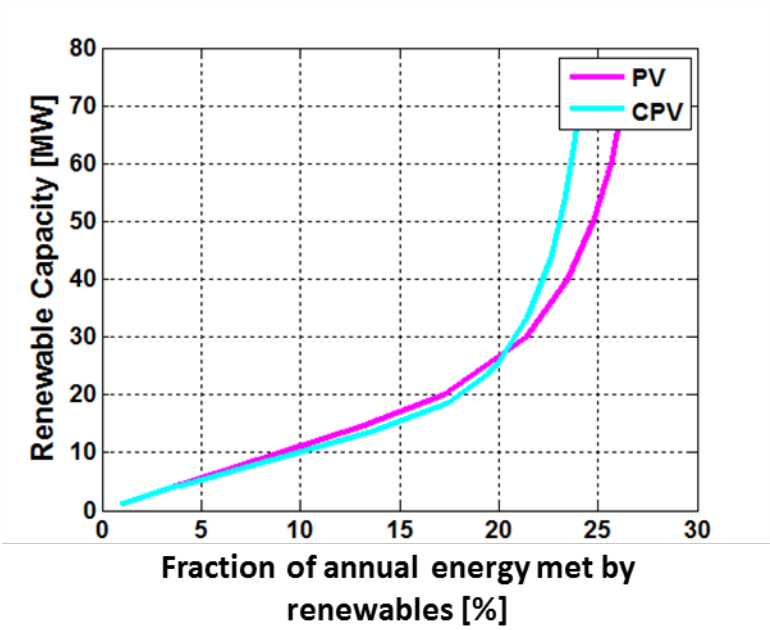

Figure 33: Renewable installed capacity versus the fraction of annual energy met by renewables for the dual-axis CPV and fixed-tilt PV deployment scenarios

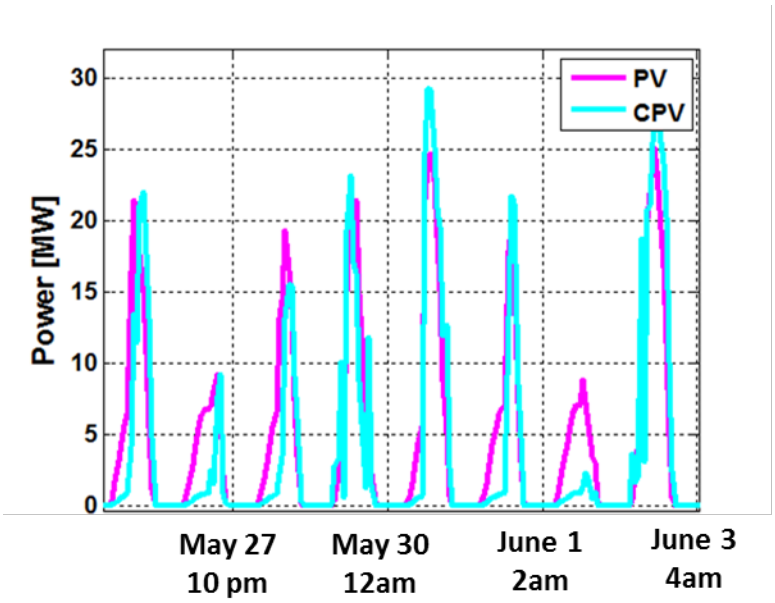

Figure 34: Time series plot of 30MW fixed-tilt PV and dual-axis CPV system installed capacities

Curtailment of renewables is not the only issue that occurs as fractions of annual energy met by renewables increase as shown in Figure 35 and Figure 36. The gas turbine and steam turbine capacity factors are reduced as fractions of annual energy met by renewables increases. These reduced capacity factors indicate that these pieces of equipment are being turned down in order to allow for the increased renewables. When the GT and ST were being planned for financially, it was likely assumed that these systems would have high capacity factors meaning that reduced capacity factors will affect the economics of the GT and ST (as well as the HRSG, see Figure 37). The installation of dual-axis CPV systems allows for a very slight increase in GT capacity factor over fixed-tilt PV systems at higher fractions of annual energy met by renewables, however, fixed-tilt PV systems allow for a greater increase in ST capacity factor over the dual-axis CPV system at higher fractions of annual energy met by renewables. It is interesting to note that the GT and ST capacity factors are nearly the same until a divergence point, and this divergence point occurs earlier for the ST capacity factor than the GT capacity factor. This occurs for reasons similar to those given above for fixed-tilt PV systems allowing less curtailment at higher fractions of annual energy met by renewables: fixed-tilt PV systems have less peaky operation and are more distributed allowing the steam turbine to be used more often as opposed to being turned off. The reason this doesn't occur in the case of the GT is the gas turbine cannot be turned off or turned down lower than 8MW. Therefore, the operation of the gas turbine in the dual-axis CPV and fixed-tilt PV deployments is more similar than the ST operation. The dual-axis CPV system allows a very slight increase in GT capacity factor because it allows the GT to operate at higher power for longer whereas the fixed-tilt PV systems given its less peaky operations requires slightly lower power for slightly longer periods. However, the difference in GT capacity factor between the two deployment scenarios is so small it may be within the model's error.

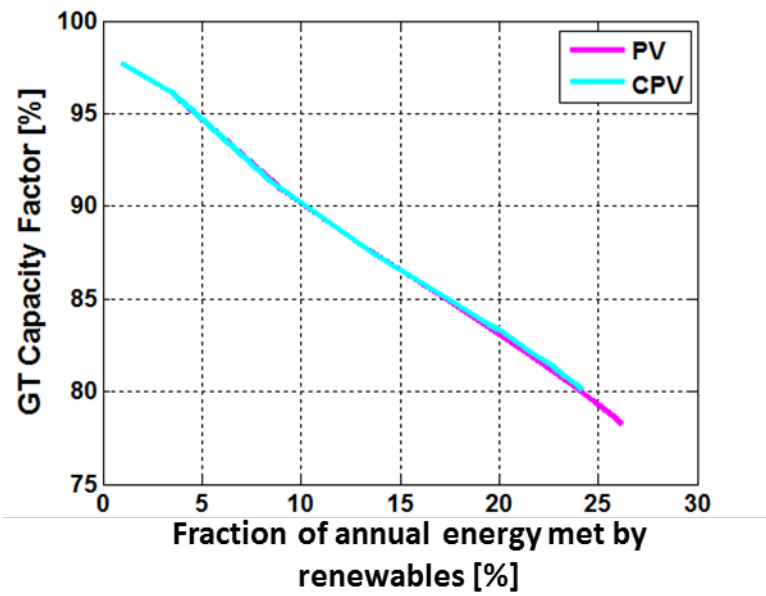

Figure 35: Gas turbine capacity factor versus fraction of annual energy met by renewables for fixed-tilt PV and dual-axis CPV system deployments

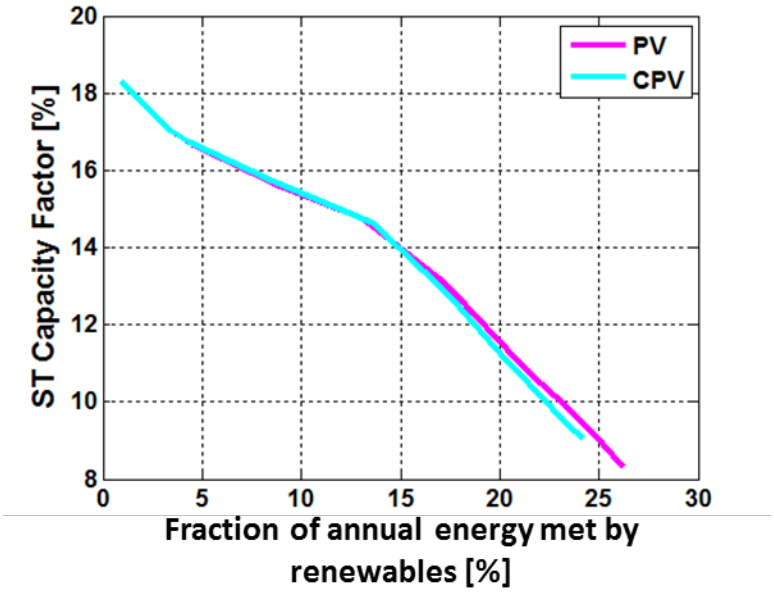

Figure 36: Steam turbine capacity factor versus fraction of annual energy met by renewables for fixed-tilt PV and dual-axis CPV system deployments

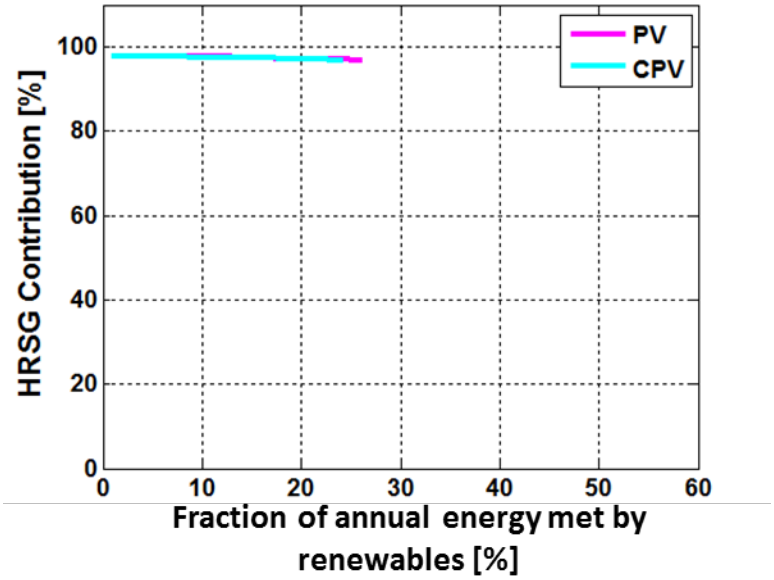

Figure 37: HRSG contribution to heat load versus fraction of annual energy met by renewables for fixed-tilt PV and dual-axis CPV system deployments

The percent increase in the levelized cost of electricity (LCOE) versus the fraction of annual energy met by renewables for the fixed-tilt PV and dual-axis CPV deployments is shown in Figure 38. The percent increase in LCOE exhibits trends similar to those in Figure 33. This results for the same reasons discussed previously: each additional installed MW of renewable capacity contributes less energy because of curtailment, which drives up the cost of electricity because each additional MW of delivered power

requires more installed capacity in addition to the fact that the conventional generators are also operating at more reduced capacity factors driving up their specific LCOE. Figure 38 also shows similar differences between the dual-axis CPV and fixed-tilt PV deployments as in Figure 33. This also occurs for reasons discussed above relating to the higher capacity factors but more peaky nature of the dual-axis CPV systems that result in dual-axis CPV systems having lower LCOE at low fractions of annual energy met by renewables where fixed-tilt PV systems have lower LCOE at higher fractions of annual energy met by renewables due to their ability to convert diffuse radiation. Although Figure 33 and Figure 38 are similar, the differences between the dual-axis CPV and fixed-tilt PV deployments are enhanced in Figure 38 compared to Figure 33. This occurs because the installed cost of dual-axis CPV ($4650/kW) is assumed to be less than that of fixed-tilt PV ($6600/kW). If the installed cost of dual-axis CPV were assumed closer to the cost of fixed-tilt PV then the LCOE gap between dual-axis CPV and fixed-tilt PV at the lower fractions of annual energy met by renewables would be reduced in Figure 38.

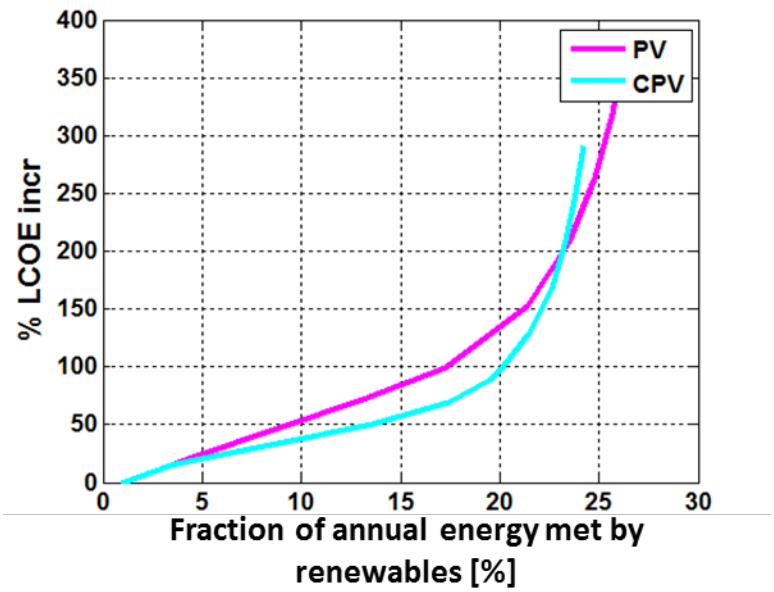

Figure 38: Percent increase in the levelized cost of electricity versus fraction of annual energy met by renewables for fixed-tilt PV and dual-axis CPV system deployments

6.2 Thermal Energy Storage and Chiller Dispatch to Enable Renewable Integration

This section describes simulations with the HiGRID tool to demonstrate the effectiveness of using thermal energy storage (TES) with appropriate dispatch of cooling loads in order to enable higher energy penetrations renewables. The dual-axis CPV deployment scenario (0.113MW to 70MW) investigated in the previous section (Section 6.1) will be evaluated for two cases of chiller dispatch and TES tank installation. The two cases are: 1) the UCI Microgrid with a TES tank installed and smart dispatch of the

chiller loads (i.e., cooling loads) and 2) without a TES tank installed and no smart dispatch of chiller loads.

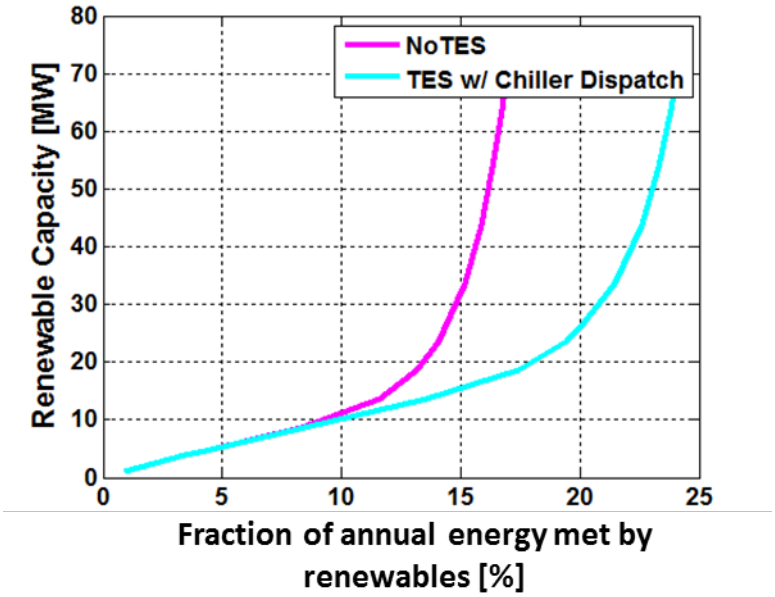

Figure 39: Installed dual-axis CPV capacity versus fraction of annual energy met by renewables for the UCI Microgrid without a TES tank installed and with a TES tank installed and cooling load dispatch

Figure 39 shows the installed renewable dual-axis CPV capacity versus the renewable dual-axis CPV energy penetration for the two cases of chiller dispatch. The first case (with no TES tank and no smart chiller dispatch) results in more curtailment than the second case (with TES tank installed and smart chiller dispatch) showing that the TES tank can be utilized to better integrate renewables (i.e., higher fractions of annual energy met by renewables for a given installed dual-axis CPV capacity). In fact, the installation of the TES tank and use of smart chiller dispatch does not only significantly increase the ability of the UCI Microgrid to integrate the installed dual-axis CPV, but also allows for increased capacity factors of the gas and steam turbines (Figure 40) and lower LCOE (Figure 41). The installation of the TES tank allows the UCI Microgrid to dispatch the cooling loads in such a way to minimize energy usage (because the chillers operate more efficiently at night due to more efficient heat rejection through the cooling towers) and reduce electric chiller operation during peak load periods.

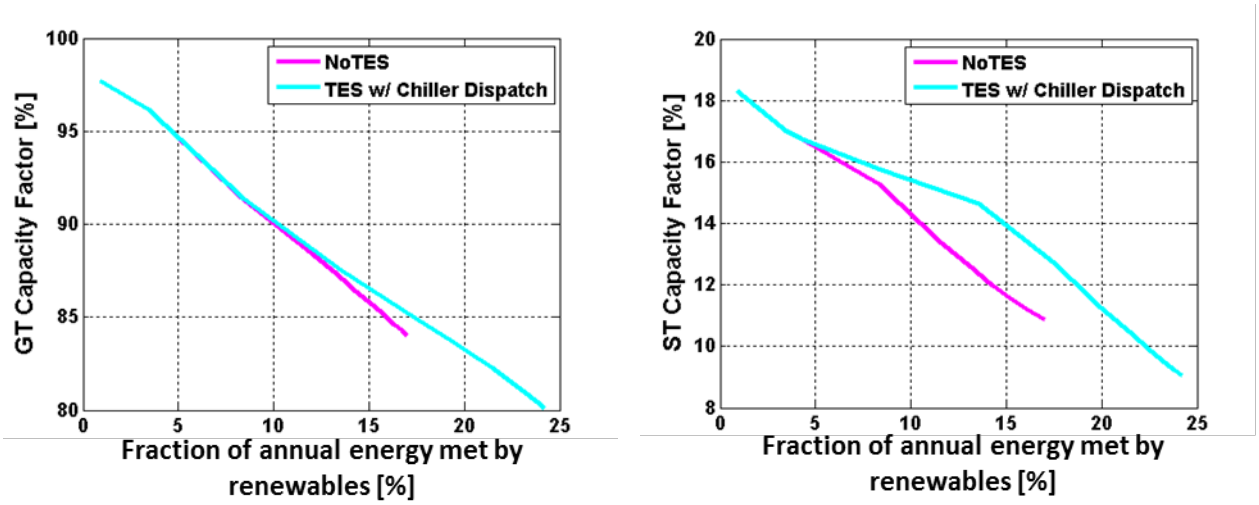

a) b)

Figure 40: Gas turbine a) and steam turbine b) capacity factor versus fraction of annual energy met by renewables for dual-axis CPV system deployments on the UCI Microgrid without a TES tank installed and with a TES tank installed and cooling load dispatch

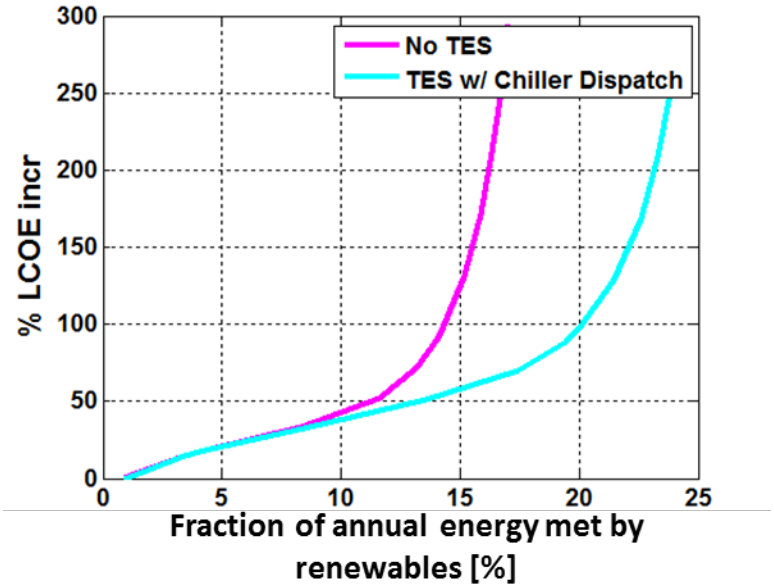

Figure 41: Levelized cost of electricity versus fraction of annual energy met by renewables for dual-axis CPV deployment on the UCI Microgrid without a TES tank installed and with a TES tank installed and cooling load dispatch

6.3 Battery Energy Storage

In this section, the effectiveness of battery energy storage on dual-axis CPV integration into the UCI Microgrid is investigated. The particular battery energy storage technology used in this investigation is Vanadium Redox Flow Battery. Pumped Hydroelectric Storage (PHS) and Compressed Air Energy Storage (CAES), which are the other two types included in the general energy storage model, are large scale,

geographically constrained systems. Therefore, it would not make sense to apply these technologies exclusively for a smaller scale system such as the UCI campus. The energy storage system is dispatched to smooth the balance profile as much as possible, responding to the effects of renewable power generation (see (Eichman et al., 2013; Samuelsen et al., 2013)). The specifications of the Vanadium Redox Flow battery used in this study are shown in Table 8.

The effects of electric energy storage in Figure 42 appear minimal at lower fractions of annual energy met by renewables; however, as the energy penetration increases the electric energy storage begins to reduce curtailment by allowing charging and discharging of renewable energy when demand is available, which is shown as reduced renewable capacity for a given fraction of annual energy met by renewables.

The effect of implementing energy storage on the UCI campus on the renewable capacity required to reach a given fraction of annual energy met by renewables is dependent on the following factors:

1. **The efficiency penalty associated with using the energy storage system**. When a unit of energy is stored and discharged, a portion of it is lost to inefficiencies of the system. Therefore, the amount available for discharge will be lower than the amount that was used to charge the system. To provide a given amount of energy towards serving the raw load demand, more generation is needed to overcome these inefficiencies. This essentially acts to increase the load demand by the amount consumed by these inefficiencies, and decreases the fraction of annual energy met by renewables for a given renewable energy contribution. It is important to note that only the fraction of energy that is shifted by the system actually passes through it and the efficiency penalty is only applied to this fraction and not the entire load demand.
2. **The smoothing of the balance profile allows renewable power that would otherwise be curtailed to contribute towards serving the load demand**. Energy storage can store excess renewable energy and discharge it during other periods, allowing this energy to contribute towards serving the load. This serves to increase the fraction of annual energy met by renewables for a given installed renewable capacity.

In this analysis, the energy storage system is used to smooth the balance profile. At low fraction of annual energy met by renewables levels when renewable curtailment is minimal or non-existent, the energy storage cases require more renewable capacity to reach a given fraction of annual energy met by renewables compared to the base case, but only by a very small amount. At these levels, the only factor present is the efficiency penalty. However, the increase in the load demand is very small compared to the energy of the load demand since only a small portion of the energy obtained is stored and discharged by the energy storage system. Therefore, the increase in required renewable capacity to reach a given fraction of annual energy met by renewables is very minimal.

At high fractions of annual energy met by renewables when curtailment is significant, the energy storage cases require less renewable capacity to reach a given fraction of annual energy met by renewables compared to the base case. To the extent possible, the energy storage system charges during periods of low balance levels which tend to correspond to periods of high renewable power generation. This allows

the campus to make use of otherwise curtailed energy. The system then discharges this energy during periods of high balance levels, which correspond to periods of low renewable power generation. The increase in the amount of renewable energy that is able to serve the load demand overpowers the increase in the load demand due to the efficiency penalty of the battery storage at high fractions of annual energy met by renewables.

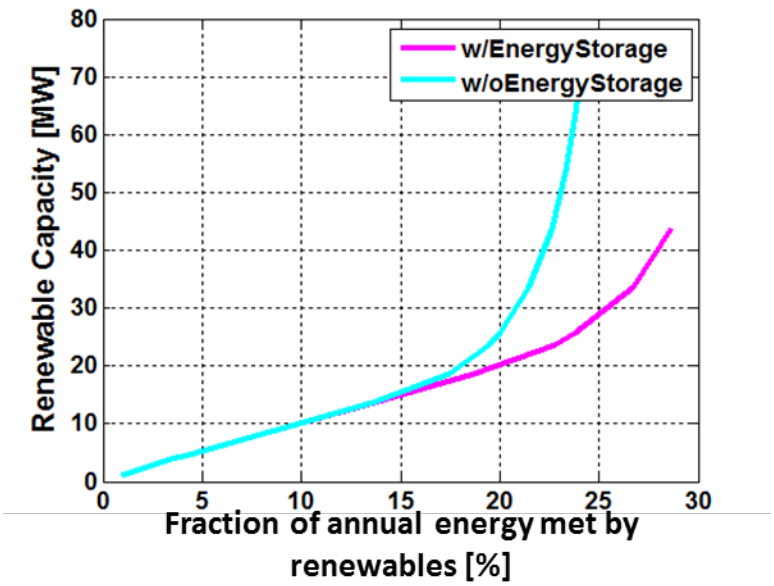

Figure 42: Installed dual-axis CPV capacity versus fraction of annual energy met by renewables for the UCI Microgrid with battery energy storage and without battery energy storage

The battery energy storage also allows increased GT and ST capacity factors by allowing the renewable energy generated at times of low demand to charge the battery rather than turn down the GT and ST (Figure 43). This effect diminishes as the fraction of annual energy met by renewables increases because the battery becomes too small to absorb all the excess renewable power at the higher fractions of annual energy met by renewables. This can be seen in Figure 43 by the smaller difference between the cases with and without energy storage at the higher fractions of annual energy met by renewables. It also occurs at lower fractions of annual energy met by renewables for the ST than the GT as would be expected since the ST is turned off prior to reduction in GT output as part of the dispatch strategy employed by the campus.

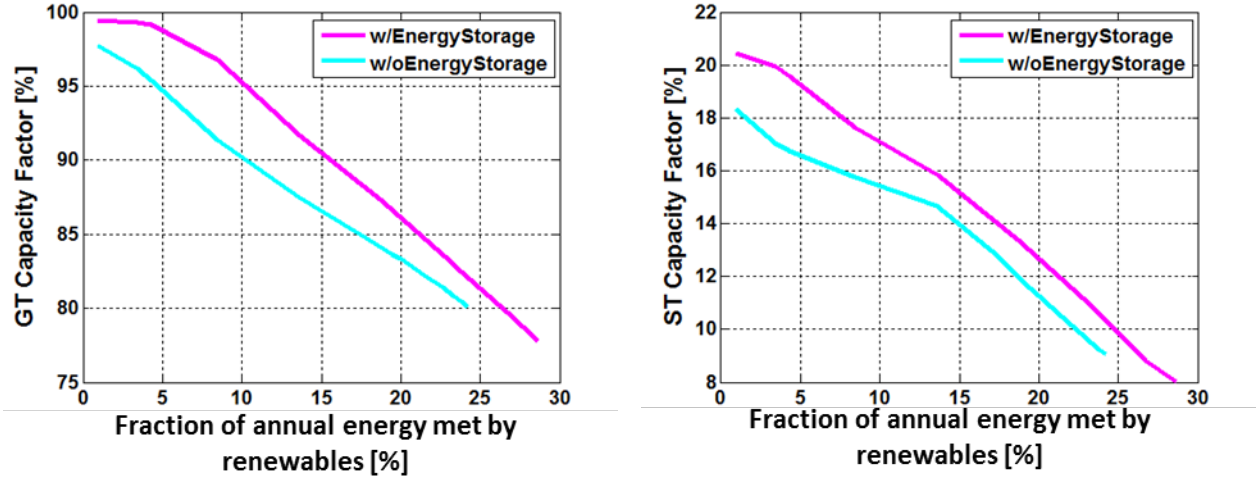

a) b)

Figure 43: Gas turbine a) and steam turbine b) capacity factor versus fraction of annual energy met by renewables for dual-axis CPV system deployments on the UCI Microgrid with battery energy storage and without battery energy storage

It is interesting to observe the battery storage system's effect on the levelized cost of electricity in Figure 44. At lower fractions of annual energy met by renewables, the battery storage system results in higher costs while at higher fractions of annual energy met by renewables results in lower costs than the case without battery storage. The battery storage system is underutilized at the lower fractions of annual energy met by renewables, which results in the higher LCOE there. However, once curtailment begins to be an issue, the battery storage system is utilized more and hence allows higher fractions of annual energy met by renewables resulting in lower LCOE because more renewable energy can be used rather than curtailed (but at the cost of the added battery storage system).

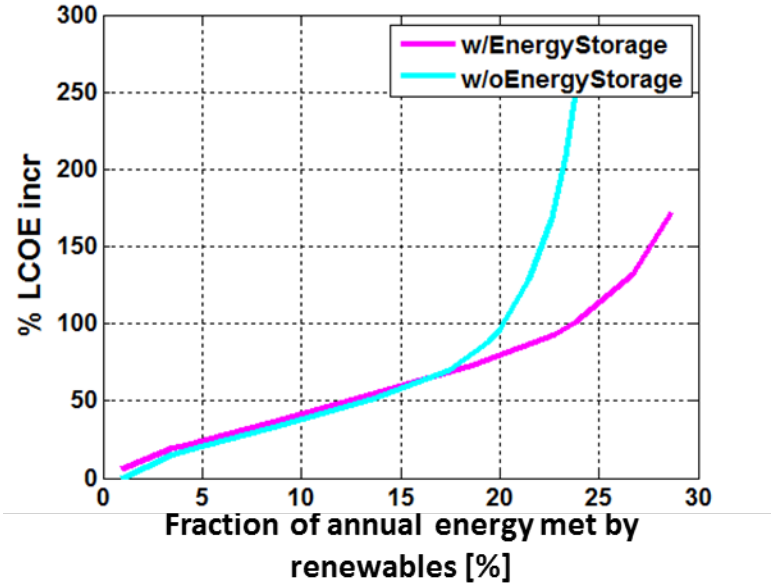

Figure 44: Levelized cost of electricity versus fraction of annual energy met by renewables for dual-axis CPV deployment on the UCI Microgrid with battery energy storage and without battery energy storage

6.4 Gas Turbine and Steam Turbine as Ancillary Services

In the previous sections, it was shown that as more dual-axis CPV or fixed-tilt PV systems are installed on the UCI Microgrid the gas and steam turbines must be turned down in order to accommodate the increase in on-site renewable generation while also satisfying import/export requirements. It has also been shown in (Eichman et al., 2013; Samuelsen et al., 2013) that the same issue occurs on the California grid as fractions of annual energy met by renewables increases. It is expected that regulations (AB 1613, Rule 21, etc.) and technologies for relieving issues associated with utility export will evolve in order to allow microgrids to assist the utility grid in managing intermittent renewables. It is expected that this will eventually enable the UCI Microgrid to participate in the CAISO market. This section examines several possibilities in which the UCI Microgrid uses the GT and ST to provide ancillary services.

6.4.1 Spinning Reserve Investigations

Operating reserves are capacity retained by generators that can be converted to generation in a short time to respond to contingencies/emergencies on the grid (e.g., loss of a generation or transmission line). Under the CAISO and FERC definitions, operating reserves are spinning and non-spinning resources that must respond within 10 minutes with spinning reserves meaning operating and synchronized while non-spinning reserves must be started and synchronized. Both types require fast ramp rate generation thus heavily favor gas-fired power plants.

During periods of low net load on the campus due to high renewable generation and low demand, the UCI Microgrid could provide spinning reserve using the gas turbine. Though depending on the size, a typical gas turbine has fast ramp-up capability from high part-load to full load (70% to 100%) that can respond within the 10 minute requirement. Thus, it is hypothesized that the gas turbine has the dispatchability to operate as spinning reserve. Such gas turbine operation should not affect the performance of the HRSG due to the narrow range of part-load operation of gas turbine.

Two simple strategies for spinning reserve operation are investigated in this section:

1. Full time spinning reserve – this strategy makes available a constant GT or ST capacity for spinning reserve over the entire year
2. Selective-bidding spinning reserve – this strategy makes available GT or ST capacity only when certain prices are seen in the CAISO market

6.4.1.1 Full Time Spinning Reserve

The UCI Central Plant operation data during 2010 were used in this analysis. A normal operating day is shown Figure 45. The gas turbine output is varying over the course of the day to satisfy the diurnal needs of the campus while also maintaining the utility import requirement. The steam turbine output varies depending on the steam available the campus heating loads are served. Actual operating data for 2010 are used in order to determine how much actual self-generation is provided by the GT or ST when that capacity is otherwise used for spinning reserve, and this also then allows the calculation of increased utility imports. This is shown in Figure 45. The steam turbine derate that results from GT turn

down for spinning reserve operation must also be calculated and is shown in Figure 45. Any shortage of steam required for meeting district heating requirement is provided by the duct burner, which is simulated as a boiler with 100% thermal efficiency. In actual systems, supplemental fired-duct burner has efficiencies close to 100% because the air is already at combustion-ready temperature and fuel energy goes directly into heat. The costs associated with these operational changes are assessed using natural gas and electric utility rate structure models. For the electric utility rate structure, TOU8-B-S-DL is used (see (Do, 2013)), and for the natural gas rate, a constant rate of $5/MMBtu is used.

The spinning reserve operation strategy is exemplified by the simulated day of August 23, 2010 as shown in Figure 45. The gas turbine is shown to operate at 9 MW and the dotted rectangle highlights the spinning reserve capacity. The highlighted green area depicts the gas turbine generation lost which results in the steam turbine turn-down to lower or zero output. The red area illustrates the required increase in import energy.

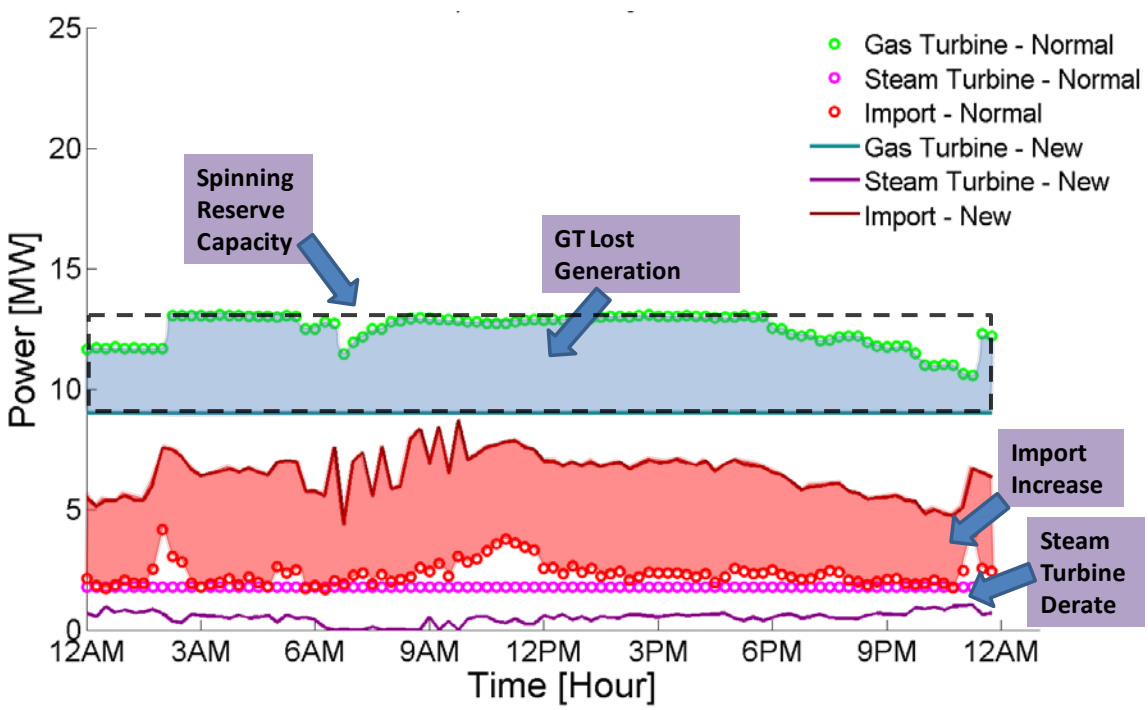

Figure 45: Typical operating day for UCI Central Plant as recorded on August 23, 2010

Figure 46 shows the simulated electric utility import costs for the full time spinning reserve operation strategy. Monthly rates under the spinning reserve strategy increase for every month as compared to normal operation in 2010 (Figure 47). The annual cost of the electric bill is now $4,712,528 while the total demand charges are $845,052. Total demand charges show little increase as compared to 2010 normal operation. This is mainly due to the fact that many maximum peaks for the month occurred during mid-peak or off-peak for winter season or during gas turbine downtime (unexpected trips) for the summer season. Gas turbine downtime provides no spinning reserve capacity, thus the import under spinning reserve simulation is the same as for normal operation.

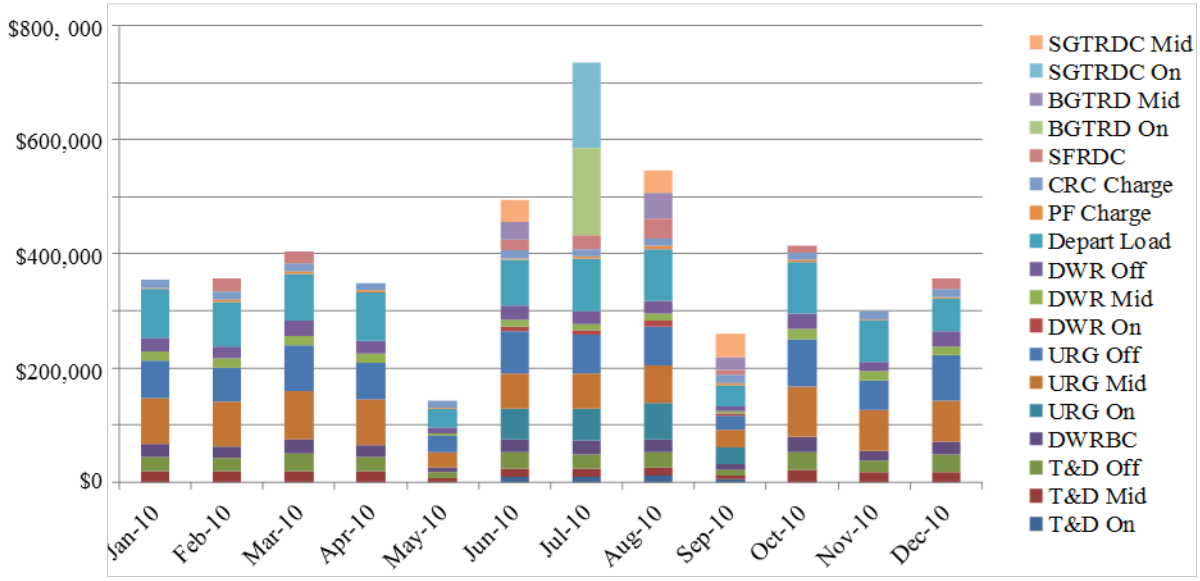

ACRONYMS

SGTRDC – Supplemental Generation Time Related Demand Charge
BGTRDC – Backup Generation Time Related Demand Charge
SFRDC – Supplemental Facility Related Demand Charge
CRC – Capacity Reservation Charge
PF – Power Factor
Depart Load – Departing Load
DWR – Department of Water Resources
URG – Utility Retained Generation
DWRBC – Dept. Water Resources Bond Charge
T&D – Transmission & Distribution
On – On Peak
Mid – Mid Peak
Off – Off Peak

Figure 46: Simulated monthly electricity costs and constituent charges for SCE TOU-8-B-S-DL rate for 2010 UCI Central Plant operation under full-time spinning reserve strategy

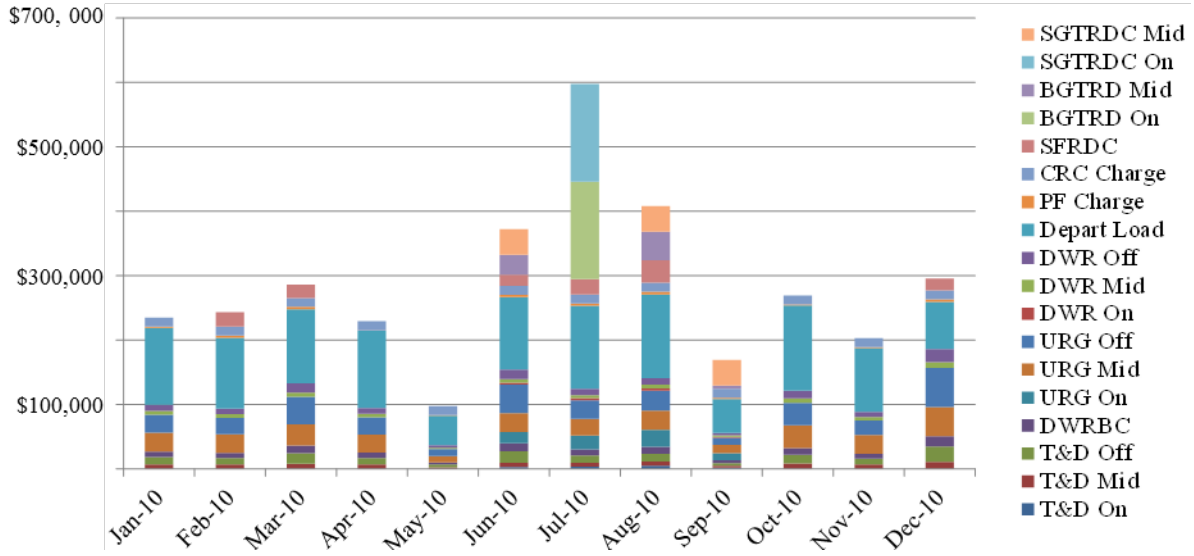

Figure 47: Simulated monthly electricity costs and constituent charges for SCE TOU-8-B-S-DL rate for 2010 UCI Central Plant operation

Table 11 showcases the total additional energy cost in operating the UCI Central Plant for spinning reserve. The difference in import should result in a $1.3 million cost increase in electrical utility bills. Accounting for the fuel savings as derived from Table 11, the total operational deficit would be slightly over $1 million. Factoring this cost into the increase in import energy to realize a cost of electricity (COE) increase of $42 per MWh.

Table 11: Cost of UCI Central Plant operation with full-time spinning reserve in 2010

Parameter	Value
SCE Cost Difference ($)	1,308,025
Fuel Savings from Part-Loading ($)	229,870
Operational Deficit ($)	1,078,155
Total Import Increase (MWh)	25,270
COE Increase ($/MWh)	42.67

The COE increase also represents the cost to break even if the UCI Microgrid is to operate with spinning reserve capacity full-time for the year. Under the current spinning reserve bid prices of CAISO, however, the average prices for 2010 is much lower than this cost. Figure 48 shows that the average market clearing price for spinning reserve in 2010 is $9.15/MW. The clearing prices for ancillary services are posted hourly on CAISO Oasis server for both Day-Ahead (DA) Market and Hour-Ahead Market.

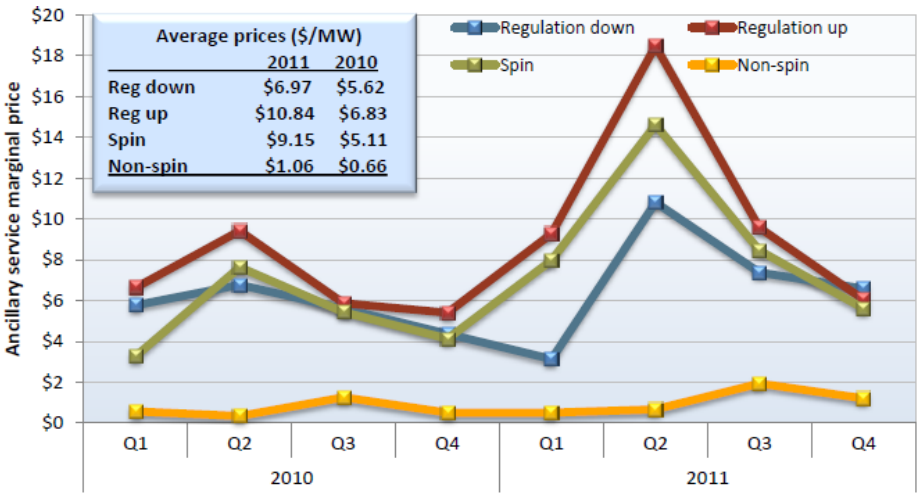

Figure 48: Quarterly average clearing prices for ancillary services in Day-Ahead Market of CAISO for 2010 and 2011 (Excerpt from (CAISO, 2011))

To further evaluate the economic benefits of providing spinning reserve capacity, CAISO day-ahead market clearing prices were used to determine the potential earnings. Figure 49 shows hourly clearing prices in January 2010 for spinning reserve in the general zone under CAISO authority. These are day-ahead values, which are available publically at CAISO Oasis server. Unfortunately, hour-ahead data were

missing or not available at this access point despite CAISO online documents stating otherwise. The prices in January show that for this month the expected contingencies are low, thus prices were at relatively low values.

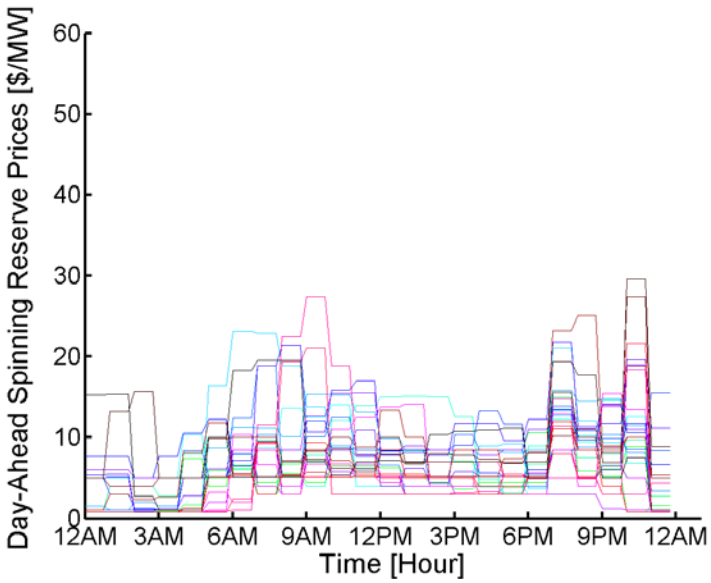

Figure 49: Hourly clearing prices for spinning reserve in Day-Ahead Market for January 2010

Annually, shortage of ancillary services occurs in spring largely due to the decline in the contribution of hydroelectric sources to ancillary services. During this season, hydroelectric units are used to provide generation instead of reserves due to very high hydro conditions. Since these units bid into the ancillary service market at relatively low costs, their unavailability in the spring causes high prices in April and May as shown respectively in Figure 50 and Figure 51. Reserves from gas-fired power plants are procured instead. However, most of these plants are non-spinning reserves according to CAISO [76] thus yielding opportunities to bid into the spinning reserve market.

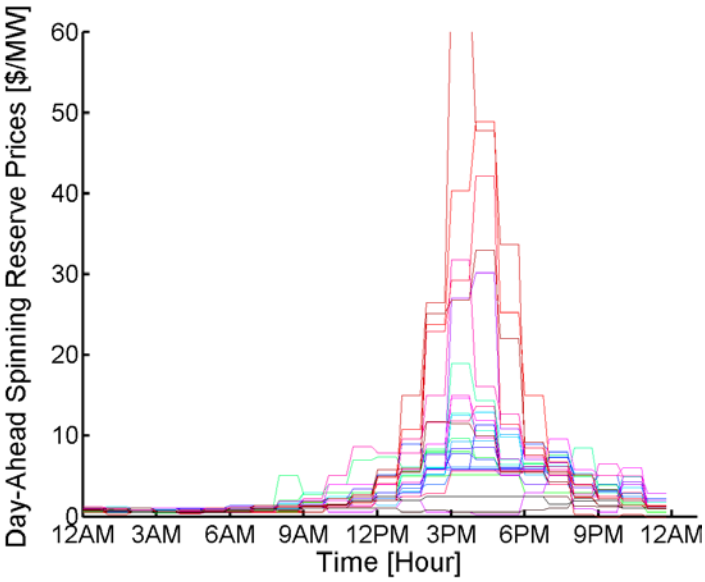

Figure 50: Hourly clearing prices for spinning reserve in Day-Ahead Market for April 2010

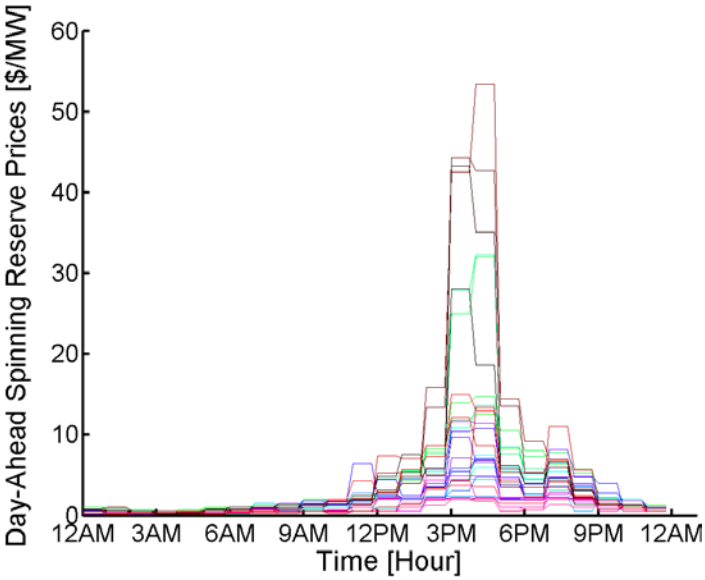

Figure 51: Hourly clearing prices for spinning reserve in Day-Ahead Market for May 2010

6.4.1.2 Selective-Bidding Spinning Reserve

Another spinning reserve operation strategy investigated was selective-bidding where the UCI Microgrid would bid GT or ST capacity competitively into the market when bidding prices were high. By selectively bidding into the market at certain periods when ancillary services are more valuable, the UCI Microgrid can avoid excessive electric import costs. Based on historic clearing prices for spinning reserves in the DA market and relying on the key assumption that the GT/ST can bid competitively (i.e. win 100% the bids) at these prices, spinning reserve earnings can be determined.

Several price levels were arbitrarily selected to be the point at which GT/ST capacity would be sold into the market for spinning reserve in order to investigate the sensitivity. These price levels are: $10, $20, and $30 per MW.

Table 12 tabulates the simulated results comparing the costs and benefits of operating the UCI Central Plant under different scenarios of spinning reserves. The full-time spinning reserve column is the case described in the previous section. Adjacent columns present the cases where selective bidding of spinning reserve are done for prices equivalent to or exceeding $10, $20,and $30 per MW reserved capacity. The general trend is decreasing cost as the bidding becomes more selective at the high price of $30/MW.

The last column depicts a case where the steam turbine (ST) is also used to provide spinning reserve capacity for the full year. In operating the steam turbine at UCI Central Plant at minimum level (500 kW), the maximum reserve capacity available is 5 MW from the 5.5 MW-rated Dresser-Rand Steam Turbine engine. Additional natural gas costs required to provide sufficient supplemental firing of the HRSG to keep the steam turbine spinning at minimum power are determined. The difference in the fuel cost is reflected in the table when comparing full-time GT bidding at market price versus full-time GT and ST

bidding at market price. In providing the additional capacity of the ST as reserve, the total capacity reserved possible is 76,865 MW for 2010. Though ST power output is at minimal level, the engine is operated more frequently and must be synchronized with the grid to satisfy SR requirements. In such regard, the ST should help lower the peak electric demands required of the IOU import. Table 12 shows that a lower SCE cost increase of $1.1 million is charged (vs. 2010 SCE bills). The total profits are reduced from a -$1.147,686 to -$791,140, respectively, for the two cases full-time GT as spinning reserve and full-time GT and ST as spinning reserve. These results show that under current markets and ancillary service requirements (of 2010) operating the UCI Central Plant with spinning reserve is highly unprofitable.

Table 12: Cost benefit comparison between different modes of providing spinning reserves for the UCI Central Plant

Costs and Benefits	Full-Time GT @ Market Price	Selective-Bidding @ $10+	Selective-Bidding @ $20+	Selective-Bidding @ $30+	Full-Time GT+ST @ Market Price
NG Additional [Therms]	-460,710	-98,131	-21,282	-6,039	-21,440
Fuel Cost [$]	-242,199	-51,588	-11,188	-3,175	-11,271
Capacity Reserved [MW]	36,410	14,111	13,633	432	76,865
Import Increase [MWh]	25,269	1,854	436	110	21,973
Expenditures [$]	4,750,301	4,940,912	4,981,312	4,989,325	4,981,229
Elec Production [MW]	70,027	93,443	94,861	95,187	73,324
Parasitic Losses [MW]	-3,681	-3,681	-3,681	-3,681	-3,681
Net Elec Production [MW]	66,346	89,762	91,180	91,506	69,643
Unit Cost [$]	71.60	55.04	54.63	54.52	71.53
Spin Reserve Earnings [$]	160,339	40,665	14,431	4,240	312,642
SCE Cost Increase [$]	1,308,025	237,721	155,352	137,501	1,103,782
Total Profits [$]	-1,147,686	-197,056	-140,921	-133,261	-791,140

6.4.2 Regulation Investigations

Another opportunity for the GT and ST to participate as ancillary services in the CAISO market is as regulation. Regulation is reserved capacity provided to CAISO by a generating resource that is running and synchronized with the grid. CAISO controls the resource through their Automatic Generation Control (AGC) to balance the grid in real-time. Regulation is utilized in normal grid conditions, which is different than other contingency reserves such as spinning, non-spinning, and replacement reserves. Generators or resources operating as regulation are regarded as primary resources while contingency reserves are supplemental resources. For these reasons, regulation is more valuable and their market clearing prices reflect this.

Balancing authorities such as CAISO uses regulation to continuously balance generation and system load. In real time, balancing authorities dispatch signals to generators every 5 or 10 minutes (varies across different ISOs) based on forecasts of load and generation. Generators that respond to such load-following service are placed under Automated Dispatch System (ADS) systems (Makarov, Loutan, & de

Mello, 2009).

CAISO defines regulation service as a resource having the ability to increase or decrease energy output on a minute-by-minute basis to balance system fluctuations (CAISO, 2010). Generators that can respond to such dynamics are placed under automatic generation control (AGC) of CAISO. Figure 52 displays a typical daily system load profile showing a morning ramp up, morning peak, evening peak, and evening ramp down. The minute-by-minute fluctuations (inset) are caused not only by the random aggregated loads but also by non-dispatchable and must-take generation of intermittent renewables.

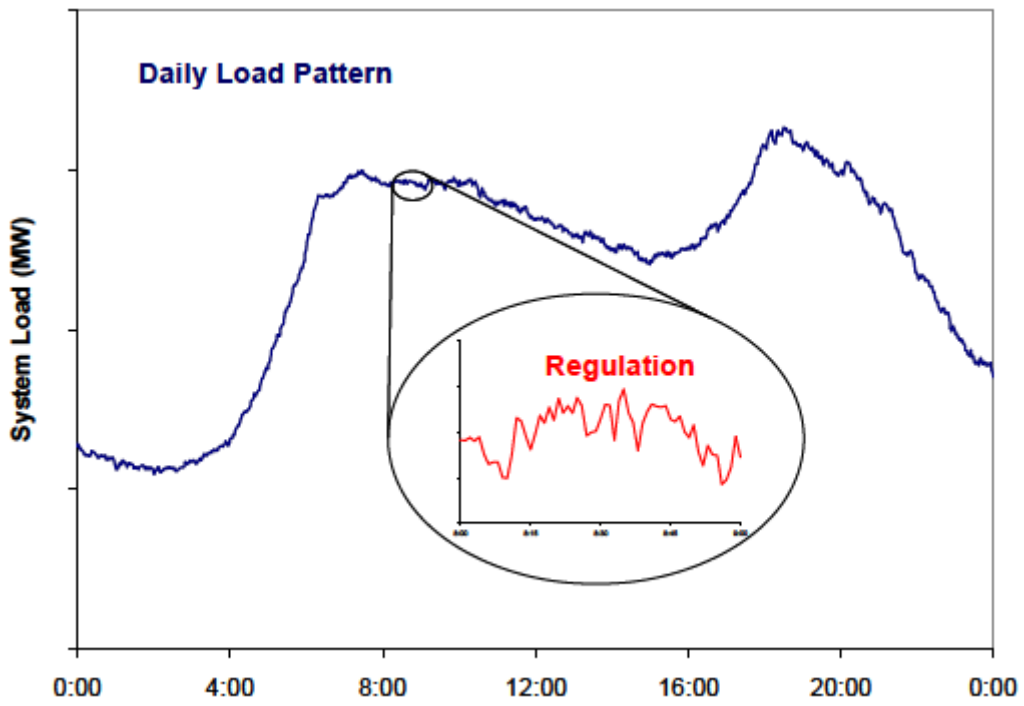

Figure 52: CAISO real-time regulation control that compensates for minute-to-minute fluctuations in total system load and non-dispatchable generation (Excerpt from (Kirby, 2007))

Under the terms and requirements of regulation service, generators must offer capacity that can be controlled by CAISO's AGC system to balance the power system(Kirby, 2007). Using the market prices for regulation reserves provided in Figure 48, the possible earnings from capacity payments were determined under 2010 and 2011 Day-Ahead Market clearing prices. Regulation Up and Down prices are accounting for two distinct upward and downward regulation markets due to the difference in fuel costs to ramp up a resource as compared to ramping down that same resource. For a flexible generator, ramping up and down can be easily performed and is twice as profitable to provide service to. Therefore, Regulation Up and Down prices were combined into an aggregated Regulation price for a controllable capacity range of the gas turbine (and steam turbine) in the analysis.

The generator under regulation reserve service is entitled to energy payments based on the generation produced during real-timed regulation control. Again, CAISO will pay for this capacity-converted energy under the real-timed locational marginal price (LMP). Assuming CAISO deploying regulation service for

the gas turbine, the total energy deployment can be calculated. The projected and simulated gas turbine dynamics for the April week of 2020 yielded an average of 2.17 MWh per hour for a total of 364.56 MWh. Apply the same analysis to the entire projected 2020 year, resulted in 13,152 MWh. Using the average hourly LMP of $36.41/MWh for 2010, an anticipated energy payment of $478,841.50 was obtained. Figure 53 provides the reserve capacity and energy payments for four ancillary service scenarios considered.

1. Full Time Spinning reserve operation with the gas turbine (Spin GT)
2. Full Time Spinning reserve operation with the gas turbine and steam turbine (Spin GT, Spin ST)
3. Regulation operation with the gas turbine (Reg. GT)
4. Regulation operation with the gas turbine and spinning reserve with the steam turbine (Spin GT, Spin ST)

The 2010 and 2011 Day-Ahead Market clearing prices of CAISO were consulted in the calculation of capacity and energy awards. The cost impact on utility electric bill was determined for the year 2010 using the economic model for the four scenarios.

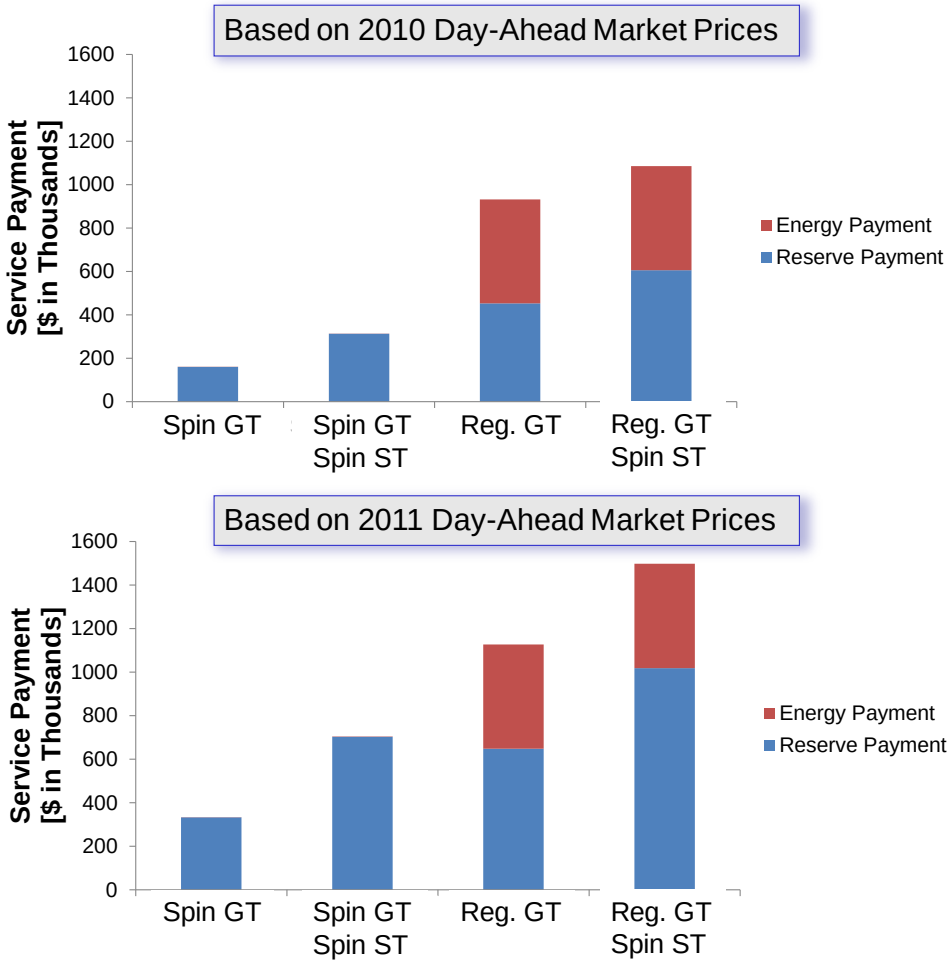

Figure 53: Ancillary service scenarios and payments based on Day-Ahead Market prices from 2010 and 2011

Table 13 shows the net profit for the four different scenarios. For gas turbine operation under regulation reserves, the additional energy payments would result in a net profit of -$375,879 and -$180,782, respectively, under 2010 and 2011 regulation reserve prices. The operation of the gas turbine as regulation is expected to be possible but the physical model described in previous sections will be used in the next section to explore the feasibility of operating the gas turbine as regulation. It is expected that the steam turbine engine might not be as responsive as that of the gas turbine and was not investigated as regulation.

The final case investigated was to operate the gas turbine with 4.5 MW as regulation and the steam turbine under 5 MW of spinning reserve. This mixed operation, with all the capacity and energy payments and utility cost considered, would almost break even under 2010 prices but yield a net profit of $393,309 under 2011.

Table 13: Net economic profits for UCI CCHP Plant to operate under different ancillary service scenarios as determined with Day-Ahead Market prices for 2010 and 2011

	Scenarios			
Year	Spin GT	Spin GT, Spin ST	Reg. GT	Reg. GT, Spin ST
2010	-1,147,686	-791,140	-375,878	-18,544
2011	-974,874	-400,472	-180,721	394,469

6.4.2.1 Feasibility of GT Operation under Automatic Generation Control for Regulation

In order to assess the feasibility of operating the GT as regulation, a highly dynamic load on the GT was estimated from future projections of net load in 2020 resulting from higher fractions of annual energy met by renewables of renewables. Figure 54 illustrates a projection of the demand for the Titan 130 of UCI Central Plant normalized from the projected net load for 2020. This variable load on the GT will be used to investigate the capability of the GT to supply regulation. The red dots are the hourly data points as derived from the raw data obtained from CAISO server. The connecting blue curve (from curve-fitting technique) can be viewed as the running-average results of minute-to-minute fluctuations. The controllable range for the gas turbine is the designated regulation reserved capacity of 4.5 MW (from 9 MW to 13.5 MW).

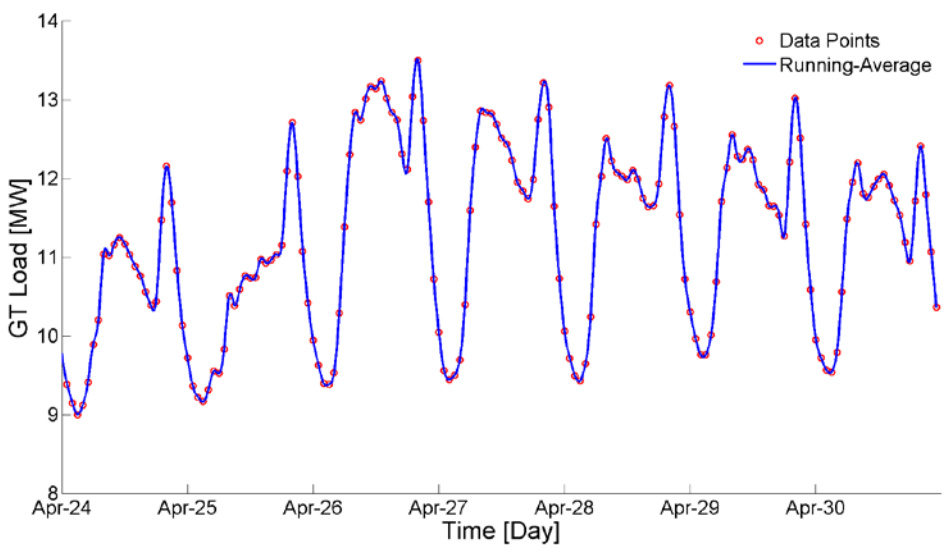

Figure 54: Projected load demand of the gas turbine of UCI Central Plant under regulation control for a future April week in 2020

Minute-by-minute fluctuations have not been obtained and may not be disclosed publicly by CAISO. Real-time dynamics of the load, however, might exhibit sinusoidal behavior due to the up-and-down nature of regulation ramps as seen in Figure 52. Thus, the gas turbine regulation load can be approximated with sinusoidal characteristics to represent minute-to-minute variations as shown in Figure 55. To obtain the real-timed dynamic curve, a sine wave with amplitude of 0.25 MW and time period of 1 minute was added to the running-average curve.

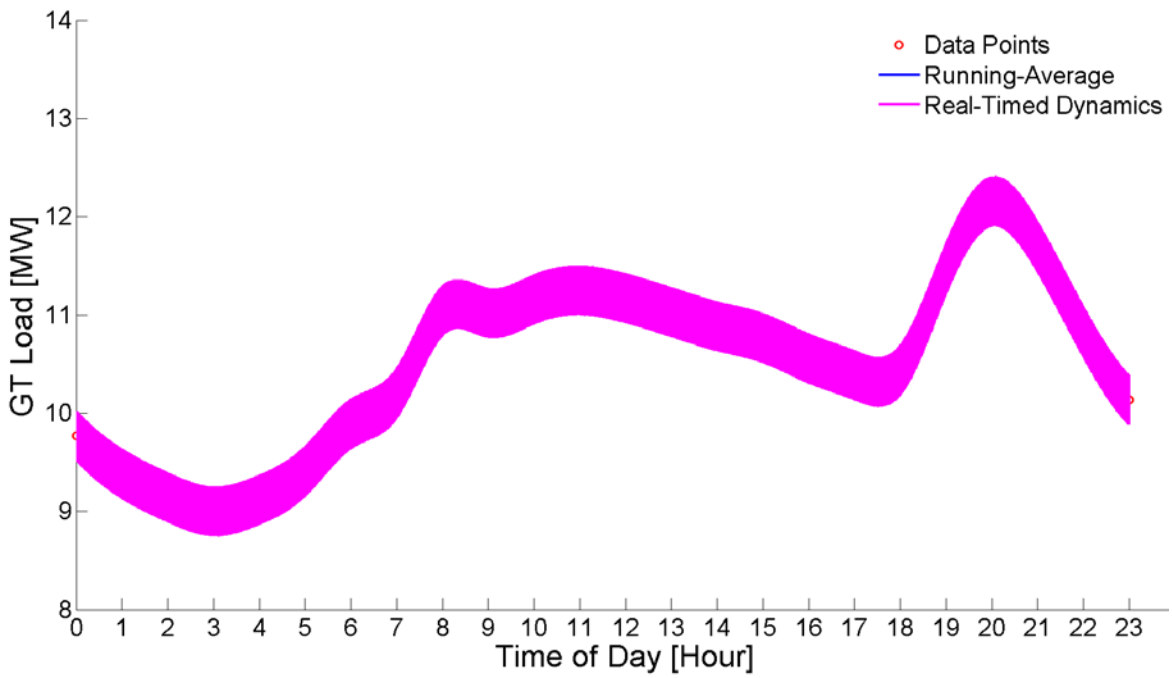

Figure 55: Sinusoidal characteristics are introduced to projected load demand of the gas turbine to approximate real-timed load dynamics for April 24, 2020

The displayed date in Figure 55 is a future April 24th in 2020 as projected from the same day from 2010. Zooming in on the hour between 8-9 AM on this futuristic date, Figure 56 shows the projected sinusoidal minute-to-minute variations in regulation service required by CAISO of the gas turbine. As can be noted from Figure 56, the ramp rate demanded of the engine reaches 0.5 MW per min. The gas turbine's capability to provide such ramping is highly plausible given the capability of the Mobile Version of the Titan 130 to reach full load within 6 minutes from cold-start according to Solar Turbines (i.e., 2.25 MW per min under cold-start) (Solar Turbines, 2010). Although this mobile version is specifically designed for peaking power applications, it is expected that the capabilities of the stationary version of Titan 130 should be somewhat comparable.

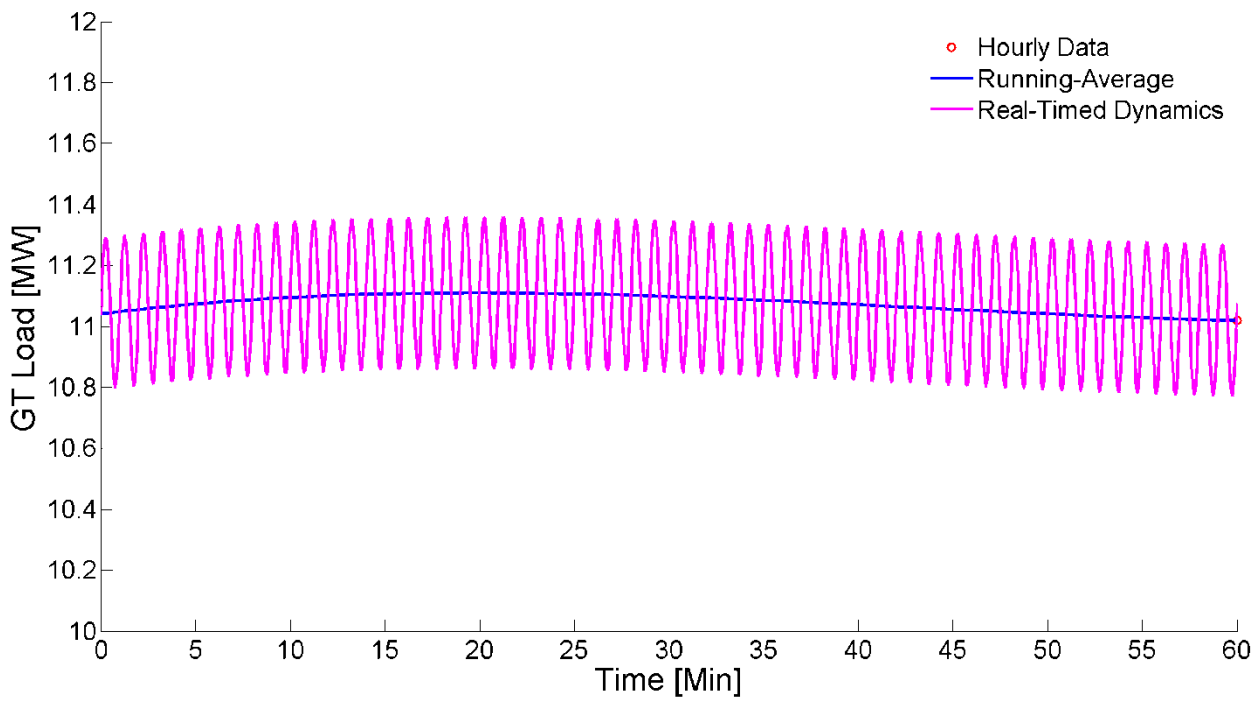

Figure 56: Projected load demand of the gas turbine under regulation service with sinusoidal minute-to-minute variations for the hour between 8 to 9 AM on a fictitious date April 24, 2020

Now, it is obvious that the actual real-timed dynamics can be highly random. It may however retain some sinusoidal characteristics for regulation up and down as CAISO attempts to balance the net load with generation. Such random behaviors can be represented by adding a random factor to the projected sinusoidal real-time dynamics shown in Figure 56. By adding a random number generator between -0.25 and +0.25 MW to the sinusoid of Figure 56, Figure 57 is produced for the same hour between 8 and 9 AM of an April day in 2020. The new dynamics now show ramp rates of 2 MW/min.

The approximated real-time dynamics of the AGC signal in Figure 57 are used as power demand input into the physical and dynamic gas turbine model presented in Section 2.2 in order to assess the physical capability of the gas turbine operating as regulation. A simulation of a day of operation of the gas turbine was carried out and the results are shown in Figure 58. The physical gas turbine dynamic model is able to follow AGC signal reasonably well. However, there are instances where the model shows that the gas turbine would have difficulty exactly following the AGC signal from CAISO. These discrepancies highlight an inherent physical limitation of this specific gas turbine engine to operate under sub 1-minute dynamics such as portrayed. It is unlikely that such errors are the result of error in the model. This is because the reliability and robustness of the gas turbine model have been extensively explored and proven based on several steady-state and dynamic simulations (see Section 2.2 and (Do, 2013)). More importantly, the dynamic response of the gas turbine model has been verified against the actual engine response as recorded at 1-minute temporal resolution.

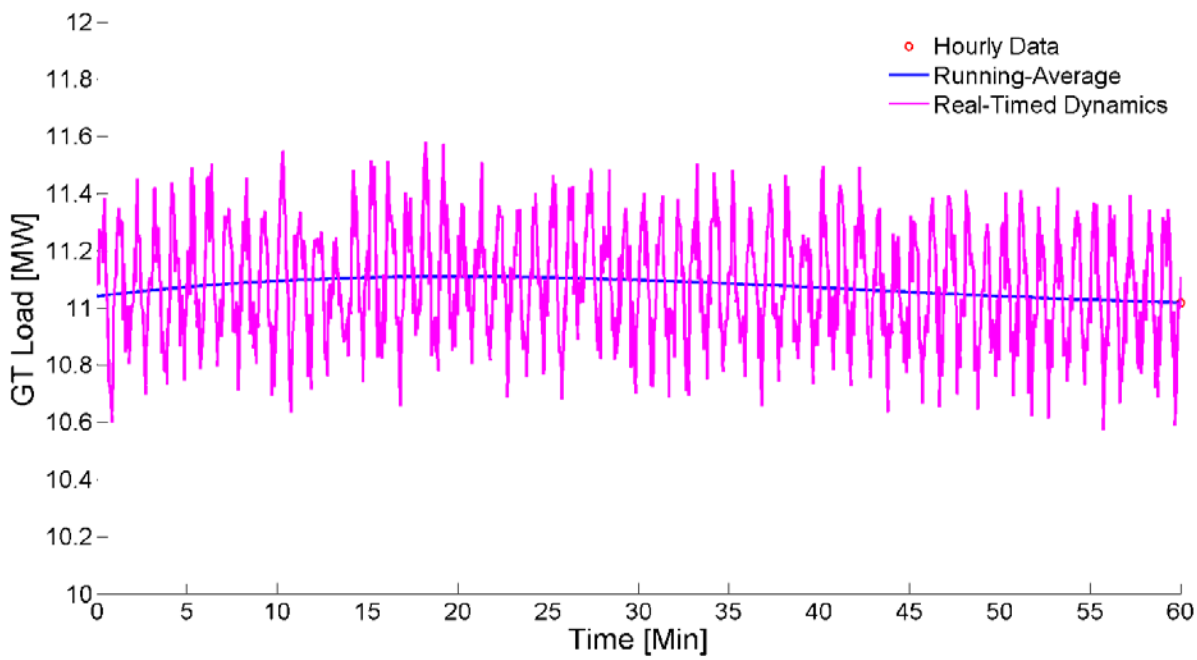

Figure 57: Projected randomized and sinusoidal characteristics for real-timed dynamics for the hour between 8am and 9am of a future April 24, 2020

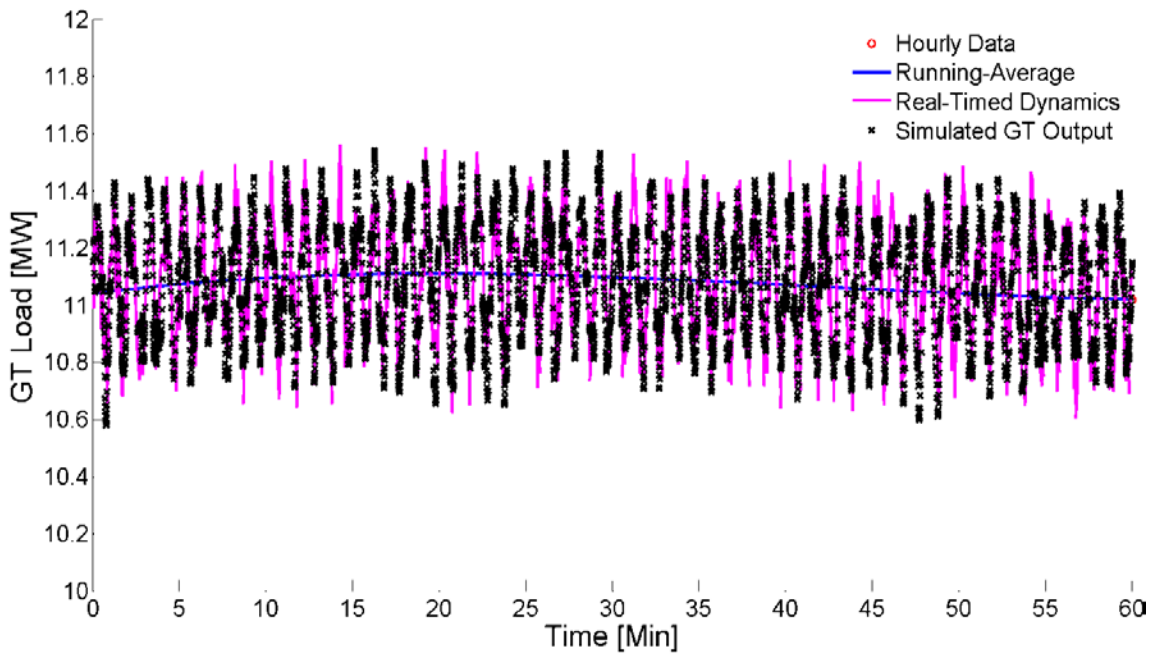

Figure 58: Simulated transient results versus the new regulation load demand for the hour between 8am and 9am of a future April 24, 2020

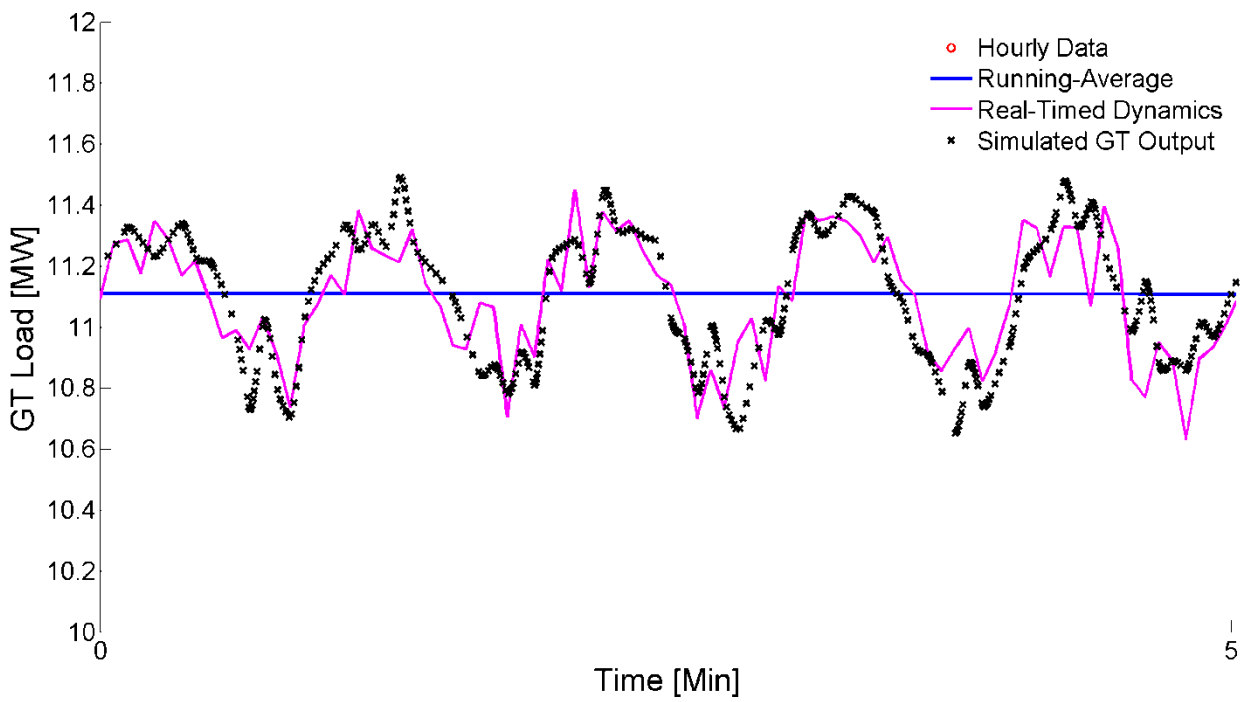

Figure 59: Simulated transient results versus the new regulation load demand for between 8:25 and 8:30 AM of a future April 24, 2020

From Figure 59, it can be concluded that the UCI gas turbine system under study cannot physically respond sufficiently to the approximated AGC signal. However, those generators operating as regulation for CAISO also exhibit a response that does not perfectly match the AGC signal as shown in Figure 60. This has been discussed in a report by Kirby et al. that the regulation response accuracy of generators is not strongly enforced on the majority of ISO systems. The stated reasons are 1) response accuracy is not formally measured in real-time and 2) it is believed that those generators cannot improve upon their response time without massive overhaul of the engines (Kirby, 2007). However, CAISO does include in its tariff language discussing Imbalance energy charges, but these charges were not included in this analysis.

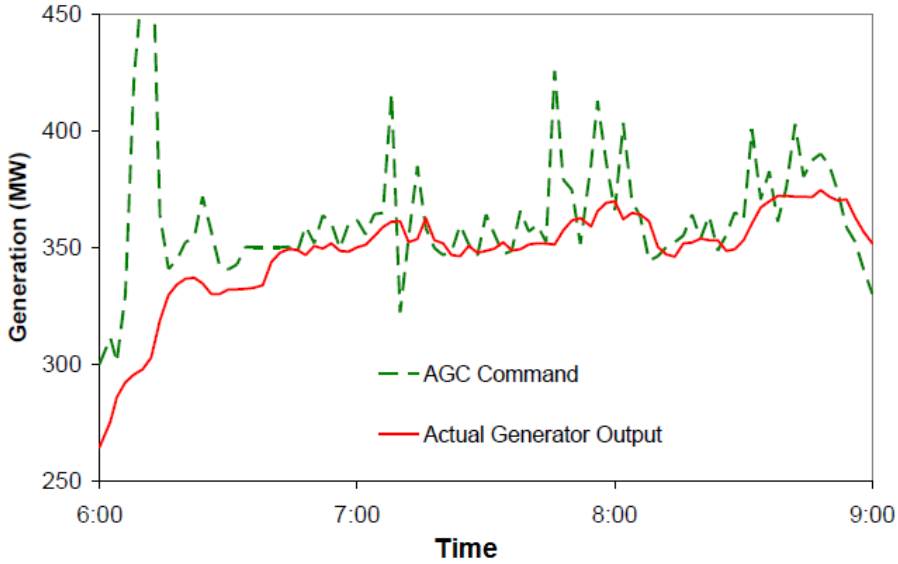

Figure 60: Regulation response of a coal-fired power plant under AGC command, showing poor response (Excerpt from(Kirby, 2007))

7 Conclusions

This report examines issues and solutions related to the integration of dual-axis CPV systems into the UCI Microgrid. These analyses are performed using the "Holistic Grid Resource Integration and Deployment" (HiGRID) tool. The HiGRID tool framework allows the models that have been developed specifically for UCI (i.e., gas turbine, steam turbine, heat recovery steam generator, electric chiller, thermal energy storage tank, fixed-panel photovoltaic, concentrating photovoltaic, vanadium redox flow battery, smart chiller dispatch) to be integrated into a system analysis tool that accounts for the interactions between the intermittent and dispatchable resources. Several analyses were performed using the HiGRID tool to demonstrate how dual-axis CPV systems could be integrated into the UCI Microgrid.

The first analysis investigated the effect of increasing the installed capacities of dual-axis CPV and fixed-tilt PV systems in the UCI Microgrid. Increasing the dual-axis CPV or fixed-tilt PV capacity always led to increased LCOE and reduced GT and ST capacity factors. However, there were interesting differences between the dual-axis CPV and fixed-tilt PV systems that can be leveraged by UCI as it continues to increase its on-site renewables. fixed-tilt PV systems will not be able to deliver as much energy for a given capacity as dual-axis CPV systems can at lower fractions of annual energy met by renewables, while at higher fractions of annual energy met by renewables fixed-tilt PV systems will begin to have the ability to deliver more energy for a given installed capacity. This difference results from the more peaky nature of dual-axis CPV systems. From this comparison, if UCI were considering only solar resources, UCI should install dual-axis CPV systems on-site up to the limit dictated by space (22MW, (Samuelsen et al., 2013)) and then move to purchase dual-axis CPV from offsite locations until 27MW is reached at which point fixed-tilt PV should then be purchased.

The capability of smart cooling load dispatch to increase dual-axis CPV energy penetrations was demonstrated. The presence of the TES tank allows the campus cooling loads to be dispatched in order to increase dual-axis CPV energy penetrations significantly, which also leads to higher GT/ST capacity factors and lower levelized costs of electricity. However, at low dual-axis CPV energy penetration, the smart cooling load dispatch is not as effective as at higher fractions of annual energy met by renewables. The energy penetration at which the smart cooling dispatch became effective at increasing the renewable energy delivered to load per MW installed was approximately 10%. The increase in dual-axis CPV energy penetration enabled by the smart cooling load dispatch was 7%. After this dual-axis CPV energy penetration, the benefit of the smart cooling dispatch became significant.

The analysis of electric energy storage using the case of a vanadium redox flow battery revealed that the implementation of energy storage achieves increased fractions of annual energy met by renewables over the case without energy storage. However, the energy storage system needs to be appropriately sized for a given fraction of annual energy met by renewables otherwise excessive curtailment could occur. At lower fractions of annual energy met by renewables, the capability of the energy storage system to reduce curtailment did not outweigh the high capital cost of this technology, but once higher fractions of annual energy met by renewables are achieved, the VFB storage system begins to be economical.

As the energy penetration of dual-axis CPV systems increase on the UCI Microgrid, the gas turbine and steam turbine must turn down in order to accommodate the renewable energy generated. As the energy penetration increases, the capacity factors decrease leaving these assets not fully utilized by the UCI Microgrid and providing an opportunity to use them in other ways to create revenue. This includes selling unused gas turbine and steam turbine capacity as spinning reserve or using the gas turbine to provide regulation. Using 4.5MW of the UCI gas turbine capacity and 5MW of the UCI steam turbine capacity for spinning reserve at CAISO market prices from 2010 and 2011 is not practical economically. Even in scenarios where the GT and/or ST bid into the market when prices were high, it was not practical economically, at least for the capacities selected for analysis. No further analysis trying to optimize the amount of capacity bid into the CAISO market was performed. Using the gas turbine to supply regulation to the CAISO and the steam turbine to provide spinning reserves was economically beneficial to UCI at 2011 prices. Through simulation using an approximated automatic generation control signal and the dynamic gas turbine model, it was also determined that the gas turbine could physically provide reasonable regulation service.

8 References

CAISO. (2010). *Integration of Renewable Resources*.

CAISO. (2011). *Annual Report on Market Issues & Performance*.

Do, A.-T. V. (2013). *Performance and Controls of Gas Turbine-Driven Combined Cooling Heating and Power Systems for Economic Dispatch*. University of California, Irvine.

Eichman, J. D., Mueller, F., Tarroja, B., Schell, L. S., & Samuelsen, S. (2013). Exploration of the integration of renewable resources into California's electric system using the Holistic Grid Resource Integration and Deployment (HiGRID) tool. *Energy*, *50*, 353–363. Retrieved from http://www.sciencedirect.com/science/article/pii/S0360544212008857

Fallah, M. H. (1978). Integrated energy conversion systems: A mathematical model of extraction steam turbine. *Energy Conversion*, *18*(1), 11–15. Retrieved from http://www.sciencedirect.com/science/article/pii/0013748078900839

Heling, M. (2008). *Assessment of the Zero-Emission Vehicle, Shared-Use Station Car (ZEV-SUSC) Mobility Concept with a Focus on Energy and Environmental Sustainability*. University of California, Irvine.

Hermanns, S. (2003). *Simulation of combined heating cooling and power equipment and application on two buildings powered by high temperature fuel cell-gas turbine hybrid systems*. Fachhochschule Trier Umwelt-Campus Birkenfeld.

Kinsey, G. S., Nayak, A., Liu, M., & Garboushian, V. (2011). Increasing Power and Energy in Amonix CPV Solar Power Plants. *IEEE Journal of Photovoltaics*, *1*(2), 213–218. doi:10.1109/JPHOTOV.2011.2172775

Kirby, B. (2007). *Ancillary Services: Technical and Commerical Insights*.

Liu, H. H. (1997). *Analysis and Performance Optimization of Commercial Chiller/Cooling Tower Systems*. Georgia Institute of Technology.

Lowe, H. J., & Christie, D. G. (1961). Heat Transfer and Pressure Drop Data on Cooling Tower Packings, and Mode Studies of the Resistance of Natural Draft Towers to Airflow. *ASME Heat Transfer Proceedings*, *Paper 113*.

Makarov, Y. V., Loutan, C., & de Mello, P. (2009). Operational Impacts of Wind Generation on California Power Systems. *IEEE Transactions on Power Systems*, *24*(2), 1039–1050. doi:10.1109/TPWRS.2009.2016364

Samuelsen, S., Mueller, F., & Eichman, J. (2013). *Piloting the Integration and Utilization of Renewables to Achieve a Flexible and Secure Energy Infrastructure* (pp. CEC–PIR–08–033).

Solar Turbines. (2010). *Solar Titan 130 Generator Set Brochure*.

Spectrolab. (2010). C3MJ Third Generation dual-axis CPV Technology Data Sheet. Retrieved from http://www.spectrolab.com/DataSheets/fixed-tilt PV/dual-axis CPV/C3MJ CDO Products 20100818.pdf

Walker, G. (2001). Evaluating MPPT converter topologies using a MATLAB fixed-tilt PV model. *Journal of Electrical & Electronics Engineering*.

Wildin, M. W., & Truman, C. R. (1985). A summary of experience with stratified chilled water tanks. *ASHRAE Transaction*, *20*(Part 1B), 956–976.